Interchromophoric Interactions

Between TMR, Alexa, and BODIPY Fluorophores

by

Bryan M. Donaphon

A Dissertation Presented in Partial Fulfilment
of the Requirements for the Degree
Doctor of Philosophy

Approved April 2018 by the
Graduate Supervisory Committee:

Marcia Levitus, Chair
Neal Woodbury
Wade Van Horn

ARIZONA STATE UNIVERSITY

May 2018

ABSTRACT

The fundamental photophysics of fluorescent probes must be understood when the probes are used in biological applications. The photophysics of BODIPY dyes inside polymeric micelles and rhodamine dyes covalently linked to proteins were studied. Hydrophobic boron-dipyrromethene (BODIPY) dyes were noncovalently encapsulated inside polymeric micelles. Absorbance and fluorescence measurements were employed to study the photophysics of these BODIPY dyes in the micellar environments. Amphiphilic polymers with a hydrophobic character and low Critical Micelle Concentration (CMC) protected BODIPYS from the aqueous environment. Moderate dye loading conditions did not result in ground-state dimerization, and only fluorescence lifetimes and brightnesses were affected. However, amphiphilic polymers with a hydrophilic character and high CMC did not protect the BODIPYS from the aqueous environment with concomitant ground-state dimerization and quenching of the fluorescence intensity, lifetime, and brightnesses even at low dye loading conditions. At the doubly-labeled interfaces of *Escherichia coli* (*E. coli*) DNA processivity β clamps, the interchromophric interactions of four rhodamine dyes were studied: tetramethylrhodamine (TMR), TMR C6, Alexa Fluor 488, and Alexa Fluor 546. Absorbance and fluorescence measurements were performed on doubly-labeled β clamps with singly-labeled β clamps and free dyes as controls. The absorbance measurements revealed that both TMR and TMR C6 readily formed H-dimers (static quenching) at the doubly-labeled interfaces of the β clamps. However, the TMR with a longer linker (TMR C6) also displayed a degree of dynamic quenching. For Alexa Fluor 546 and Alexa Fluor 488, there were no clear signs of dimerization in the absorbance scans. However, the

fluorescence properties (fluorescence intensity, lifetime, and anisotropy) of the Alexa Fluor dyes significantly changed when three methodologies were employed to disrupt the doubly-labeled interfaces: 1) the addition of sodium dodecyl sulfate (SDS) detergent to denature the proteins, 2) the addition of clamp loader (γ complex) to open one of the two interfaces, and 3) the use of subunit exchange to decrease the number of dyes per interface. These fluorescence measurements indicated that for the Alexa Fluor dyes, other interchromophoric interactions were present such as dynamic quenching and homo-Förster Resonance Energy Transfer (homo-FRET).

DEDICATION

I would like to thank my friends and acquaintances in the various ASU graduate science programs including Bobby Baravati, Andrew Serban, Devon Bridgeman, and others too numerable to mention. They listened to my concerns and my scientific ideas and kept me motivated when I was questioning my path. In the early years of my graduate program, I immensely enjoyed exploring the wilderness and natural beauty of Arizona with Bobby. The camping at Sedona, Flagstaff, and Show Low (the White Mountains) helped me take my mind off graduate school during much-needed breaks. During the summer, hiking at Mount Lemmon, Mount Graham, and the Pinal Mountains offered escapes from the congested city of Phoenix with 120°F plus weather. Bobby also rekindled my interest in Stephen King books which was another outlet for me to relax. I would like to thank two other friends: Timothy Lamb and Rene Hernandez Jr. Timothy Lamb is an excellent instructor for the ASU School of Molecular Sciences (SMS) General Chemistry for Majors class including the labs and recitations. Tim was a great teaching supervisor who helped me improve the quality of my teaching. Therefore, working under Tim was one of the few positive teaching experiences I had at ASU. I wish Tim good luck in the further development of his teaching career at ASU, and I have no doubt that an instructor of his caliber will be successful in the future. Rene is the Research Lab Coordinator for the General Chemistry Stockroom for the School of Molecular Sciences. Rene is one of the most dedicated workers I have seen in the stockroom. Because of Rene and the other hard workers in the stockroom, my General Chemistry teaching labs went smoothly. If chemicals or other supplies were missing or if there was too much chemical waste, Rene would promptly respond to the requests for

assistance. Furthermore, in the early years, when I was still an inexperienced teacher's assistant for the chemistry labs, Rene went out of his way to help me learn the proper lab procedures. Last but not least, I never missed an opportunity to enjoy a round of beers at the Devil's Advocate happy hour with Tim and Rene on Friday after a long week. Those happy hours helped me decompress and recover from my graduate studies.

While my friends' contributions to my success and well-being were invaluable, I would not be here without my family. My family always supported my research endeavors in science and mathematics even if some concepts like "photophysics" sounded strange to them. I would like to thank my father for giving me good advice on how academia works and on alternatives to academia. I would like to thank my mother for always supporting my ambitions. Last but not least, I would like to thank my sister Shellie for always being there for me. Without my parents' emotional and financial support, I would not have made it through my undergraduate studies in Tennessee or my graduate studies in Arizona.

On a more humorous note, I would like to thank both coffee and alcohol for helping me survive my graduate studies. Just like excess solvent is needed in organic chemistry to drive a chemical reaction forward, coffee and alcohol were essential in driving me forward through my graduate studies. I would like to thank Biodesign Facilities and Parks Coffee for providing the coffee and Devil's Advocate and Four Peaks Brewery for making and providing the alcohol.

ACKNOWLEDGMENTS

I would like to thank Dr. Su Lin and Doug Daniel for providing invaluable assistance for my ensemble fluorescence experiments in the ASU Ultrafast Laser Facility. Whenever there were issues with the computers, laser, AOTF, or the overall alignment of the TCSPC setup, Su and Doug would respond promptly to requests for assistance. I would also like to thank my research colleagues over the years including Andrew Serban, Nikita Kumari, and Anirban Purohit. They listened to my concerns about research and life in general and offered much-needed criticism of my scientific ideas and presentations so that I could present better next time. I will greatly miss the science seminars that I attended with my colleagues. I would like to thank Michael Dodson from the Biodesign Center for Single Molecule Biophysics (SMB) for patiently navigating me through the labyrinth nature of the Biodesign building. With so many different research centers and groups, it was difficult to know who to contact when there were problems with the computers, equipment, or shipping orders. Mike helped me figure out how the different groups in the Biodesign building operated. I would like to thank Dr. Raymo and his student Sicheng Tang for providing BODIPY dyes and amphiphilic polymer for my micelle project. I would also like to thank Dr. Linda Bloom and her students for providing the dye-labeled β clamps, unlabeled β clamps, and clamp loader for my beta clamp project. Last but not least, I would like to thank Dr. Marcia Levitus for providing much-needed direction to my graduate studies. I had no experience with photophysics from my undergraduate studies, so Dr. Levitus was essential in helping me understand the field of photophysics. Without funding from Dr. Levitus, I would have been unable to use the ASU Ultrafast Laser Facility for many of my measurements.

TABLE OF CONTENTS

Page

CHAPTER Page

CHAPTER Page

LIST OF TABLES

LIST OF FIGURES

Figure Page

CHAPTER ONE

INTRODUCTION TO FLUORESCENCE

1.1 Fluorescence Concepts

Small organic conjugated molecules known as dyes/fluorophores can interact with light. The Jablonski Diagram shown in Figure 1.1 depicts the interactions between dyes and photons of light. The electronic states of a dye are shown with each electronic state divided into different vibrational levels. Upon the dye's absorption of a photon, an electron in the singlet ground state (S_0) can be excited to a singlet excited state (S_1, S_2, etc). Light absorption is near instantaneous on the timescale of femtoseconds. As shown in Figure 1.2, singlet states are states where the pair of electrons have opposite spins. In a singlet excited state, the spin of the excited state electron is still paired with that of the ground state electron. Fluorescence is the radiative relaxation/decay of the singlet excited state. In other words, a photon of light is emitted as the excited electron returns, or decays, to the ground state. Fluorescence occurs on the timescale of nanoseconds. There are two important measures of fluorescence: quantum yield and lifetime. Quantum yield is the ratio of emission photons to absorbed photons. Dyes with high quantum yields, approaching unity, are considered bright. The fluorescence lifetime is the time it takes for the excited state population to decay to e^{-1} of its initial value.

As depicted in Figure 1.1, fluorescence almost always occurs from the lowest vibrational level of S_1. Two mechanisms are responsible for this: internal conversion and vibrational relaxation. Internal conversion is a radiationless de-excitation mechanism whereas vibrational relaxation is a transition from a higher vibrational level to a lower

vibrational level within the same electronic state. Vibrational relaxation occurs due to the fast picosecond rearrangement of water molecules around the dye to minimize the energy of the dye's excited state. Because of these mechanisms, the fluorescence always has less energy, or longer wavelength, compared to the exciting light. The difference in energies/wavelengths between the excitation and emission is known as Stokes shift.

Figure 1.1 displays the symmetry between excitation and emission: excitation to different vibrational levels of the excited state vs return to different vibrational levels of the ground state. This symmetry causes the absorbance/excitation and emission spectra to be mirror images of each other.

Another radiationless de-excitation mechanism would be intersystem crossing where the spin of the excited electron flips. This action creates a triplet excited state. Radiative relaxation from the triplet excited state is known as phosphorescence. Phosphorescence occurs on a longer timescale of milliseconds or even hours because the spin of the excited electron must flip again before it can decay back to the ground state. When the excited electron returns to the ground state, its spin must be opposite that of the ground electron (Pauli Exclusion Principle). These spin-flips are classically forbidden and have a low probability in quantum mechanics: hence, the long timescale.

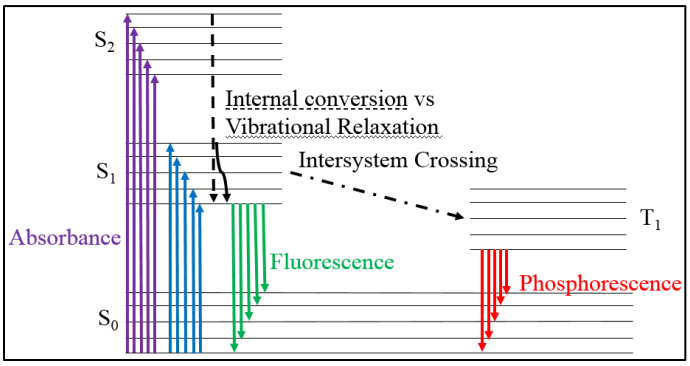

Figure 1.1: Jablonski Diagram.

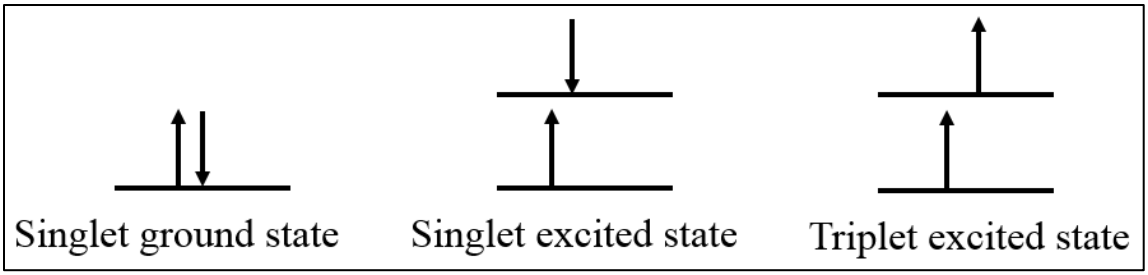

Figure 1.2: Singlet vs Triplet.

Figure 1.3 reveals the effects of polarization and photoselection. If the exciting light is of a certain polarization, then the dye molecules whose absorption dipoles are oriented in that direction will be preferentially excited (photoselection). The probability of absorption/excitation will follow a $\cos^2\theta$ dependence where θ is the angle between the absorption dipole of the dye and the direction of the polarized exciting light. With vertically polarized excitation light, vertically oriented dyes (0°) will have the highest probability of absorption whereas dyes oriented at an angle to the vertical will have a lower probability of absorption. Horizontally oriented dyes (90°) will not be excited at all. If the solution is a cold, viscous, rigid medium, then the dye molecules will not sufficiently move on the timescale of fluorescence. Therefore, the fluorescence polarization will be high (similar to that of the exciting light). However, if the solution is fluid (hot and non-viscous), then the orientations of the dye molecules will randomize during the fluorescence, and the fluorescence polarization will be small. Besides rotational diffusion, other factors such as energy transfer can affect the fluorescence polarization. Anisotropy is another measure of polarization and will be explained in greater detail in the next section.

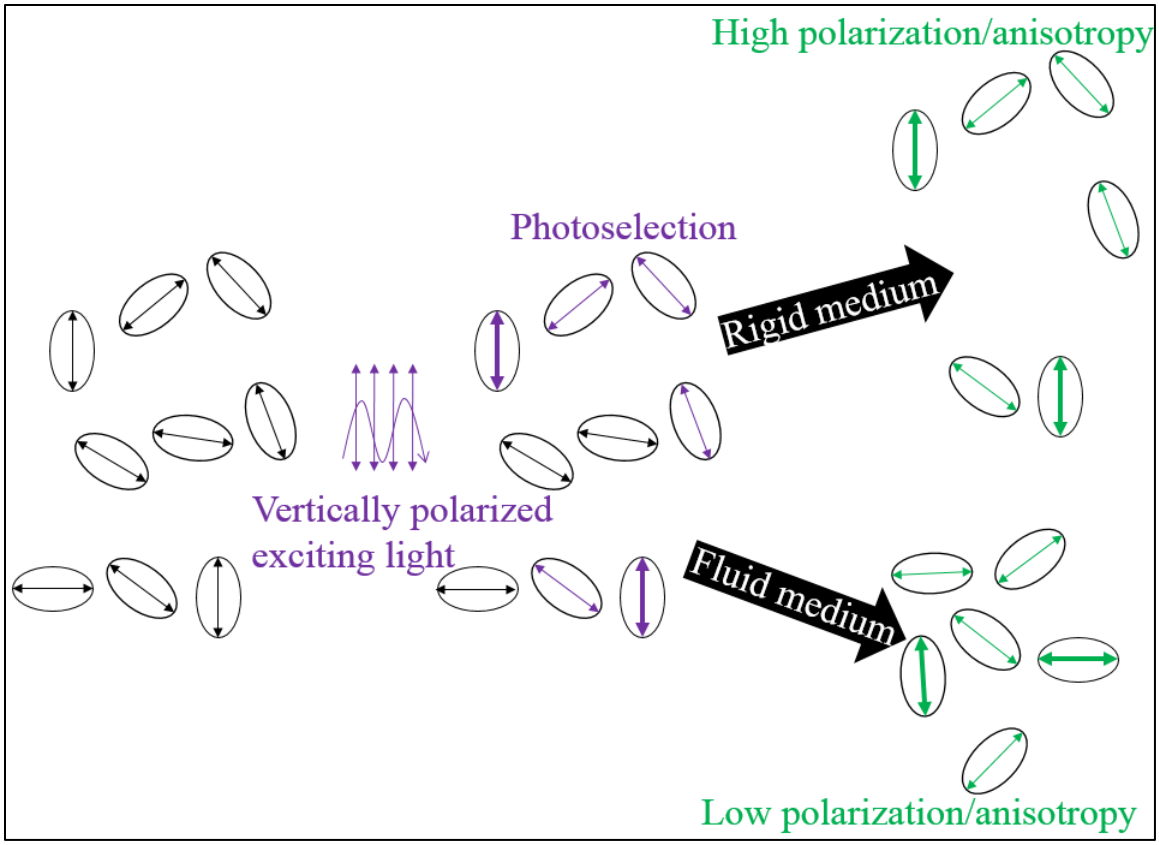

Figure 1.3: Effects of Photoselection and Media on Fluorescence Polarization.

1.2 Instrumentation of Fluorescence Techniques

A. Fluorimeter

The PTI Quantamaster fluorimeter was used to measure excitation and emission scans. For excitation scans, the excitation wavelength is varied while the emission is collected at a fixed wavelength. In contrast, for emission scans, the excitation wavelength is fixed while the emission is collected at varying wavelengths. Figure 1.4 shows the diagram of the fluorimeter. A xenon arc lamp (1) provides a bright white light while an excitation monochromator (4) allows the selection of the excitation wavelength out of the white light. A focusing lens guides the excitation light to the cuvette holder (5)

for the sample. The fluorescence is collected perpendicular to the direction of the excitation in order to minimize the collection of scattered excitation light. An emission monochromator (6) allows the selection of a particular emission wavelength while the photomultiplier tube (PMT) (7) detects the fluorescence photons. Slits (2) and shutters (3) control the intensity of light in both the excitation and detection pathways.

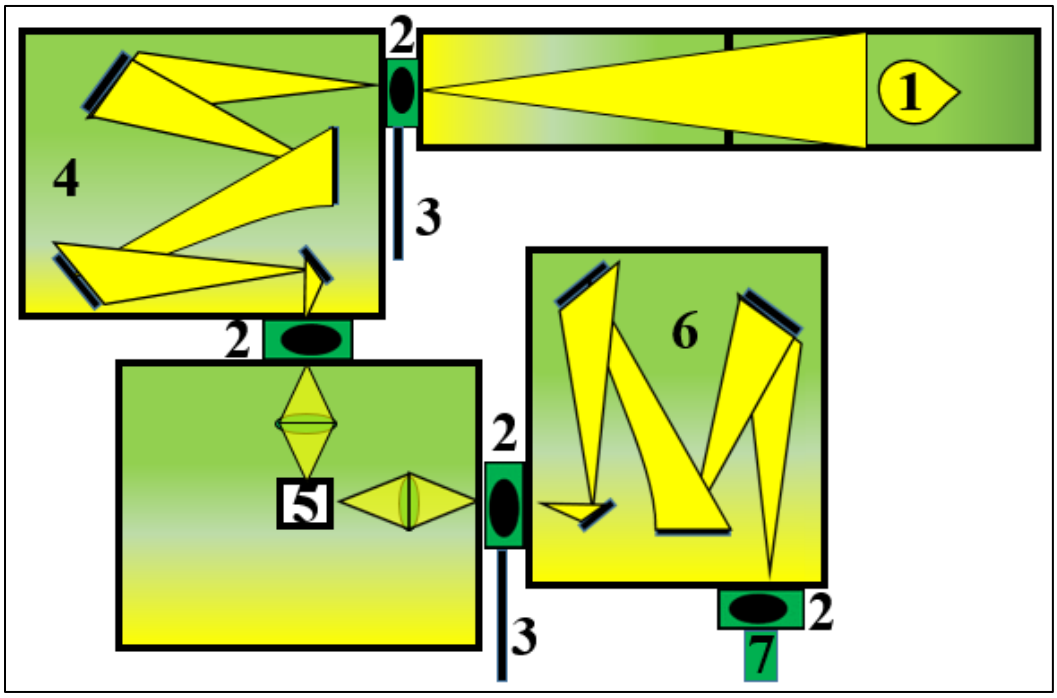

Figure 1.4: Fluorimeter [Lamp (1), Slit (2), Shutter (3), Excitation Monochromator (4), Cuvette Holder (5), Emission Monochromator (6), and PMT Detector (7)]

One potential artifact present in all absorbance and fluorescence techniques is primary and secondary inner filter effects. In samples with high optical density/absorbance, both attenuation of the excitation light and reabsorption of emission light may occur. Figure 1.5 depicts the primary inner filter effect. In the dilute sample, the excitation light travels uniformly through the solution whereas in the concentrated sample, the excitation light is attenuated as it travels through the solution. These artifacts can be avoided by keeping the optical density at 0.1 or below.

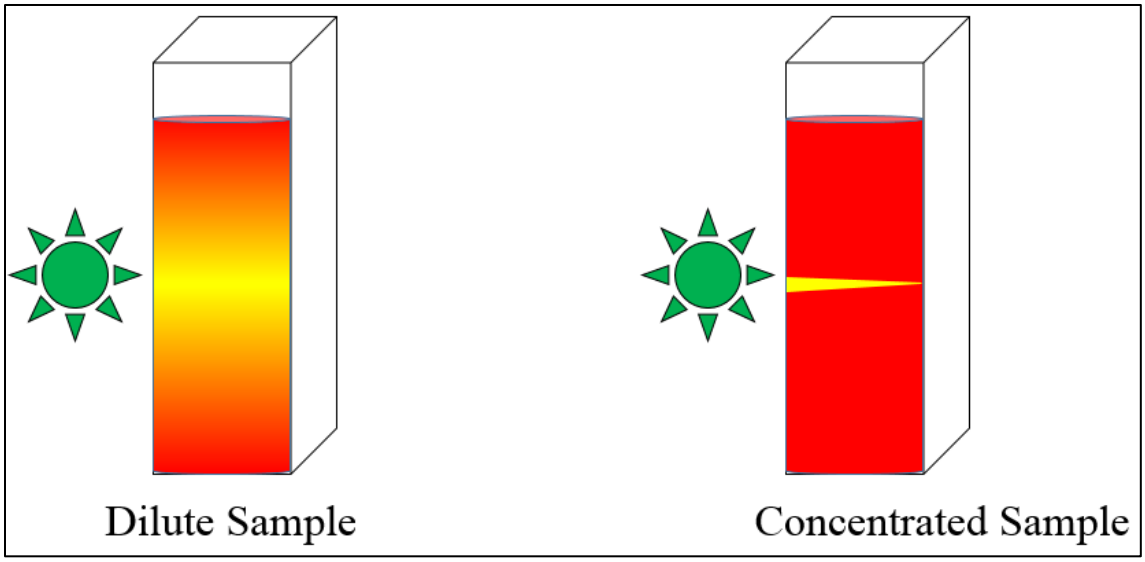

Figure 1.5: Primary Inner Filter Effect

B. Time-Correlated Single Photon Counting

Time-Correlated Single Photon Counting (TCSPC) uses a pulsed laser along with sophisticated timing electronics to measure the time between excitation of the sample and the emission of a fluorescence photon. Depending on the repetition rate, the pulsed laser can generate millions of excitation cycles per second. The times between excitation and emission are referred to as photon arrival times and are recorded for each excitation cycle. As shown in Figure 1.6, a histogram of photon arrival times can be generated. This histogram describes the decay of the excited fluorophore population. Analysis of this decay curve allows the determination of the fluorescence lifetime. The true decay can be described by a monoexponential decay in Equation 1.1

$$I(t) = I_0 e^{-t/\tau} \tag{1.1}$$

where I_0 is the peak/maximum of the decay and τ is the fluorescence lifetime. The fluorescence lifetime is the time at which the excited state population has decayed to e^{-1}

of its initial value. It is important to keep in mind the following: not all excited dyes decay to the ground state within τ. Instead, the lifetime is a statistical property that states that only e^{-1} of the initial excited fluorophore population has not yet decayed. For the cases of one species in different environments or multiple species present, Equation 1.2 describes the decay as a sum of discrete exponential decays.

$$I(t) = \sum_{i=1}^{n} A_i e^{-t/\tau_i} \tag{1.2}$$

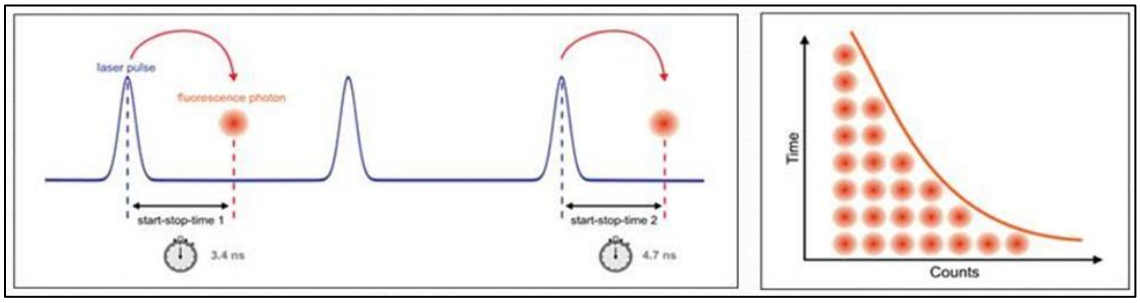

Figure 1.6: Histogram of Photon Arrival Times in TCSPC. Photon arrival times for separate excitation cycles are recorded. The detection events are then organized into a histogram. Figure by courtesy of Dr. Su Lin.

Unfortunately, analysis of TCSPC decay curves is not so straightforward. The photodetector has an inherent timing response that gets convoluted with the true decay. The timing response of the detector and the overall setup is referred to as the Instrument Response Function (IRF). Both a picosecond pulsed laser and a detector with a timing response in the tens of picoseconds are essential in order to have a good IRF. An IRF should have a narrow Full Width at Half Maximum (FWHM). The IRF can be measured with Ludox, a colloidal silica solution. Equation 1.3 describes the experimental decay as a convolution of the IRF with the true decay

$$N(t) = \int_0^t L(t')I(t-t')dt' \tag{1.3}$$

where *N(t)* is the experimental decay, *L(t')* is the IRF, and *I(t-t')* is the true decay.

The fluorescence lifetimes can be determined with IRF reconvolution and least squares fitting. First, the IRF is convoluted with a simulated decay. This simulated convolution is then iteratively compared to the experimentally measured decay. The goal is to minimize the sum of squared differences between the simulated convolution and the experimentally measured decay as shown in Equation 1.4

$$\chi^2 = \sum_{i=1}^{n} \frac{1}{\sigma_i^2} [\, N(t_i) - I(t_i)]^2 \qquad (1.4)$$

where *N(t)* is the experimentally measured decay, *I(t)* is the true/simulated decay, and $1/\sigma^2$ is the weight (reciprocal of the variance). Since photon counting data follow a Poisson distribution, the variance is the average number of photon counts at time *i*. Indicators of a good fit are a low χ^2 and randomness of the residuals.

Polarization artifacts can also affect the TCSPC data. Ideally, the collected emission would be representative of the total emission. The total emission is depicted in Figure 1.7 and is defined in Equation 1.5 as $I_{VV} + 2I_{VH}$ where I_{VV} and I_{VH} are vertically and horizontally oriented emissions upon vertical excitation. Equations 1.6-1.7 describe the vertically and horizontally oriented emissions where θ and Φ are angles relative to the *z* and *y* axes respectively. Unfortunately, emission monochromators have polarization biases in which either horizontally or vertically oriented fluorescence will be transmitted more efficiently than the other orientation. The magic angle condition must be used so that the collected emission is proportional to the total emission. In the magic angle condition, the sample is excited with vertically polarized light (0°), and the emission is collected at the magic angle (54.7° with respect to the vertical *z* direction). The magic angle condition allows I_{VH} to be detected twofold over I_{VV}. The following derivation explains how the magic angle condition fulfills that detection requirement.

$$I_T = I_{VV} + 2I_{VH} \tag{1.5}$$

$$I_{VV} = \cos^2\theta \tag{1.6}$$

$$I_{VH} = \sin^2\theta\sin^2\Phi \tag{1.7}$$

If it is assumed that the dyes are equally distributed between 0 and 2π in the Φ direction, then Equation 1.8 describes the average value of $sin^2\Phi$.

$$\langle sin^2\Phi \rangle = \frac{\int_0^{2\pi} sin^2\Phi \, d\Phi}{\int_0^{2\pi} d\Phi} = \frac{1}{2} \tag{1.8}$$

The 2 from Equation 1.5 and the ½ from Equation 1.8 cancel each other out. Equation 1.5 simplifies to $I_T = cos^2\theta + sin^2\theta$. If θ is 54.7°, then $\cos^2(54.7°)$ is 0.333 and $\sin^2(54.7°)$ is 0.667. The horizontally oriented emission will be detected twofold more than the vertically oriented emission. Now, the collected emission is proportional to the total emission.

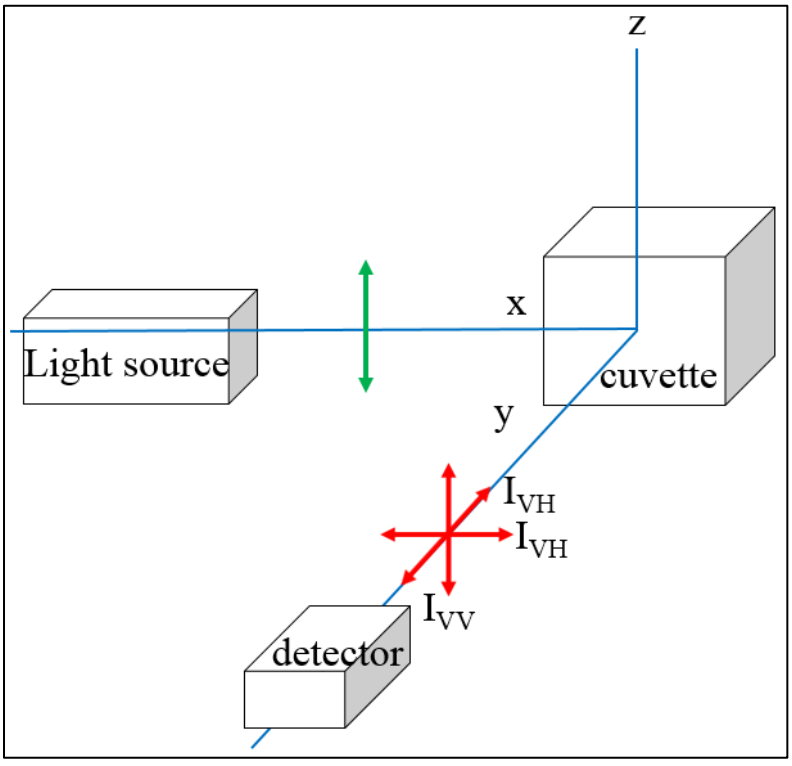

Figure 1.7: Total Emission Intensity in Cuvette Setup

Another potential artifact is the pile-up effect. The photon count rate should be low (just 1% of the repetition rate). Since the timing electronics are not instant, the photodetectors have a dead time where the detection of one photon prevents the detection of another photon until the detector is ready again. If a large number of photons are emitted during one excitation cycle, only the first photon will be detected. This shortcoming biases the TCSPC histogram to earlier photon arrival times resulting in a lower measured lifetime. In order to avoid this bias, the photon count rate should be a small percentage of the repetition rate.

The TCSPC setup used in this research is described in Figure 1.8. A pulsed laser provides the source of excitation and a SYNC signal which is an electrical signal analogous to the optical pulse. A radial neutral density filter is used to control the intensity of the exciting light before the exciting light reaches the sample in the cuvette holder. The fluorescence is collected perpendicular to the direction of the excitation. An emission filter selects the desired range of emission wavelengths, and the photomultiplier tube (PMT) acts as the detector. A TCSPC timing card receives signals from both the SYNC and the PMT detector which allow it to calculate the photon arrival times and generate the corresponding histogram.

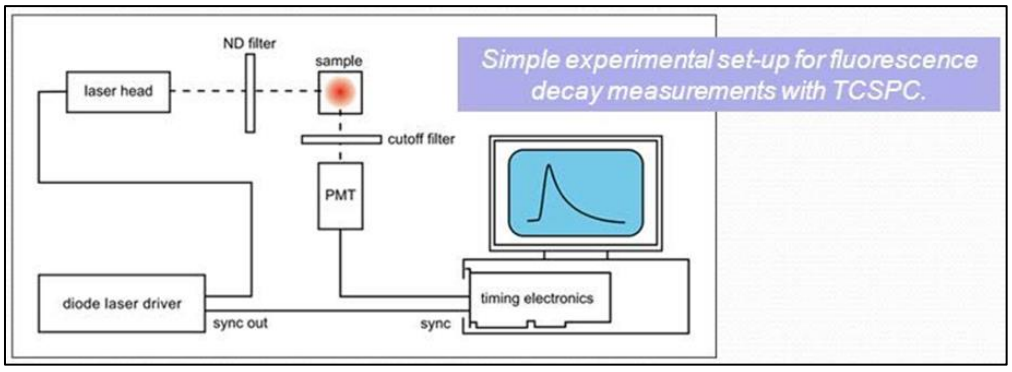

Figure 1.8: TCSPC Setup. Figure by courtesy of Dr. Su Lin.

C. Time-Resolved Fluorescence Anisotropy

As mentioned earlier, fluorescence polarization refers to the polarization of the emission upon excitation of the sample with polarized light. Rotational diffusion and energy transfer determine the extent of the fluorescence polarization. Polarization can be calculated by exciting with vertically polarized light and monitoring the emission in the vertical and horizontal directions. Polarization is defined as a ratio of intensities in Equation 1.9.

$$P = \frac{I_{VV} - I_{VH}}{I_{VV} + I_{VH}} \tag{1.9}$$

However, the polarization is not normalized correctly because the total intensity is $I_{VV} + 2 \times I_{VH}$. Hence, a new term called anisotropy was used to refer to the correct normalization as shown in Equation 1.10. It is important to note that polarization/anisotropy are experimentally calculated, not experimentally measured.

$$r = \frac{I_{VV} - I_{VH}}{I_{VV} + 2I_{VH}} \tag{1.10}$$

Ideally, Equation 1.10 would be a sufficient description of anisotropy. However, there are other considerations. Monochromators can display a polarization bias which will impact polarization/anisotropy measurements. In order to account for this polarization bias, the G factor must be measured with a free dye standard. The G factor is I_{HV}/I_{HH}. Equation 1.11 displays the G factor correction in the anisotropy.

$$r = \frac{I_{VV} - G \times I_{VH}}{I_{VV} + 2 \times G \times I_{VH}} \tag{1.11}$$

The anisotropy can be fit to the Perrin Equation (Equation 1.12) if rotational diffusion is the only contribution

$$r = \frac{r_0}{(1 + \frac{\tau}{\theta})} \tag{1.12}$$

where r_0 is the fundamental anisotropy (at $t = 0$), τ is the fluorescence lifetime, and θ is the rotational correlation time (the time it takes for the dye molecule to rotate one radian on average). The Perrin Equation shows that anisotropy can be used to monitor rotational diffusion if the rotational diffusion occurs on the same timescale as fluorescence.

In the absence of rotational diffusion and energy transfer, the fundamental anisotropy describes the loss of anisotropy due to photoselection and angular displacement between the absorption and emission dipoles. Because of the $cos^2\theta$ dependence in photoselection, dyes that are not precisely oriented with the polarized excitation will still be excited. If the absorption and emission dipoles are collinear, r_0 will be 0.4. However, an angle β between the absorption and emission dipoles will further decrease the anisotropy by $(3cos^2\beta-1)/2$. With these two contributions, the fundamental anisotropy can be defined in Equation 1.13.

$$r_0 = \frac{2}{5}\left(\frac{3cos^2\beta-1}{2}\right) \quad (1.13)$$

While steady state anisotropy is useful, time-resolved anisotropy can reveal how quickly the anisotropy decays. The time-resolved anisotropy can be calculated using Equation 1.14. Although $G = \frac{\int I_{HV}(t)dt}{\int I_{HH}(t)dt}$, the G factor can alternatively be calculated with tail-matching. In tail-matching, $I_{VV}(t)$ and $I_{VH}(t)$ are measured for a free dye standard whose rotational correlation time is much shorter than the fluorescence lifetime. Because of that condition, the fluorescence emission is expected to be depolarized at long times. Therefore, the two decay curves can be scaled until their tails match (i.e. have equal intensities at long times). The scaling factor, or multiplication factor, is the G factor.[1, 2]

$$r(t) = \frac{I_{VV}(t)-G\times I_{VH}(t)}{I_{VV}(t)+2\times G\times I_{VH}(t)} \quad (1.14)$$

For a spherical object, the anisotropy can be fit to a mono-exponential decay in Equation 1.15.

$$r(t) = r_0 e^{-t/\theta} \tag{1.15}$$

Many factors can lead to more complicated anisotropy decays. For example, dyes never have spherical shapes. Dyes can also be surrounded by anisotropic environments or attached to biological macromolecules. Similar to the TCSPC decay curve, a sum of discrete exponential decays can be used as shown in Equation 1.16.

$$r(t) = \sum_{i=1}^{n} r_{0i}\, e^{-t/\theta_i} \tag{1.16}$$

However, various complex fitting models can also be used. Hindered Rotor (Equation 1.17) assumes that a crowded anisotropic environment leads to a limiting anisotropy. In other words, the fluorescence anisotropy cannot decay to zero within the timescale of the experiment due to the limited motion of the dye. An example would be a dye embedded in a membrane

$$r(t) = (r_0 - r_\infty)e^{-t/\theta} + r_\infty \tag{1.17}$$

where r_∞ is the limiting anisotropy.

Segmental Mobility of a Biopolymer-Bound Fluorophore (Equation 1.18) describes the anisotropy decay of a dye attached to a biological macromolecule with a flexible covalent linker. This fitting model assumes two rotational correlation times: one correlation time associated with the local motion of the attached dye and the other time associated with the global motion of the macromolecule.

$$r(t) = r_0[\alpha e^{-t/\theta_f} + (1-\alpha)]e^{-t/\theta_p} \tag{1.18}$$

Where θ_f is the correlation time associated with the fast segmental motions of the attached dye and θ_p is the correlation time associated with the slow overall motion of the biological macromolecule. This fitting model is a special case of hindered rotor where the anisotropy decays rapidly to $r_\infty = r_0 (1-\alpha)$ due to the fast motion of the dye. Then, the anisotropy slowly decays to zero due to the slow motion of the macromolecule.

Similar to the TCSPC decay, the IRF can also affect the anisotropy decay. However, a simple IRF reconvolution cannot be performed because the anisotropy decay is calculated, not measured. The only way to take the IRF into account is to do a simultaneous fitting of I_{VV} and I_{VH}.

For the purpose of this research, the anisotropy decays were not fit. Instead, the focus was on the trends. Therefore, no attempt was made to account for the IRF.

The TCSPC setup described in Figure 1.8 was also used for the time-resolved anisotropy measurements.

D. Fluorescence Correlation Spectroscopy

Fluorescence Correlation Spectroscopy (FCS) refers to the autocorrelation of fluorescence fluctuations over a range of delay times from a small number of molecules within an optically restricted volume.[3] This autocorrelation of fluorescence fluctuations is described in Equation 1.19

$$G(\tau) = \frac{\langle \delta F(t) \delta F(t+\tau) \rangle}{\langle F \rangle^2} \tag{1.19}$$

where τ is the delay time, or lag time, and $\delta F(0)$ and $\delta F(\tau)$ are the fluorescence fluctuations around the average intensity $\langle F \rangle$ at times 0 and τ, respectively. This

autocorrelation function is normalized by the average intensity squared $\langle F \rangle^2$. In Figure 1.9, an intensity time trace depicts $\delta F(t)$ and $\delta F(t + \tau)$ from $\langle F \rangle$.

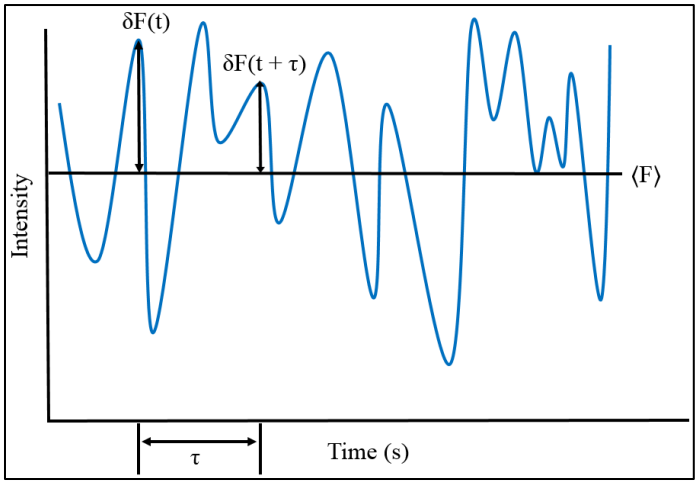

Figure 1.9: Intensity Time Trace

For FCS measurements, the concentration is typically in the nanomolar or picomolar range, and the optically restricted volume is typically on the order of femtoliters. The dilute sample concentration and the small observation volume ensure that only a few molecules are in the observation volume at any given time. Due to these characteristics, FCS is considered a quasi-single molecule technique. The average number of molecules in the observation volume can be calculated by Equation 1.20

$$N = N_A C V \tag{1.20}$$

where N_A is Avogadro's Number, C is the molar concentration, and V is the observation volume.

The observation volume is created through confocal optics: 1) an objective lens focuses the laser (with a Gaussian profile) to a diffraction limited spot within the sample and 2) a pinhole/aperture in the detection pathway rejects out-of-focus light. This pinhole is located at the conjugate focal plane: hence, confocal optics. Under these two

conditions, the confocal observation volume is typically an ellipsoid elongated along the optical axis. The observation volume is depicted in Figure 1.10a. The longer axis of the observation volume that is elongated along the optical axis is referred to as the semi-major axis *u* while the smaller axis is referred to as the semi-minor axis *s*, or waist.

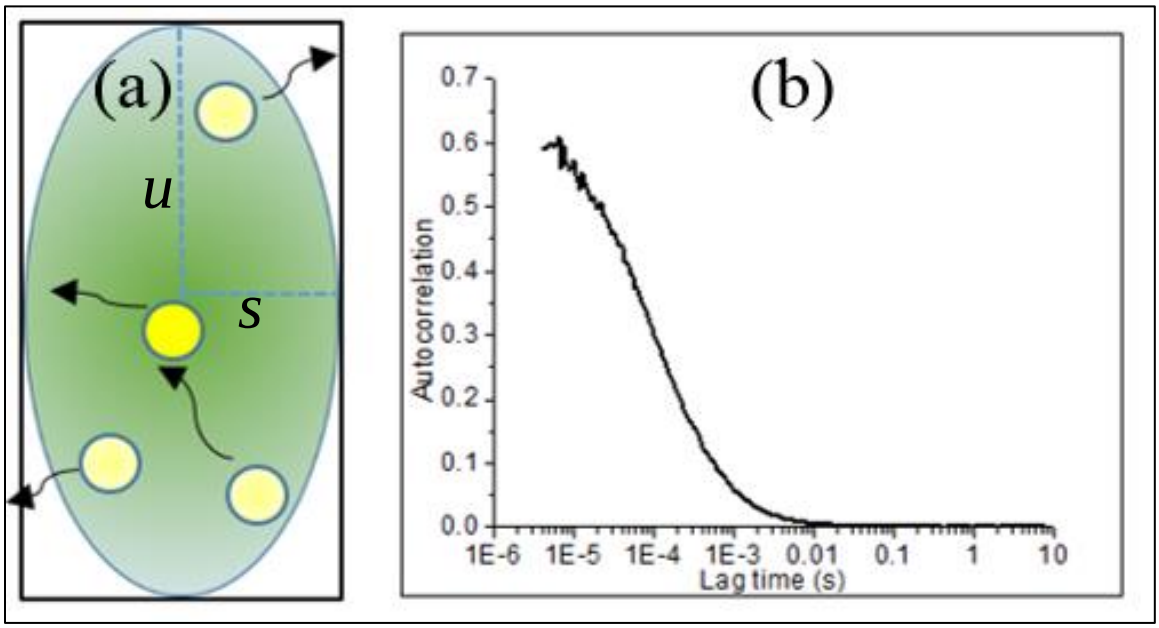

Figure 1.10: FCS Observation Volume and Autocorrelation Curve. (a) The confocal observation volume is illuminated with a green laser of Gaussian profile. The center of the observation volume is most brightly illuminated. The molecules inside this volume display yellow fluorescence. The black arrows depict the trajectories of the diffusion. The horizontal and vertical blue dashes depict the semi-minor axis s and the semi-major axis u respectively. (b) An autocorrelation curve for 1 nM TAMRA dye in water excited at 532 nm.

Many processes can lead to fluorescence fluctuations such as transitions to the dark triplet state (blinking), binding, and diffusion due to Brownian motion. The decay of the autocorrelation function reveals the timescale of these processes. If Brownian motion is the only contribution to the fluorescence fluctuations, then fast diffusion through the observation volume will cause the correlation to decay quickly as shown in Figure 1.10b. If the diffusion is slow, then the correlation will decay slowly. In the

above case of Brownian motion, the autocorrelation function can be fit to a simple diffusion model (Equation 1.21)

$$G(\tau) = G(0)(1 + \frac{4D\tau}{s^2})^{-1}(1 + \frac{4D\tau}{u^2})^{-1/2} \quad (1.21)$$

where *G(0)* is the amplitude at $\tau = 0$, *D* is the diffusion coefficient, *s* is the semi-minor axis of the observation volume, and *u* is the semi-major axis of the observation volume. The amplitude gives the inverse of the average number of diffusing particles in the observation volume $G(0) = \langle N \rangle^{-1}$. Since dilute concentrations result in large amplitudes, FCS is more sensitive to dilute concentrations than high concentrations. In contrast, ensemble fluorescence techniques are more sensitive to higher concentrations.

If the semi-major axis *u* is sufficiently large, then the term containing *u* vanishes. In other words, fluorescence fluctuations along the optical axis do not contribute to the autocorrelation function. Only fluorescence fluctuations along the waist of the observation volume contribute to the autocorrelation function. Equation 1.21 simplifies to Equation 1.22.

$$G(\tau) = G(0)(1 + \frac{4D\tau}{s^2})^{-1} \quad (1.22)$$

In the beginning, FCS measurements are always performed on a free dye standard with known diffusion coefficient. The autocorrelation function of the free dye can be fit by Equation 1.22 with a fixed diffusion coefficient to determine the waist, or semi-minor axis. Once the waist is known, FCS measurements can be performed on the actual samples to measure the diffusion coefficient.

If *N* fluorescent species with different brightnesses contribute to the autocorrelation, then the autocorrelation function can be described as Equation 1.23.

$$G(\tau) = \frac{\sum_{i=1}^{N} N_i B_i^2 (1+\frac{4D_i\tau}{s^2})^{-1}}{(\sum_{i=1}^{N} N_i B_i)^2} \quad (1.23)$$

Where B_i is the brightness of the *i*th species and N_i is the number of *i*th species. Due to the presence of particles of different brightnesses, the experimentally measured amplitude will not give the true number of particles. Instead, Equation 1.24 applies.

$$G(0) = \frac{\sum_{i=1}^{N} N_i B_i^2}{(\sum_{i=1}^{N} N_i B_i)^2} = \frac{1}{(\sum_i N_i)} \frac{\langle B_i^2 \rangle}{\langle B_i \rangle^2} = \frac{1}{N_T} \frac{\sigma^2+\mu^2}{\mu^2} \quad (1.24)$$

Where σ^2 and μ are the variance and mean of the probability density function that describes the distribution of brightnesses. As a result, the inverse of *G(0)* deviates from the true number of particles by a factor of $(\frac{\sigma^2+\mu^2}{\mu^2})^{-1}$.

One artifact that can affect FCS measurements is the afterpulse of the photodetector. When a fluorescence photon strikes the photoactive area of the photodetector, a photon detection event occurs in which the optical input is converted to electrical output (electron avalanche). Sometimes, the electrons are trapped in lattice defects in the photoactive area. Then, these electrons are later released by heat or some other mechanism. These released electrons are considered to be spurious photon detection events because they do not indicate true photon detection events. Unfortunately, these spurious photon detection events do occur in response to true photon detection events. Hence, the spurious events appear as an abrupt increase in the autocorrelation at low microsecond lag times. This feature is called the afterpulse. This afterpulse can be minimized by cross-correlation FCS. In cross-correlation FCS, the fluorescence emission in the detection pathway is directed to two photodetectors by a beam splitter. Since there is no reason for the afterpulses from two detectors to be

correlated, the afterpulse effect should disappear when the signals from the two detectors are cross-correlated.[4, 5]

FCS measurements should be performed at low to moderate laser powers to avoid optical saturation of the observation volume. As previously mentioned, the laser should have a Gaussian profile. Therefore, the excitation intensity distribution (EID) should be Gaussian as well. The excitation probability distribution (EPD) describes the probability that a dye in the observation volume will absorb a photon and be excited. Ideally, the EPD will be directly proportional to the EID. The EPD is multiplied with the light-collection efficiency function (CEF) to define the molecule-detection function (MDF). This MDF describes the probability of detecting a fluorescence photon from a dye at a particular position in the observation volume. At a certain laser power (depending on the extinction coefficient of the dyes), the majority of dyes in the observation volume are not in the ground state but in the excited state. As a result, the EPD flattens and no longer has a Gaussian peak. This artifact creates an apparently larger non-Gaussian observation volume. This non-Gaussian MDF will lead to smaller amplitudes and longer diffusion times. Therefore, the laser power should be kept low to avoid these artifacts.[6, 7]

Figure 1.11 describes the FCS setup used in this research. A continuous laser provides the exciting light. A dichroic filter inclined at 45° reflects the excitation into an oil-immersion objective lens. The objective lens focuses the excitation light into a diffraction-limited spot within the sample on a glass coverslip. The same objective lens collects the fluorescence from the diffraction limited spot, and the same dichroic filter transmits the fluorescence. The fluorescence is reflected by a mirror into a 50 μm pinhole. The fluorescence is then guided through an emission filter and to an avalanche

photodioide (APD) detector. The APD detector is connected to a dedicated hardware correlator card which calculates the autocorrelation for logarithmically spaced lag times.

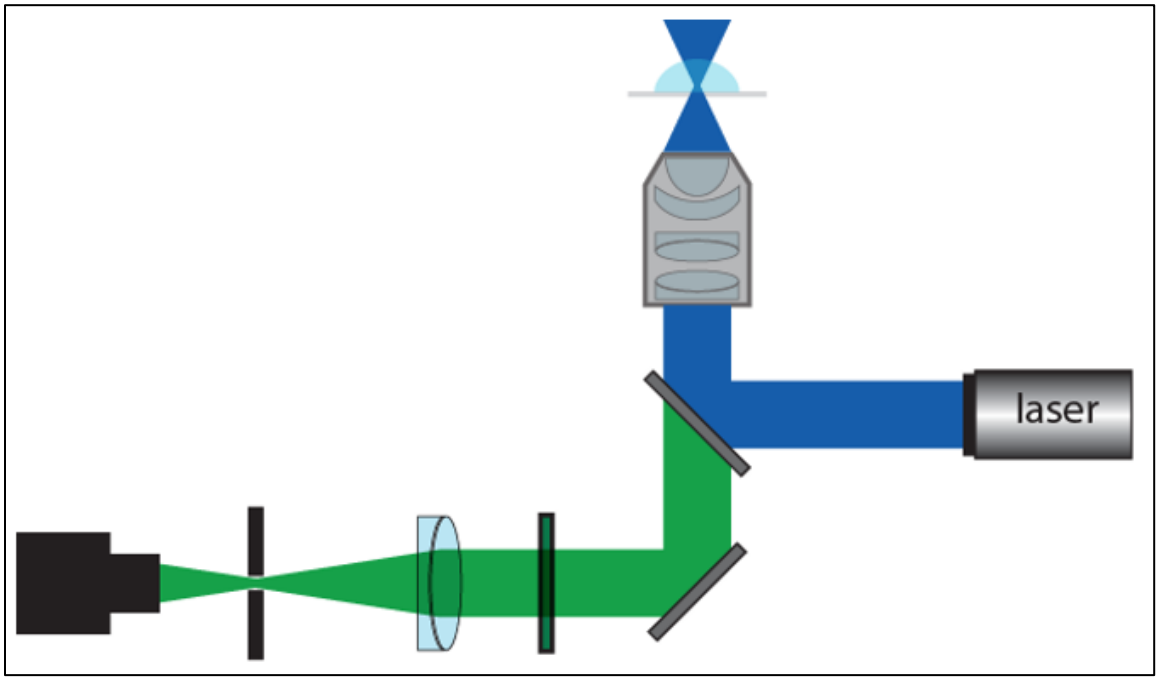

Figure 1.11: FCS Setup. Figure by courtesy of Doug Daniel.

CHAPTER TWO

PHOTOPHYSICS OF RHODAMINE AND BODIPY FLUOROPHORES

2.1 Rhodamine Monomers

Xanthene dyes and rhodamine dyes are commonly used fluorescent dyes/fluorophores. Xanthenes and rhodamines are used for labeling of biological macromolecules such as DNA and proteins and as donors and acceptors in Förster Resonance Energy Transfer (FRET) applications. They have large fluorescence quantum yields and a narrow Stokes shift of 20-30 nm. Both dye structures are shown in Figures 2.1a and 2.1b. Xanthene dyes are organic heterocyclic compounds with a conjugated π-electron distribution. Rhodamine dyes have structures very similar to that of xanthene dyes with two modifications: 1) the addition of amino groups and 2) the addition of a phenyl group. Various reactive groups such as carboxyl groups can be attached to the phenyl ring for labeling. Fortunately, the carboxyphenyl group is almost perpendicular to the plane of the xanthene scaffold. Hence, the carboxyphenyl ring has a negligible impact on xanthene's π-electron system and on xanthene's absorbance and fluorescence properties.[8] In the following paragraphs, the effects of both alkylated amino groups and unesterfied carboxyphenyl groups on the photophysics of rhodamines will be explained.

The absorbance and fluorescence properties of rhodamines with unesterfied carboxyphenyl groups do change with the pH of the solution. In 1981, I. Lopez Arbeloa and P. Ruiz Ojeda studied the different molecular forms of Rhodamine B as a function of pH. The structure of cationic Rhodamine B is shown in Figure 2.1c. Rhodamine B has a carboxyphenyl group and fully alkylated amino groups. At a basic pH, Rhodamine B

was present in a neutral (zwitterion) form with a negatively charged carboxyphenyl group and a positively charged alkylated amino group. At an acidic pH, the carboxyphenyl group was protonated causing the cationic form to become dominant. As the pH decreased, the wavelengths of both the absorption and emission maxima were red-shifted by a few nanometers. At really acidic conditions where the pH was below 2.5, the absorbance spectrum intensity dropped indicating the emergence of a colorless lactone with an interrupted π-electron system.[9] In 1986, I. Lopez Arbeloa studied the absorbance and fluorescence properties of different molecular forms of Rhodamine B in different solvents. Arbeloa attempted to find clear correlations between the absorbance/fluorescence properties of Rhodamine B and the solvent properties. As an example, it was suspected that torsional motion of the alkylated amino groups served as a non-radiative deactivation pathway for the excited state. Therefore, increasing the solvent viscosity should have reduced the torsional motion and increased the fluorescence quantum yield and lifetime. However, a substantial enhancement of fluorescence quantum yield was not observed with solutions of ethylene glycol or butanol. Furthermore, upon transition from ethanol to water, the fluorescence quantum yield dropped even though the two solvents had similar viscosities. Despite the lack of clear correlations between absorbance/fluorescence properties and solvent properties, two clear trends did emerge. 1) The protonated cationic form of Rhodamine B had a lower fluorescence quantum yield compared to that of the neutral (zwitterion) form of Rhodamine B. Arbeloa speculated that the zwitterion form of Rhodamine B had an increased C-N bond order in the terminal alkylated amino groups which reduced the torsional motion of those same amino groups thereby reducing non-radiative deactivation

of the excited state. 2) The colorless lactonic form of Rhodamine B manifested in aprotic solvents such as DMSO and DMF. Arbeloa speculated that only protic solvents can solvate the carboxyphenyl group by hydrogen bonding.[10]

The structure of Rhodamine 6G is shown in Figure 2.1d. Rhodamine 6G differs from Rhodamine B in two major ways. 1) In Rhodamine 6G, the amino groups are only partially alkylated. The photophysics of rhodamines with partially alkylated amino groups or amino groups incorporated in six-membered rings tend to be solvent independent. 2) The carboxyphenyl group has been replaced with an ester phenyl. Therefore, Rhodamine 6G is not expected to display different molecular forms as a function of pH.[8]

In 1989, F. Lopez Arbeloa et al. studied the absorbance and fluorescence properties of Rhodamine 19. The structure of Rhodamine 19 is indicated in Figure 2.1f. Both Rhodamine 6G and Rhodamine 19 have similar structures. The only important difference between the two structures is that Rhodamine 6G has an ester phenyl whereas Rhodamine 19 has a carboxyphenyl. Therefore, Rhodamine 19 was expected to display behavior similar to that of Rhodamine B. Red-shifts of the absorption and emission peaks upon increasing acidic conditions were observed for both aqueous and ethanolic solutions of Rhodamine 19 (as was observed with Rhodamine B as well). With ethanol, the red-shifts were more pronounced. For both aqueous and ethanolic solutions of Rhodamine 19, the fluorescence quantum yields decreased upon increasing acidic conditions (also observed with Rhodamine B).[11]

The structure of Rhodamine 3B is shown in Figure 2.1e. Rhodamine 3B has a structure similar to that of Rhodamine B with one major difference: the carboxyphenyl

group has been esterfied. Like Rhodamine 6G, Rhodamine 3B is not expected to display different molecular forms as a function of pH. In 1991, F. Lopez Arbeloa et al. did a thorough study of the photophysics of Rhodamine 19 (different molecular forms), Rhodamine 6G, Rhodamine B (different molecular forms), and Rhodamine 3B in water/ethanol mixtures. Arbeloa speculated that an interaction between the xanthene moiety and the carboxyl group was responsible for the phenyl ring being nearly perpendicular to the xanthene scaffold. Arbeloa also speculated that the interaction changed the distribution of xanthene's resonance structures. The interaction between the xanthene and the carboxyl drew the positive charge away from the amino groups onto the xanthene and decreased the bond character of the xanthene-amine double bond. This redistribution of xanthene's resonance structures caused the amino groups to transition from a planar structure to a pyramidal structure as shown in Figures 2.1b and 2.1c respectively. With the positive charge stabilized on the xanthene, internal conversion was reduced and fluorescence was enhanced. The interaction strength decreased down the following series: the deprotonated carboxyl group (neutral/zwitterion), the protonated carboxyl group (cation), and the ester. Hence, the interaction strength was strongest with the deprotonated carboxyl group. This trend explained why the deprotonated zwitterion/neutral forms of rhodamines had higher fluorescence quantum yields than the protonated cationic forms. The same trends of interaction strength were observed in ethanol (deprotonated > protonated > ester). However, since ethanol poorly solvated the carboxyl group, the interaction between the xanthene and the carboxyl was stronger in ethanol compared to water. Hence, the rate of internal conversion was lower in ethanol. Arbeloa also speculated that the rhodamines with fully alkylated amino groups

(Rhodamines B and 3B) stabilize the positive charge on the amino group through the inductive effect trapping the amino groups in the planar state and increasing internal conversion. In contrast, for rhodamines with partially alkylated amino groups (Rhodamines 6G and 19), the inductive effect was weaker allowing a stronger contribution of pyramidal amino groups and reducing internal conversion.[12] A 1993 study by Sauer et al. seemed to confirm Arbeloa's speculations. One of the dyes studied by Sauer et al. was Rosamine 1 whose structure is depicted in Figure 2.1g. Rosamine 1 has amino groups incorporated into six-membered rings and a phenyl ring with no substituents. Rosamine 1 displayed a weak fluorescence quantum yield and lifetime. Sauer et al. speculated that with the removal of the carboxyl group, the phenyl ring became nearly coplanar with the xanthene scaffold in the first excited state. Loss of perpendicularity was followed by an increase in the internal conversion and a decrease in the fluorescence quantum yield and lifetime.[13]

In the late 1990s, a new class of fluorophores called Alexa Fluor was released by Molecular Probes. The majority of dyes in this relatively new class were sulfonated rhodamines. The negatively charged sulfonates improved water solubility and minimized dye aggregation by charge repulsion. Protein conjugates of these Alexa Fluor dyes were reported as being brighter than the protein conjugates of traditional rhodamines and cyanines.[14]

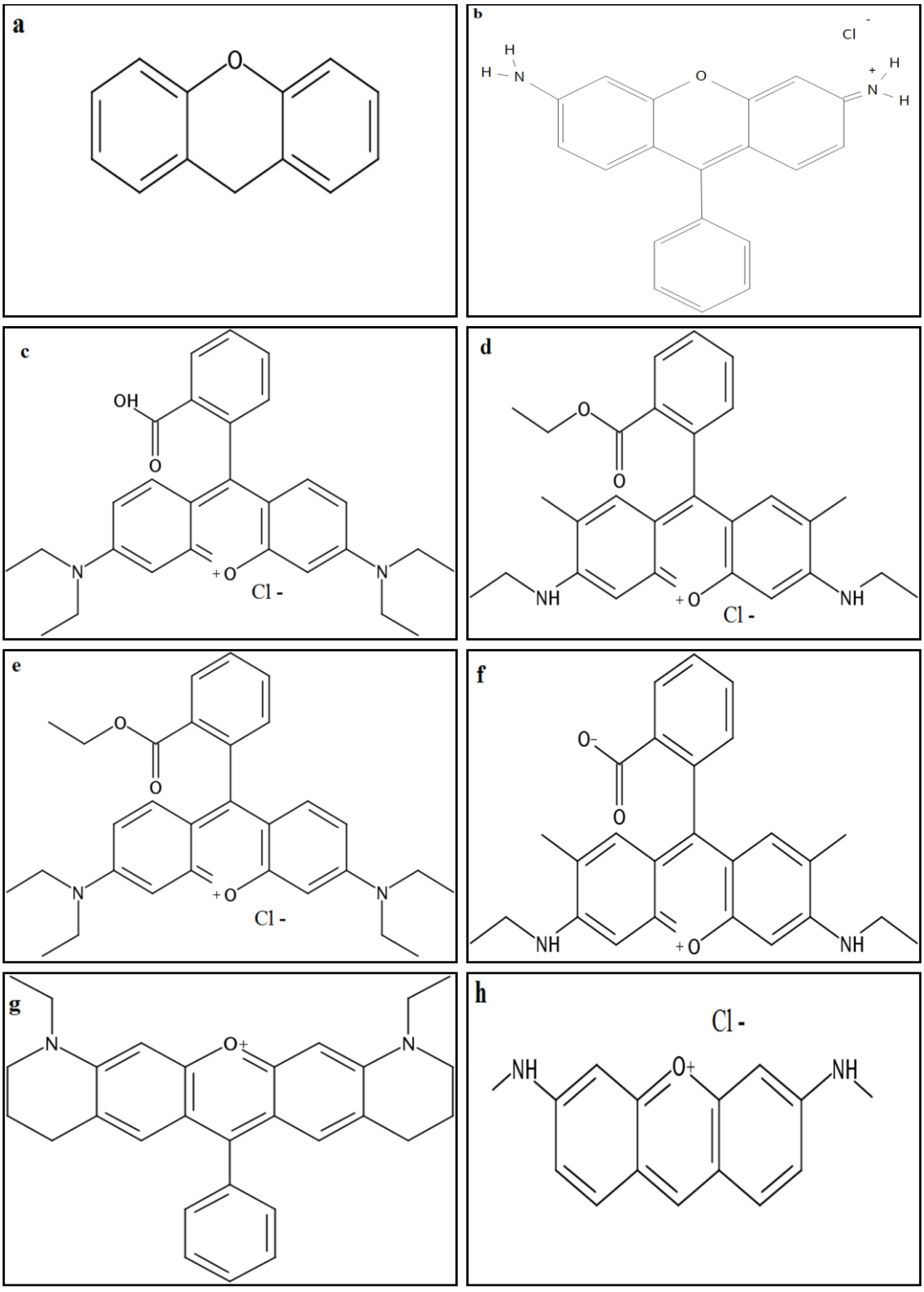

Figure 2.1: Structures of Xanthenes. Xanthene (a), Rhodamine (b), Rhodamine B (c), Rhodamine 6G (d), Rhodamine 3B (e), Rhodamine 19 (f), Rosamine 1 (g), and Acridine Red (h).

2.2 Rhodamine Dimers

A. Absorbance Properties of Rhodamine Dimers

In 1963 and 1966, K. K. Rohatgi and G. S. Singhal studied the behavior of Rhodamine B in water at different concentrations. They observed the emergence of a shorter-wavelength/higher energy peak in the absorbance scans as the Rhodamine B concentration was increased from micromolar to millimolar. They attributed this blue-shifted (hypsochromic) peak to dye aggregation caused by the hydrophobic effect.[15, 16] In 1972, Judith E. Selwyn and Jeffrey I. Steinfeld studied the aggregation equilibria of xanthene dyes and rhodamine dyes. As the concentrations of Rhodamine B and Rhodamine 6G in aqueous solutions at room temperature were increased from micromolar to millimolar, pronounced blue-shifted peaks were observed in the absorbance scans.[17] An example of such a hypsochromic peak in the absorbance scan is depicted in Figure 2.2. For ethanolic solutions of Rhodamine B at room temperature, as the concentration of Rhodamine B was increased from micromolar to millimolar, pronounced red-shifted (bathochromic) peaks were observed in the absorbance scans. Similar bathochromic shifts were observed for ethanolic solutions of Acridine Red (structure shown in Figure 2.1h) at room temperature.[17] In 1982, I. Lopez Arbeloa and P. Ruiz Ojeda studied the aggregation of Rhodamine B in water of basic pH (pH = 12) at room temperature. They observed the same hypsochromic shifts in the absorbance scans of Rhodamine B as the concentration was increased from micromolar to millimolar.[18] In 1982, F. Lopez Arbeloa et al. observed hypsochromic shifts in the absorbance spectra of aqueous solutions (pH = 4) of Rhodamine 6G at room temperature as the concentration was increased from micromolar to millimolar.[19] In 1989, Oscar Valdes-Aguilera and D.

C. Neckers also studied the aggregation behavior of xanthene dyes. They observed similar hypsochromic shifts in the absorbance spectra of aqueous solutions of Rhodamine 6G at room temperature as the concentration was increased from micromolar to millimolar.[20] In 1989, F. Lopez Arbeloa et al. studied the aggregation of Rhodamine 19 in both aqueous and ethanolic solutions. In aqueous solution, as the concentration of Rhodamine 19 was increased from micromolar to twenty micromolar, the aggregation resulted in hypsochromic shifts in the absorbance spectra. In ethanol, bathochromic shifts in the absorbance scans were observed under acidic conditions and under neutral conditions when the concentration was increased from micromolar to millimolar.[11, 21]

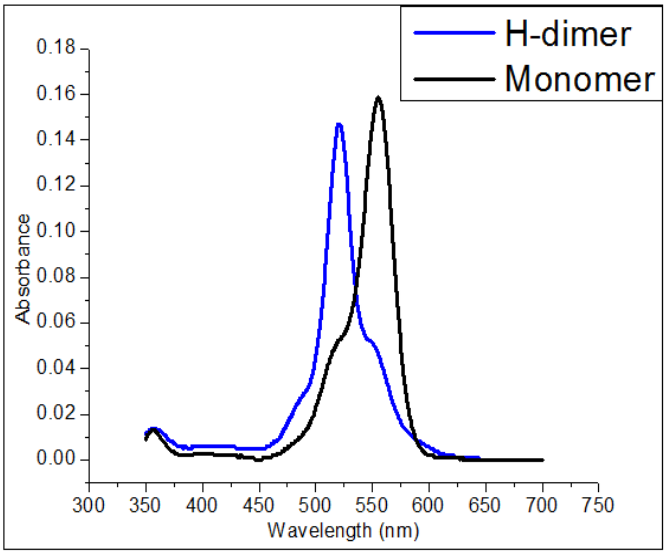

Figure 2.2: Hypsochromic Shift. An Example of a Hypsochromic Shift in the Absorbance Spectrum of a Dye Upon Aggregation.

B. Exciton Splitting in Rhodamine Dimers

In 1964, A.S. Davydov developed the theory of molecular excitons for molecular crystals. His theory described how the excited state would be split if two or more

ground-state molecules interacted in a unit cell.[22] The term "molecular exciton" refers to an excited electron strongly bound to a specific molecule in a Van der Waals aggregate. If an aggregate consists of *N* molecules, then the excited state will be split *N* times. If two ground-state rhodamine monomers were to interact, then their degenerate excited singlet states would experience a resonance splitting into two levels: one exciton singlet state would be below the excited singlet state of the monomer and the other exciton singlet state would be higher than that of the monomer. Typically, only one electronic transition is allowed while the other transition is forbidden. The vector sum of the transition dipoles must be used to determine which transitions are allowed and which are forbidden. In-phase dipoles result in allowed transitions whereas out-of-phase dipoles correspond to forbidden transitions because the transition dipole vector sum is zero, or vanishing. In Figure 2.3a, the case of H-dimers (sandwich-type dimers) with parallel transition dipoles is explored. The out-of-phase dipole arrangement represents an electrostatic attraction (lower exciton singlet state S_1'). However, since the transition dipole vector sum is zero in this out-of-phase arrangement, this lower electronic transition is forbidden. In contrast, the in-phase dipole arrangement represents repulsion (higher exciton singlet state S_1"), but this higher electronic transition is still allowed because the vector sum is non-vanishing. The oscillator strength of the allowed transition is 2f/dimer. Since the higher electronic transition is allowed, H-dimers are expected to display blue/hypsochromic shifts (shorter wavelength/higher energy) in their absorbance scans. In Figure 2.3b, the case of J-dimers with in-line transition dipoles will be explored. The out-of-phase dipole arrangement represents repulsion (S_1") and is forbidden because the vector sum is zero. The in-phase dipole arrangement represents an

electrostatic attraction (S_1') and is allowed because the vector sum is non-vanishing. The oscillator strength of this allowed transition is also 2f/dimer. Since the lower electronic transition is allowed, J-dimers are expected to display red/bathochromic shifts (longer wavelength/lower energy) in their absorbance scans. Dimers with intermediate geometries are expected to have non-vanishing transition moments for both electronic transitions. A careful inspection of Figures 2.3a and 2.3b reveals that H-dimers are nonfluorescent while J-dimers are fluorescent. Figure 2.3c explains why H-dimers are nonfluorescent. In the case of H-dimers, an electronic transition to the higher exciton singlet state (S_1") is followed by rapid internal conversion to S_1'. Since transitions to/from the S_1' state are forbidden for H-dimers, the intersystem crossing becomes the only deactivation pathway available for the dimer. After the intersystem crossing, phosphorescence occurs. In summary, for H-dimers, there is an enhancement of the triplet state excitation and phosphorescence at the expense of the fluorescence. In the case of J-dimers, transitions to/from the S_1' state are allowed, so fluorescence can still occur.[23, 24]

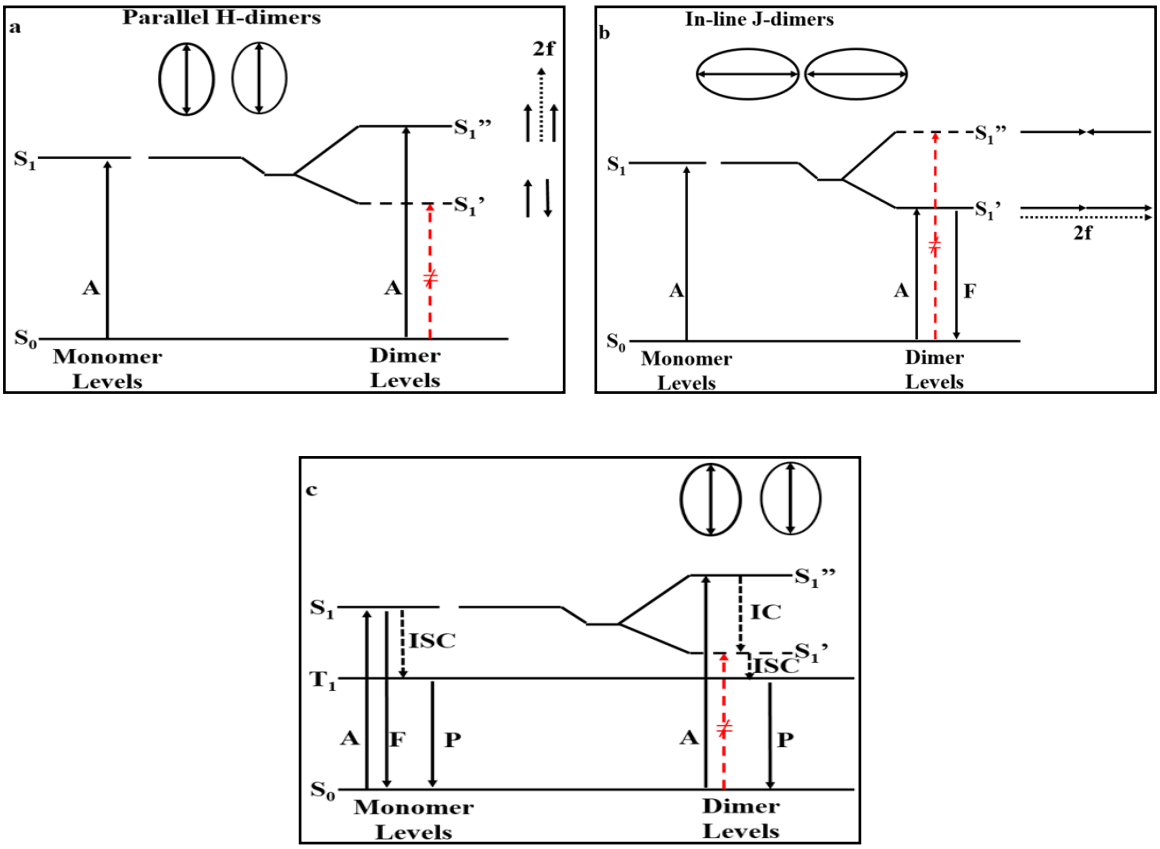

Figure 2.3: Exciton Splitting in H-dimers (a), Exciton Splitting in J-dimers (b), and Quenching of Fluorescence in H-dimers (c). Allowed transitions are depicted as black lines while forbidden transitions are depicted as red dashed lines. Radiative transitions are depicted as black solid lines whereas non-radiative transitions are depicted as black dotted lines.

C. Fluorescence Properties of Rhodamine Dimers

In 1988, F. Lopez Arbeloa et al. studied the fluorescence quenching of Rhodamine 6G in concentrated ethanolic solutions. It was found that dimers and trimers were responsible for the pronounced fluorescence quenching.[25] In 1989, F. Lopez Arbeloa et al. studied the fluorescence quenching of different molecular forms of Rhodamine B in both aqueous and ethanolic solutions. It was determined that the fluorescence quantum yield of Rhodamine B was higher in ethanol than in water and that

higher concentrations in ethanol were required to observe fluorescence quenching. However, once the fluorescence quenching was reached in ethanol, then the fluorescence quenching in ethanol became more pronounced than in water.[26] In 1991, Klaus Kemnitz and Keitaro Yoshibara studied the dimerization of xanthene dyes in nonpolar solvents as a function of solvent, dye concentration, temperature, and nature of the counteranion. The researchers determined that the stacking of xanthene dyes in nonpolar solvents was entropy-driven. They also established other interesting trends. TCSPC measurements indicated that the extent of dimerization increased with temperature. The authors speculated that non-fluorescent H-dimers competed with fluorescent J-dimers. At high temperatures, the fluorescent J-dimers were dominant over the nonfluorescent H-dimers. Dark H-dimers would not contribute to the decay kinetics while fluorescent J-dimers would manifest as really short lifetime components on the order of hundreds of picoseconds. Therefore, the TCSPC decay curves became more quenched with increasing temperature and concentration. Another important contribution was the nature of the counteranion. It was found that small counteranions like chloride enhanced the stacking of Rhodamine 6G more than larger counteranions like perchlorate. Last but not least, it was observed that zwitterionic rhodamines like Rhodamines B and 101 had smaller extents of dimerization.[27] In 2003, Jordi Hernando et al. studied the photophysics of a dimer of tetramethylrhodamine-5-isothiocyanate (5-TRITC). Bulk absorption of $TRITC_2$ in polar solvents revealed H-dimers. However, the excitation scans of $TRITC_2$ in polar solvents almost perfectly overlapped with the absorbance spectra of the monomer TRITC. Those ensemble absorbance and fluorescence measurements indicated two populations of dimers: strongly-coupled nonfluorescent H-dimers and weakly-coupled

fluorescent dimers. Fluorescence confocal scanning microscopy combined with polarization-sensitive detection determined two subpopulations within the weakly-coupled dimers: extended and gauche conformations.[28]

D. Applications of Rhodamine Dimers

Rhodamine dimers have been used for many interesting applications over the years. In 1996, Packard et al. designed and synthesized protease substrates whose cleavage sites were doubly labeled with xanthene dyes forming H-dimers. When serine proteases such as elastase were added, the substrates were cleaved resulting in disruptions of the H-dimers. The disruptions of the H-dimers could be monitored with both absorbance and fluorescence techniques. Upon cleavage of the substrates, the diminution of the H-dimer absorption band could be observed. Furthermore, substantial enhancements of the fluorescence intensity (at least an order of magnitude) were measured. In an interesting biological application, Packard was able to monitor intracellular elastase activity of promyelocytic leukemic cells of the HL-60 line by incorporating these doubly-labeled substrates into the HL-60 cells and recording the concomitant increases in fluorescence intensity with a fluorescence microscope.[29] In 2002, Blackman et al. studied malarial protease substrates doubly labeled with 5- or 6-isomers of iodoacetamidotetramethylrhodamine (IATR). Their goal was to develop a fluorescence-based assay for proteolysis. When the doubly-labeled substrates were digested with proteases like Pronase, reductions of the H-dimer absorption peaks and concomitant 30-fold enhancements of the fluorescence intensity were recorded. Frequency-domain lifetime measurements indicated that the doubly-labeled substrates

had two lifetime components. One lifetime component was around 2.4 ns and the other lifetime component was subnanosecond (on the order of hundreds of picoseconds). The shorter lifetime component was attributed to the rhodamine dimers. The presence of the longer lifetime component suggested that a significant fraction of the doubly labeled interfaces did not result in H-dimers suggesting an equilibrium between monomer and dimer rhodamine states. When the doubly-labeled substrates were cleaved with Pronase, single exponential decays were obtained with a lifetime of around 2.4 ns.[30]

In 1999, Gakamsky et al. studied the class I major histocompatibility complex (MHC-I) protein assembly using a xanthene-derivatized β_2-microglobulin. The β_2-microglobulin was singly labeled with Texas Red. When absorbance scans of β_2m-TR were compared with those of free TR sulfonate, pronounced blue-shifted bands were observed in β_2m-TR. Since β_2m-TR was only singly-labeled, protein oligomerization was speculated to result in dye oligomerization. However, four methodologies reduced the H-dimer absorption band: the addition of urea to β_2m-TR, the heating of β_2m-TR at 37°C, the dilution of β_2m-TR, and the incorporation of β_2m-TR into MHC-1 and a peptide to form a ternary complex. Fluorescence measurements of β_2m-TR confirmed the suspicions of dye oligomerization. Both the excitation and emission spectra of β_2m-TR were inhomogeneous (dependence on excitation and emission wavelength). Furthermore, the excitation spectrum of β_2m-TR had both blue-shifted and red-shifted bands suggesting that the dye oligomerization resulted in intermediate geometries between that of H-dimers and J-dimers. However, when β_2m-TR was incorporated into that ternary complex, both the excitation and emission spectra became homogeneous.[31]

In 2009, Ogawa et al. used the concept of H-dimers to develop fluorescence activatable probes for *in vivo* optical molecular imaging. Proteins such as avidin and trastuzumab were conjugated with rhodamines. A high local dye proximity on the proteins led to H-dimer formation. The protein conjugates of these rhodamines bound to the antigens and receptors on cancer cells' surfaces. The protein complexes were internalized within lysosomes which degraded the protein complexes. Digestion of the protein complexes resulted in disruptions of the H-dimers and concomitant activation of the fluorescence intensity. The proof of the concept was demonstrated with both *in vitro* and *in vivo* fluorescent microscopy studies in cancer cells. For the *in vivo* studies, ovarian tumors in mice were imaged. For these experiments, various rhodamines were tested. It was found that protein conjugates of TAMRA had the greatest tendency to form H-dimers while the protein conjugates of sulfonated Alexa Fluor 488 showed no signs of ground-state dimerization in the absorbance scans. Therefore, the protein conjugates of TAMRA displayed low background fluorescence whereas the protein conjugates of Alex Fluor 488 displayed high background fluorescence.[32]

In 2014, Jennifer K. Binder et al. studied the stability and oligomerization dynamics of DNA processivity clamps like the homodimeric *Escherichia coli* β clamps and the homotrimeric *Saccharomyces cerevisiae* proliferating cell nuclear antigen (PCNA) clamps. Ensemble and single-molecule fluorescence techniques were used to study these clamps. The β clamps singly-labeled and doubly-labeled at the interfaces with TMR were referred to as β-TMR_1 and β-TMR_2 respectively. The PCNA clamps singly-labeled at the interfaces with TMR were referred to as PCNA-TMR_1. FCS measurements of β-TMR_1 and PCNA-TMR_1 were performed in order to calculate the

equilibrium and kinetic parameters for the dissociation equilibria of β and PCNA clamps. The diffusion times obtained from FCS measurements at different protein concentrations indicated protein oligomerization. Additional FCS measurements of β-TMR_1 and PCNA-TMR_1 performed at different incubation times indicated that the homotrimeric PCNA clamp was less stable than the homodimeric β clamp. However, if 1 M NaCl was added to β-TMR_1, then rapid dissociation to monomers was observed suggesting that the electrostatic interactions holding the β clamp dimer together were interrupted by the high ionic strength. Ensemble TCSPC decay curves of β-TMR_1 displayed only two lifetime components: 2.7 ns and 1.1 ns. The first lifetime component 2.7 ns corresponded to the literature values for the fluorescence lifetime of TMR. The second lifetime 1.1 ns was attributed to the protein environment of the TMR probe. In contrast, ensemble TCSPC decay curves of β-TMR_2 displayed a third short lifetime component on the order of hundreds of picoseconds. This subnanosecond lifetime component was attributed to the H-dimers of TMR at the doubly-labeled interfaces. The kinetics of subunit exchange were studied by mixing β-TMR_2 with unlabeled wild-type β clamps and performing TCSPC measurements of these subunit-exchanged β-TMR_2 at different incubation times. From the kinetics of subunit exchange, the lifetime of the β clamp dimer at room temperature in 50 mM NaCl buffer was found to be 43 ± 3 hours. The equilibrium dissociation constant K_d for the β clamp was estimated to be between 6.5-65 pM. Dissociation of β-TMR_2 at the single-molecule level was also studied. After an incubation time of eight hours, more bursts of fluorescence were detected suggesting that a significant fraction of the β clamp dimers had dissociated into monomers with a concomitant disruption of the H-dimers and an activation of the fluorescence.[33]

In 2017, Anirban Purohit et al. used the same ensemble and single-molecule fluorescence techniques to study the electrostatic interactions that hold the β clamp dimers together. It was found that the mutation of a charged amino acid residue (Arg-103) at the interface weakened the interface whereas the mutation of a hydrophilic (Ser-109) and a hydrophobic reside (Ile-305) did not weaken the interface. FCS measurements did not indicate conformational fluctuations at the interface that would aid the binding of clamp loader.[34]

2.3 BODIPY Monomers

Boron-dipyrromethene (BODIPY) dyes cover a wide portion of the visible spectrum (500 nm to 650 nm). BODIPYs are nonpolar, have small Stokes shifts, and are electrically neutral. Because of their electrical neutrality, BODIPY dyes are poorly suited for specific binding to biological macromolecules.[8] The first synthesis of BODIPY dyes is often attributed to Boyer and colleagues. They reported high extinction coefficients and large fluorescence quantum yields for the novel BODIPYs in ethanol.[35] In 1994, Karolin et al. reported long fluorescence lifetimes (5-6 ns) and large fluorescence quantum yields ($\phi_f > 0.8$) for various BODIPYS in various organic solvents.[36] In 1999, F. Lopez Arbeloa et al. noted the high extinction coefficients, large fluorescence quantum yields, and large fluorescence lifetimes of BODIPY in various organic solvents.[37, 38] The structure of the basic BODIPY core is shown in Figure 2.4a. The BODIPY dye used in the publication "Structural Implications on the Properties of Self-Assembling Supramolecular Hosts for Fluorescent Guests" described in Chapter 3 will be referred to as compound **6**. Compound **6**'s real name is 1,3,5,7-tetramethyl-2,6-diethyl with

phenylbipyrromethene difluoroborate. The structure of compound **6** is depicted in Figure 2.4b. It should be noted that the phenyl group is at the *meso* position.

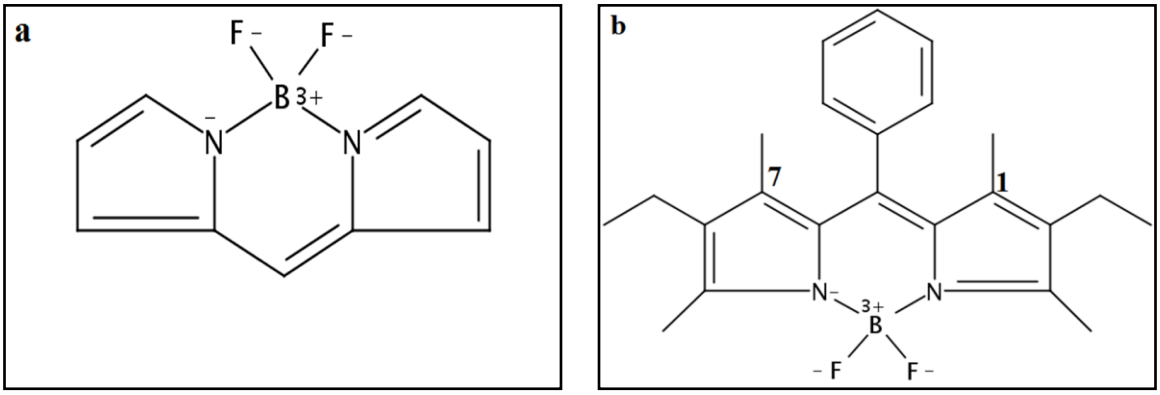

Figure 2.4: Structure of BODIPY core (a) and compound **6** (b).

In 2001, Liang et al. described the synthesis, absorbance properties, and fluorescence properties of compound **6** and other novel BODIPY dyes. Large fluorescence quantum yields were reported for the novel BODIPY dyes including compound **6** in ethanol.[39] In 2006, Röhr et al. reported large fluorescence quantum yields (between 0.8 and 0.9) and long fluorescence lifetimes of around 5 ns for compound **6** in organic solvents such as acetonitrile and hexane.[40] It was found that the presence of the phenyl group in compound **6** increased the photostability of the BODIPY dye and that compound **6** displayed strong fluorescence in organic solvents.[41, 42] X-ray diffraction studies of BODIPY dyes very similar in structure to that of compound **6** indicated that the *meso*-phenyl ring is nearly perpendicular to the BODIPY moiety due to steric factors when substituents are present at the 1 and 7 positions.[43, 44] Based on the experimental trends observed with the rhodamine dyes, it is reasonable to speculate that the perpendicular phenyl ring will have a negligible impact on BODIPY's conjugated π-

electron system. In fact, fluorescence studies of BODIPY dyes with *meso*-phenyl rings but no substituents at positions 1 and 7 revealed very low fluorescence quantum yields and very low fluorescence lifetimes. Bahaidarah et al. speculated that rotation of the *meso*-phenyl ring caused the dipyrrin core to buckle leading to enhanced radiationless decay and that the placement of substituents at positions 1 and 7 prevented the rotation of the *meso*-phenyl ring.[45]

2.4 BODIPY Dimers

In 2002, Mikhalyov et al studied the absorbance and fluorescence properties of mono- and bis-BODIPY labeled diaminocyclohexane. When bis-BODIPY was dissolved in mixtures of methanol and water, a blue-shifted absorption band manifested. The magnitude of this band increased with increasing water, and the fluorescence intensity decreased. These experimental observations were consistent with the formation of nonfluorescent ground-state H-dimers. The absorbance and fluorescence properties of mono-BODIPY labelled oleoyl glyceride in pure solvents and solvent mixtures revealed the existence of another ground-state dimer similar to that of a J-dimer with red-shifted absorption.[46] In 2006, Marushchak et al. did a more thorough photophysical study with these mono- and bis-BODIPY labeled diaminocyclohexane. The fluorescence lifetimes of these mono- and bis-BODIPYs were measured in pure organic solvents and organic solvent/water mixtures at different emission wavelengths. The TCSPC decay curves of the mono-BODIPYs were monoexponential, but the bis-BODIPYs' decay curves were multi-exponential with 3-4 lifetime components. Furthermore, as the content of water increased and as the wavelength of the collected emission increased, the contribution of

the shortest lifetime component grew. The authors attributed these trends to the formation of BODIPY excimers (excited state dimers) in the presence of water. Since excimers typically have short fluorescence lifetimes and red-shifted emission, the contribution of excimers to the TCSPC decay curve grew as the wavelength of collected emission was increased with a concomitant shortening of the average fluorescence lifetime.[47] In 2006, Röhr et al. synthesized bichromophoric dimers of BODIPY connected by a disulfide bridge between the two *meso*-phenyl rings. The positions of the disulfide bridge were varied from the *ortho* to the *para* position. When TCSPC measurements were performed in polar and weakly polar organic solvents, the *para*-substituted analogues were found to have only one fluorescence lifetime distribution. The *ortho*-substituted analogies also displayed only one fluorescence lifetime distribution in weakly polar solvents. However, in polar solvents, the *ortho*-substituted analogues displayed two lifetime distributions. The first lifetime distribution was similar to that of *para*-substituted analogues and the *ortho*-substituted analogues in weakly polar solvents while the second lifetime distribution was very short. The authors attributed the long and short fluorescence lifetimes of the *ortho*-substituted analogues to elongated and sandwich geometries respectively.[40] In 2015, Bell et al. studied the encapsulation of BODIPY dyes in polynorbornene micelles. They found that BODIPY dyes formed nonfluorescent ground-state H-aggregates in organic solvent/water mixtures as evidenced by the appearance of a blue-shifted absorption peak. X-ray diffraction studies confirmed antiparallel stacking. Interestingly, the presence of polynorbornene micelles in the organic solvent/water mixtures established a partition equilibrium between the aqueous phase and the polymer. Over time, a diminution of the H-dimer absorbance peak and

concomitant increases in the fluorescence intensity were observed suggesting that the aqueous H-aggregates were incorporated into the polymeric micelles and disassociated into monomeric dyes.[48]

2.5 The Connection Between Research Projects Described in Chapters 3 and 5

Chapter 3 details a spectroscopic investigation of the photophysics of BODIPY dyes noncovalently encapsulated inside polymeric micelles. Chapter 3 is also a Langmuir publication "Structural Implications on the Properties of Self-Assembling Supramolecular Hosts for Fluorescent Guests." The permission to use this publication as a chapter in my thesis has been granted by the publisher and co-authors. Their permission is displayed in Appendix A.

Chapter 4 is the Supporting Information section for "Structural Implications on the Properties of Self-Assembling Supramolecular Hosts for Fluorescent Guests."

Chapter 5 details a spectroscopic investigation of the interchromophoric interactions at the doubly-labeled interfaces of *E. coli* DNA Processivity β clamps for four rhodamine dyes: TMR, TMR C6, Alexa Fluor 546, and Alexa Fluor 488.

Chapter 6 is the Supporting Information section for the β clamp project.

As one can see, both Chapters 3 and 5 study the photophysics of BODIPY dyes and rhodamine dyes when they are in close proximity to each other. Understanding interchromophoric interactions is very important. Sometimes over-labeling of biological macromolecules with fluorophores can result in artifacts in both the absorbance and fluorescence properties. Understanding the signatures of BODIPY aggregates and rhodamine aggregates will help identify the artifacts in one's measurements.

CHAPTER THREE

LANGMUIR

"STRUCTURAL IMPLICATIONS ON THE PROPERTIES OF SELF-ASSEMBLING SUPRAMOLECULAR HOSTS FOR FLUORESCENT GUESTS"

Sicheng Tang,[†,§] Bryan Donaphon,[‡,§] Marcia Levitus[*,‡] and Françisco M. Raymo[*,†]

Laboratory for Molecular Photonics, Department of Chemistry, University of Miami, 1301 Memorial Drive, Coral Gables, Florida, 33146-0431 and School of Molecular Sciences and The Biodesign Institute, Arizona State University, Tempe, Arizona, 85287-5601

E-Mail: Marcia.Levitus@asu.edu; fraymo@miami.edu

Abstract: Nine amphiphilic macromolecules with decyl and oligo(ethylene glycol) side chains, randomly distributed along a common poly(methacrylate) backbone, were synthesized from the radical co-polymerization of appropriate methacrylate monomers. These resulting amphiphilic constructs differ in (1) the ratio between their hydrophobic and hydrophilic components, (2) the length of their oligo(ethylene glycol) chains and/or (3) the molecular weight. When the ratio between hydrophobic and hydrophilic segments is comprised between 6:1 and 1:2, the macromolecules assemble spontaneously into particles with nanoscaled dimensions in neutral buffer and capture hydrophobic borondipyrromethene chromophores in their interior. However, the critical concentration required for the assembly of these supramolecular hosts as well as their hydrodynamic diameter, supramolecular weight and number of constituent macromolecular building

† University of Miami
‡ Arizona State University
§ Contributed equally to this work
* Correspondence authors

blocks all vary monotonically with the ratio between hydrophobic and hydrophilic components. Specifically, the critical concentration decreases and the other three parameters increase as the relative hydrophobic content raises. Furthermore, an increase in the relative hydrophobic content also discourages interchromophoric interactions between entrapped guests in both ground and excited states as well as delays access of potential quenchers. In fact, these observations demonstrate that the hydrophobic components must be in excess over their hydrophilic counterparts for optimal supramolecular hosts to be assembled. Indeed, a ratio of 6:1 between the numbers of decyl and oligo(ethylene glycol) side chains appears to be ideal for this particular structural design. Under these conditions, supramolecular hosts assemble spontaneously even at relatively low polymer concentrations and their fluorescent guests do not escape into the bulk aqueous solution, despite the reversibility of the noncovalent interactions holding the supramolecular container together. Thus, these systematic investigations provide invaluable structural guidelines to design self-assembling supramolecular hosts with optimal composition for the effective encapsulation of fluorescent guests and can lead to ideal delivery vehicles for the transport of imaging probes to target locations in biological samples.

Introduction

The covalent incorporation of hydrophobic and hydrophilic components within the same macromolecular skeleton results in the formation of amphiphilic polymers.[49-52] In aqueous solutions at appropriate concentrations, these macromolecules can assemble into particles with nanoscaled dimensions. Noncovalent contacts between the hydrophobic domains of independent polymer chains bring multiple macromolecular

components together in the form of discrete nanoparticles to avoid their direct exposure to water. Concomitant solvation of the hydrophilic counterparts ensures the dispersion of the resulting supramolecular assemblies in the aqueous medium and prevents their further association into large aggregates. In the process of assembling, the amphiphilic components can capture hydrophobic molecules and position them in the interior of the nanostructured assemblies. Once encapsulated, the molecular guests can be transported by their supramolecular host across hydrophilic environments. In fact, the unique properties of self-assembling nanoparticles of amphiphilic polymers can be exploited to transfer, otherwise insoluble, molecules into aqueous phases and carry them across physiological media to target locations in biological specimens. Indeed, these supramolecular constructs are becoming invaluable vehicles for the delivery of contrast agents and/or drugs in a diversity of diagnostic and/or therapeutic applications.[53-56]

Self-assembling nanoparticles of amphiphilic polymers can capture hydrophobic chromophores in their interior and transfer them into water.[57] The supramolecular host around the encapsulated molecular guests protects them from the aqueous environment and, generally, preserves their photochemical and photophysical properties. In fact, this strategy permits the modular assembly of supramolecular constructs with multiple chromophoric subunits in close proximity and the engineering of photoresponsive systems with properties that would not be possible to replicate with the individual chromophoric components on their own.[58-78] In our laboratories, we followed similar experimental protocols to encapsulate fluorescent, photochromic and/or photocleavable guests inside such supramolecular hosts.[79-89] We demonstrated that the photochemical and photophysical properties of the entrapped species can be exploited to (1) modulate

fluorescence inside living cells with optical control,[79] (2) image the resulting nanostructured constructs with subdiffraction resolution,[81-83] (3) monitor their ability to exchange their constituent components in the intracellular space[84, 86-88] and (4) probe their dynamics within hydrogels or developing embryos in real time.[85] In all these experiments, however, we relied exclusively on one structural design for the self-assembling amphiphilic building blocks. Specifically, we synthesized a poly(methacrylate) backbone with a random distribution of decyl and oligo(ethylene glycol) side chains. This particular polymer forms supramolecular hosts with fast kinetics in neutral buffer that are capable of entrapping a diversity of hydrophobic guests and transport them from the extracellular into the intracellular space. Such behavior is a consequence of the amphiphilic character engineered into the macromolecular construct, which, in turn, is related to the relative amount of hydrophobic and hydrophilic chains as well as to their lengths. In principle, the modification of these parameters should (1) have an influence on the ability of the amphiphilic components to associate, (2) control the physical dimensions and stability of the resulting supramolecular hosts, (3) dictate the nature of the environment surrounding the entrapped guests and their exposure to the aqueous phase as well as (4) affect the cellular uptake and intracellular localization of the nanocarriers and their cargo. Thus, a systematic investigation of the influence that the structural design of the individual amphiphilic building blocks can have on the properties of the corresponding nanoparticles can provide fundamental insights on these fascinating supramolecular systems and, possibly, guide the optimization of these promising delivery vehicles. On the basis of these considerations, we envisaged the possibility of synthesizing homologous series of macromolecules, differing in their amphiphilic

character, and investigating their ability to form supramolecular hosts for fluorescent guests in aqueous solutions. In this article, we report the preparation and structural characterization of these polymers together with spectroscopic investigations of their assembly into nanostructured hosts for borondipyrromethene (BODIPY) guests.

Results and Discussion

Design, Synthesis and Structural Characterization. Macromolecules **1** and **2** (Figure 3.1) incorporate a random distribution of hydrophobic and hydrophilic components along a common poly(methacrylate) backbone. They differ in the number of repeating units integrated within their oligo(ethylene glycol) chains (*l* in Figure 3.1). They were prepared by the radical co-polymerization of **3** and either **4** or **5**, under the influence of azobis(*i*-butyronitrile) (AIBN), in tetrahydrofuran (THF). In both instances, various amounts of **3** (0.05–3 mmol) were reacted with fixed aliquots of either **4** or **5** (0.5 mmol) and AIBN (0.03 mmol) at 75 °C for 3 days to produce polymers (**1a**, **1b**, **1d–f** or **2a–c** in Table 3.1) with a ratio between hydrophobic and hydrophilic components (*m*:*n* in Figure 3.1) ranging from 8:1 to 1:3. For each macromolecule, *m*:*n* was estimated from the integrals of the resonances associated with the terminal methyl protons of the side chains in the corresponding ^{1}H nuclear magnetic resonance (NMR) spectrum. As an example, the ^{1}H NMR spectrum (Figure 3.2) of **1b**, recorded in deuterated chloroform, shows peaks at 0.88 and 3.39 ppm for the protons of the methyl groups at the termini of the hydrophobic and hydrophilic chains respectively with relative intensities corresponding to a *m*:*n* ratio of 4:1. Furthermore, the spectrum does not reveal any signals at chemical shifts greater than 5.0 ppm, where olefinic protons are expected to resonate, indicating

that any unreacted methacrylate monomers are effectively separated from the corresponding polymer in the purification steps.

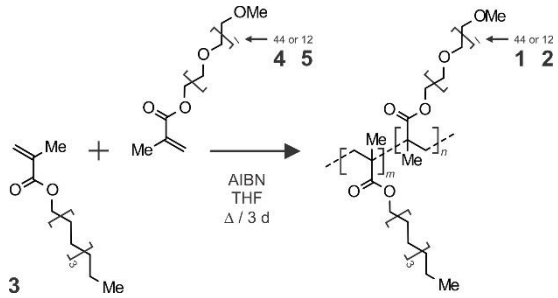

Figure 3.1: Synthesis of **1** or **2** from **3** and **4** or **5** respectively.

Table 3.1: Structural parameters associated with **1a–f** and **2a–c**.

	m:*n* [a]	M_n [b] (kDa)	PDI [b]	D_H [c] (nm)	W_S [d] (kDa)	I_S [c]	N_M [e]	C_c [f] (μg mL^{-1})
1a	6:1	19	1.28	36	1130	0.24	59	7.5
1b	4:1	21	1.32	26	580	0.25	26	16.7
1c	4:1	81	1.11	20	716	0.27	8.8	7.1
1d	1:1	21	1.16	10	53	0.51	2.5	19.3
1e	1:2	17	1.16	7	23	0.88	1.3	76.8
1f [g]	1:3	22	1.23	6	16	0.55	0.7	—
2a [h]	8:1	23	1.14	—	—	—	—	—
2b	3:1	19	1.26	14	109	0.24	5.7	12.9
2c	1:1	19	1.16	11	88	0.32	4.6	9.5

[a] The ratio (*m*:*n*) between the hydrophobic and hydrophilic components of each macromolecule was determined by ^{1}H NMR spectroscopy in $CDCl_3$. [b] The average number molecular weight (M_n) and polydispersity index (PDI) of the macromolecules were determined by GPC in THF against monodisperse polystyrene standards (2,700–200,000, ref.[90]). [c] The hydrodynamic diameter (D_H) and "supramolecular" polydispersity index (I_S) of the nanoparticles were determined by DLS in PBS (ref.[90]). [d] The average "supramolecular" weight (W_S) of the nanoparticles was determined by SLS in PBS. [e] The number (N_M) of macromolecules per nanoparticles is the ratio between W_S and M_n. [f] The critical concentration (C_c) was determined by emission spectroscopy in PBS and the presence of **6**. [g] **1f** is not able to solubilize **6** in PBS and the corresponding C_c could not be determined. [h] **2a** is not soluble in PBS and the corresponding D_H, W_s, I_S, N_M and C_c could not be determined.

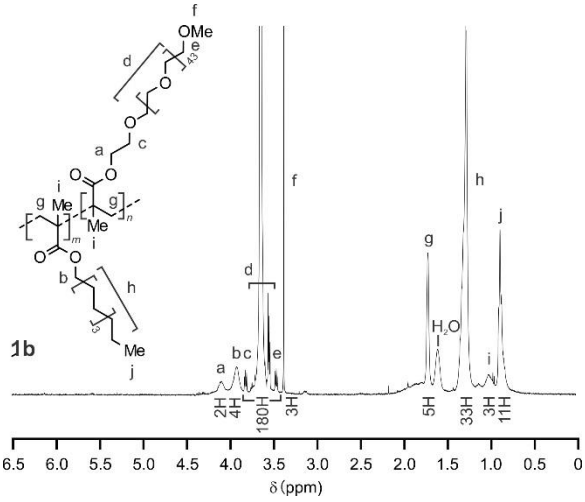

Figure 3.2: ^{1}H NMR spectrum (400 MHz, $CDCl_3$, 25 °C) of **1b**.

Gel permeation chromatography (GPC) of THF solutions of **1a**, **1b**, **1d**–**f** and **2a**–**c** indicates their number-average molecular weight (M_n in Table 3.1) to range from 17 to 23 kDa with a polydispersity index (PDI in Table 3.1) varying from 1.14 to 1.32.[90-92] In order to assess the influence of M_n on the ability of the amphiphilic macromolecules to form nanoparticles (*vide infra*), **3** and **4** were reacted in the presence of a tenth of the original amount of AIBN, under conditions otherwise identical to those employed for the preparation of **1b**, to generate **1c**. The *m*:*n* of both polymers is 4:1, but the M_n of **1b** is only 22 kDa while that of **1c** is 81 kDa.

All macromolecules readily dissolve in aqueous solution with the exception of **2a**. This particular polymer has a *m*:*n* of 8:1 in conjunction with a *l* of 12. Therefore, it is the amphiphilic construct with the most pronounced hydrophobic character out of the nine macromolecules investigated. Dynamic light scattering (DLS) measurements (Figures 4.1 and 4.2) on phosphate buffer saline (PBS) solutions of the other eight polymers, at a concentration of 0.5 mg mL^{-1}, indicate the hydrodynamic diameter (D_H in Table 3.1) to range from 6 to 36 nm with a polydispersity index (I_S) varying from 0.24 to 0.88.[90-92]

Interestingly, D_H increases linearly with *m*:*n* for **1** (Figure 3.3) and remains approximately constant for each polymer solution, maintained in the dark at ambient temperature, over the course of up to 4 days (Figure 4.3). A similar trend is observed also for the D_H of **2**, which drops from 14 to 11 nm with a decrease in *m*:*n* from 3:1 to 1:1. These results demonstrate that the hydrophobic character of these amphiphilic constructs controls their ability to aggregate into nanostructured particles in aqueous solution and that the physical dimensions of the resulting supramolecular assemblies increase with the relative content of hydrophobic components. Consistently, static light scattering (SLS) measurements reveal that the "supramolecular" weight (W_S in Table 3.1) of the resulting assemblies also increases monotonically with *m*:*n* (Figure 3.3) to range from 16 to 1130 kDa for **1**. The ratio between W_S and M_n for each polymer suggests that the average number (N_M) of amphiphilic components in each nanostructured assembly varies from 2.5 to 59 and, yet again, increases monotonically with *m*:*n*. For **1e** and **1f**, however, W_S and M_n are almost identical, indicating that these particular polymers remain isolated in aqueous solution instead of assembling into supramolecular aggregates. In fact, they are significantly more hydrophilic than any of the other macromolecules with *m*:*n* of 1:2 and 1:3 respectively.

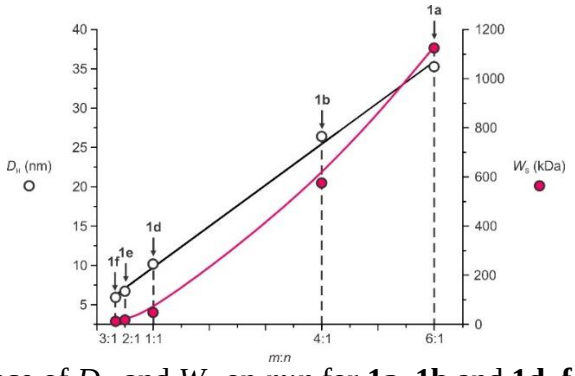

Figure 3.3: Dependence of D_H and W_S on *m*:*n* for **1a**, **1b** and **1d**–**f** (0.5 mg mL^{-1}) in PBS at 22 °C.

Comparison of **1b** and **1c**, which have the same *m*:*n* but different M_n, shows minor differences in D_H and W_S but a significant change in N_M. Up to 26 independent macromolecules are required on average to form a single nanoparticle of **1b**, while only 8.8 are sufficient for **1c**. Thus, the elongation of the macromolecular backbone of the individual amphiphilic building blocks reduces the number of separate components needed for the noncovalent assembly of one nanoparticle.

Noncovalent Encapsulation of Fluorescent Chromophores. The absorption and emission spectra of **6** in THF (Figure 3.4) show maxima at 524 and 536 nm respectively. Essentially the same bands are observed also if **6** is combined with appropriate amounts of **1a**–**e**, **2b** or **2c** in PBS (Figure 3.4). In fact, the wavelengths (λ_{Ab} and λ_{Em} in Table 3.2) of the absorption and emission maxima detected in aqueous media, with the amphiphilic macromolecules, remain close to those measured in organic solution, without the polymers. However, the amount of polymer required to enable the spectroscopic detection of the, otherwise insoluble, chromophore in PBS changes with the amphiphilic character of the macromolecular construct. For example, the emission intensity (Figure 3.5), detected after treating a fixed aliquot of **6** with PBS solutions containing increasing amounts of either **1a** or **1d**, raises abruptly above a critical concentration (C_c in Table 3.1) of either 7.5 or 19.3 μg mL^{-1} respectively. These observations suggest that the amphiphilic macromolecules form supramolecular hosts, capable of capturing the fluorescent guests and allowing their detection in the aqueous phase, only at concentrations greater than the corresponding C_c. In agreement with this interpretation, DLS measurements (Figure 3.5) show that D_H increases by one order of magnitude as the concentration of either **1a** or **1d** raises above the corresponding C_c. Interestingly,

comparison of the C_c values determined with this protocol for **1a**, **1b**, **1d** and **1e** clearly indicates that this parameter increases with a decrease in *m*:*n*. Specifically, C_c varies from 7.5 to 76.8 μg mL^{-1} with a change in *m*:*n* from 6:1 to 1:2 (Table 3.1), suggesting that the hydrophobic content of the macromolecular constructs controls their ability to aggregate into supramolecular hosts for **6**. In fact, even relatively large concentrations of **1f**, which is the polymer with the most pronounced hydrophilic character, cannot solubilize the fluorescent chromophore in aqueous environments to allow its detection. In agreement with this interpretation, the stability of the nanocarriers and their ability to retain their fluorescent cargo also appear to vary with *m*:*n*. At concentrations greater than the corresponding C_c in PBS, the emission intensity detected for **6** in the presence of **1a** remains constant for hundreds of minutes (Figure 4.4), while it gradually decreases over time in the presence of **1e**. Thus, nanocarriers of the polymer with a predominant hydrophobic character (*i.e.*, **1a**) retain their integrity and hold their cargo in the aqueous phase, while nanoparticles of the macromolecules with a predominant hydrophilic character (*i.e.*, **1e**) slowly lose their fluorescent guests with a concomitant decrease in the emission intensity.

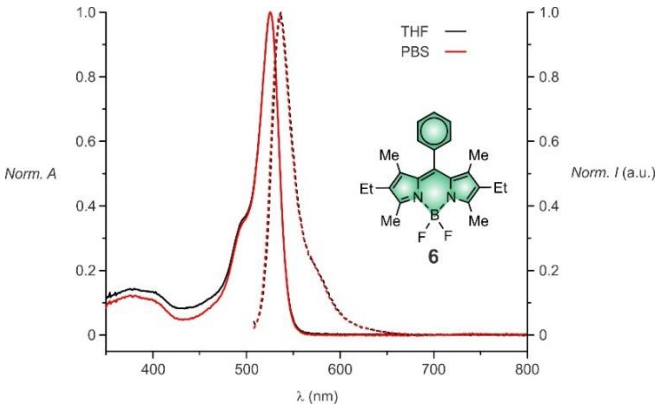

Figure 3.4. Normalized absorption and emission (λ_{Ex} = 500 nm) spectra of either **6** (1 μM) in THF or nanoparticles of **1a** (0.5 mg mL^{-1}), containing **6** (0.34 μM), in PBS recorded at 25 °C.

Table 3.2: Photophysical parameters for **6** encapsulated within nanoparticles of **1a**–**e**, **2b** and **2c** [a].

	λ_{Ab} [b] (nm)	λ_{Em} [b] (nm)	N_G [c]	ϕ [d]	K_{SV} [e] (M^{-1})
1a	526	538	0.63 (5.28)	0.59	72
1b	525	539	0.20	0.60	56
1c	525	538	0.47	0.72	—
1d	525	537	0.02	0.39	29
1e	526	539	0.005 (0.13)	0.09	8
2b	525	537	0.05	0.78	—
2c	525	539	0.04	0.73	—

[a] Absorption and emission spectra were recorded after combining CH_2Cl_2 solutions of **6** (0.1 mM, 1 μL for λ_{Ab}, λ_{Em}, N_G, ϕ and 10 μL for K_{SV}) and one of the polymers (2.5 mg mL^{-1}, 0.2 mL), distilling the solvent off under reduced pressure, dispersing the residue in PBS (1 mL) and passing the resulting dispersion through a nanoporous membrane. The concentration of **6** in the filtrate was estimated from the absorbance at λ_{Ab}, using the molar absorption coefficient measured for this compound in THF. That of the polymer was 0.5 mg mL^{-1} in all instances. [b] The wavelengths of the absorption (λ_{Ab}) and emission (λ_{Em}) maxima were determined in PBS at 25 °C. In THF without macromolecules, λ_{Ab} and λ_{Em} are 524 and 536 nm respectively. [c] The average number (N_G) of fluorophores per nanoparticle is the ratio between the molar concentrations of the molecular guests and the supramolecular hosts (ref.[93]). The values listed in parenthesis for **1a** and **1e** were determined at the dye-loading (concentration of **6** = 2.3 μM) used for the lifetime (Figure 3.7) and FCS (Figure 3.8) experiments. [d] The fluorescence quantum yield (ϕ) was determined against a rhodamine 6G standard. In the absence of the macromolecules, ϕ is 0.73 and 0.50 for **6** and **8** respectively in THF and it is 0.58 for **8** in PBS. [e] The Stern–Volmer constant (K_{SV}) was determined from plots (Figure 4.9) of the relative emission intensity against the concentration of NaI in PBS at 25 °C. Under the same conditions without the macromolecules, K_{SV} is 14 M^{-1} for **8** (Figure 4.11).

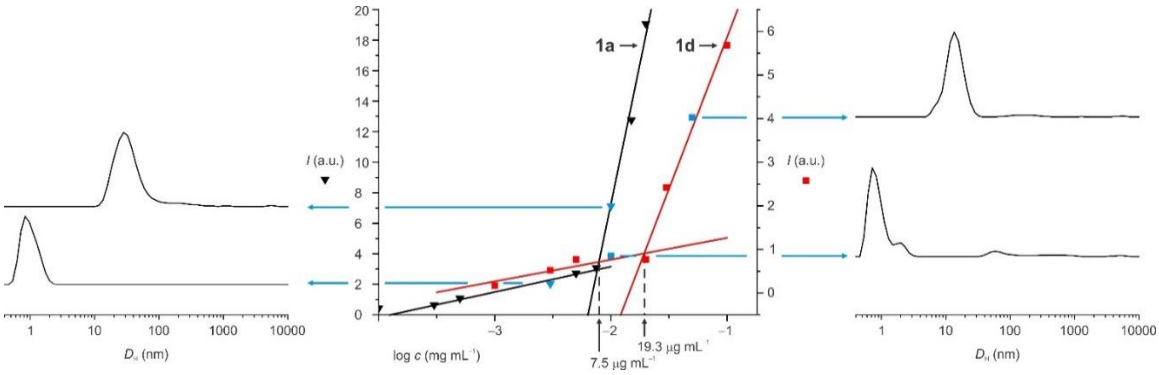

Figure 3.5: Plots of the emission intensity (λ_{Ex} = 500 nm, λ_{Em} = 540 nm), recorded at 25 °C after combining CH_2Cl_2 solutions of **6** (0.1 mM, 0.1 mL) and either **1a** or **1d** (25 μg mL^{-1}, 4–800 μL or 2.5 mg mL^{-1}, 12–25 μL), distilling the solvent off under reduced pressure, dispersing the residue in PBS (1 mL) and passing the resulting dispersion through a nanoporous membrane, against the polymer concentration and statistical distribution of D_H at the four concentrations indicated in the chart determined by DLS.

Samples for the spectroscopic measurements (Table 3.2 and Figure 3.4) were prepared by combining aliquots of dichloromethane solutions of **6** and one of the amphiphilic polymers, distilling the organic solvent off under reduced pressure, dispersing the residue in PBS and filtering the resulting dispersion through a nanoporous membrane. In these particular experiments, the amount of fluorescent guest in the initial organic solution was 0.08% w/w, relative to the corresponding amphiphilic macromolecule. However, only a fraction of the water-insoluble fluorophores is captured by the water-soluble macromolecules and transported into the aqueous phase. Nonetheless, the concentration of **6** in the final solutions can be determined from the absorbance at the corresponding λ_{Ab}, using the molar absorption coefficient measured in THF, to estimate the average number (N_G in Table 3.2) of fluorescent guests per supramolecular host. The resulting values of N_G range from 0.005 to 0.63 for **1a**–**d**, **2b** and **2c**.[93] These particular loading conditions ensure a relatively high fluorescence

quantum yield (ϕ in Table 3.2). Indeed, ϕ varies from 0.39 to 0.78 and, in some instances, approaches the value determined for **6** in THF (*i.e.*, 0.78).

The behavior of **1e** is instead significantly different. This particular polymer has N_G and ϕ of only 0.005 and 0.09 respectively (Table 3.2) at identical loading conditions.[93] Presumably, the pronounced hydrophilic character of this amphiphilic macromolecule limits the ability of the resulting supramolecular hosts to accommodate fluorescent guests and to protect them from the surrounding aqueous environment. In agreement with this interpretation, comparison of the dependence of the absorption and emission spectra (Figure 3.6) on guest loading for **1a** and **1e** shows significant differences. For the polymer with predominant hydrophobic character (*i.e.*, **1a**), the characteristic BODIPY absorption grows with guest loading without shifting. The shape of the spectrum recorded at low guest loading is identical to that observed in either THF (Figure 3.4) or ethanol, indicating that **6** is present predominantly as a monomer inside the nanoparticles. At higher concentrations, however, the absorption spectrum shows an increase in the contribution of the shoulder at 495 nm. This trend is indicative of ground-state dimerization of the BODIPY chromophore[46] and is obvious from the bottom panel of Figure 3.6, which plots the ratio between the absorbance values (A_{495} and A_{527}) at 495 and 527 nm as a function of guest loading. Ratios (A_{495}/A_{527}) of 0.30 and 0.70 were measured in ethanol and in an ethanol/water (1:10, v/v) mixture respectively (Figure 4.5). The spectral characteristics of the dimer (*i.e.*, high A_{495}/A_{527} ratio) are evident even at low guest loading for the macromolecule with predominant hydrophilic character (*i.e.* **1e**). Even more, the band shifts bathochromically at high guest concentrations (Figure 4.5), indicating strong interchromophoric interactions that arise from exposure to the

surrounding aqueous buffer. These interactions result in fluorescence self-quenching, as evidenced by the significantly lower fluorescence intensity measured at large guest concentrations (Figure 3.6) in **1e**, but not **1a**. Put together, these observations suggest that the chromophores remain fairly isolated from each other within nanoparticles of **1a** at moderate loading ratios, but not at high loads where the A_{495}/A_{527} ratio shows signs of aggregation. In the case of **1e**, on the other hand, pronounced electronic interactions in the ground state lead to changes in the absorption spectrum and depressive effects on the radiative efficiency, even at the lowest guest concentration investigated in this study.

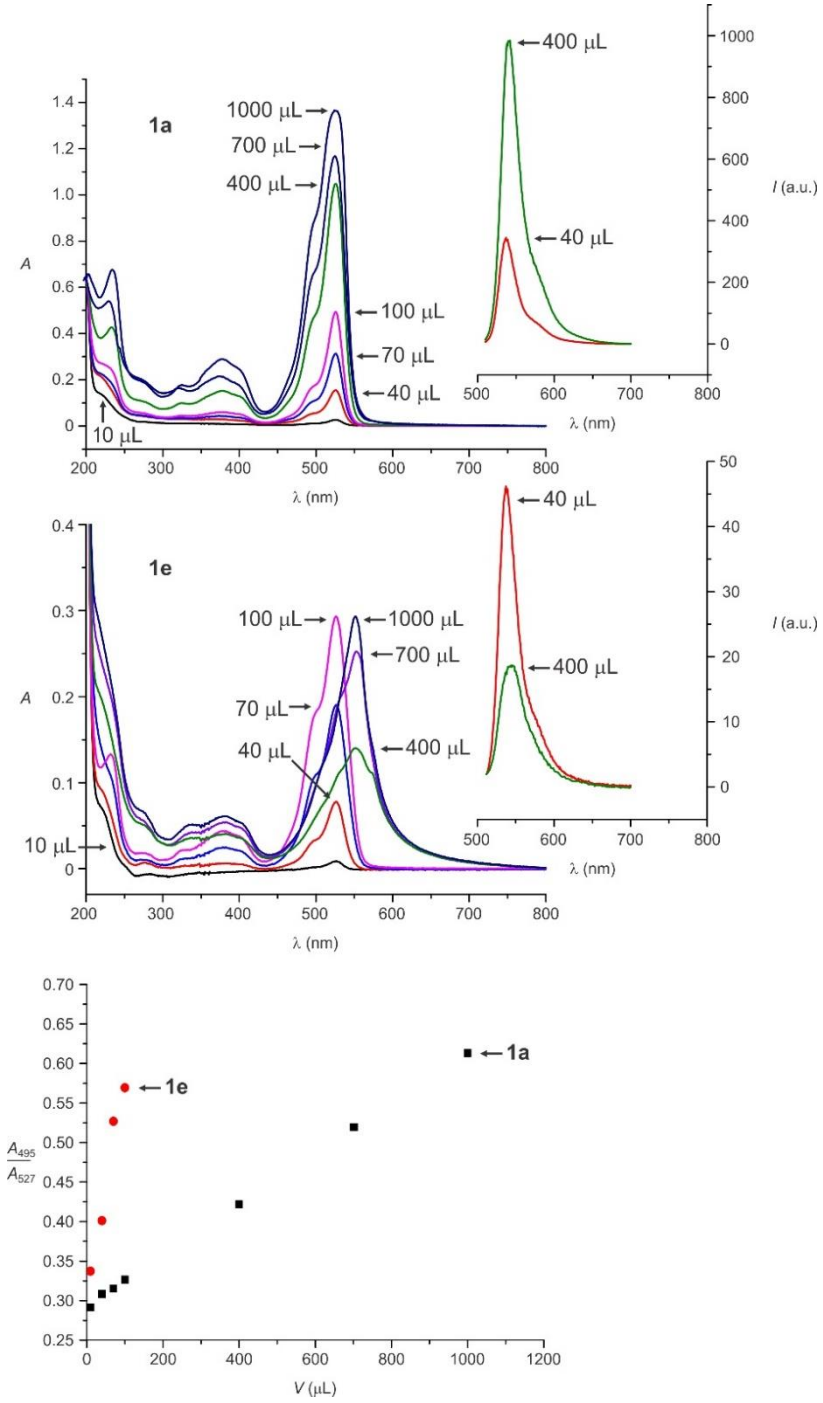

Figure 3.6: Absorption and emission (λ_{Ex} = 500 nm) spectra recorded at 25 °C after combining CH_2Cl_2 solutions of **6** (0.1 mM, volume indicated in the chart) and either **1a** or **1e** (1 mg mL^{-1}, 0.5 mL), distilling the solvent off under reduced pressure, dispersing the residue in PBS (1 mL) and passing the resulting dispersion through a nanoporous membrane. Plots of the ratio (A_{495}/A_{527}) between the absorbance values at 495 and 527 nm in the spectra for **1a** or **1e** against the volume of the initial solution of **6**. A value of 0.30 for A_{495}/A_{527} was measured in EtOH (monomeric BODIPY). Larger ratios indicate an increasing contribution of the dimer.

This conclusion is further supported by the results of time-correlated single photon counting (TCSPC) experiments, which show lifetimes that are highly dependent on guest loading and emission wavelength in the case of **1e**, but not **1a**. Two lifetimes (5.1 and 1.9 ns) were needed to fit the fluorescence decays of **6** incorporated into **1a**. The longest lifetime is identical to the value measured in chloroform (5.1 ns) and its fractional contribution decreases slightly with increasing guest concentration (***a*** in Figure 3.7). The fluorescence decays of **6** encapsulated inside **1e** are significantly different. A third short lifetime (<200 ps) is needed to fit the decays and the fractional contribution of this component increases with guest loading and increasing emission wavelength (***b*** in Figure 3.7 and Table 4.1). The same dependence on guest concentration was observed in experiments with samples prepared independently containing different concentrations of **6**, and with samples prepared using a high concentration of **6** that were subsequently diluted with empty hosts. This result indicates that filled and empty hosts are able to interact and exchange their cargo, thus redistributing the concentrated dye in a larger number of hosts.

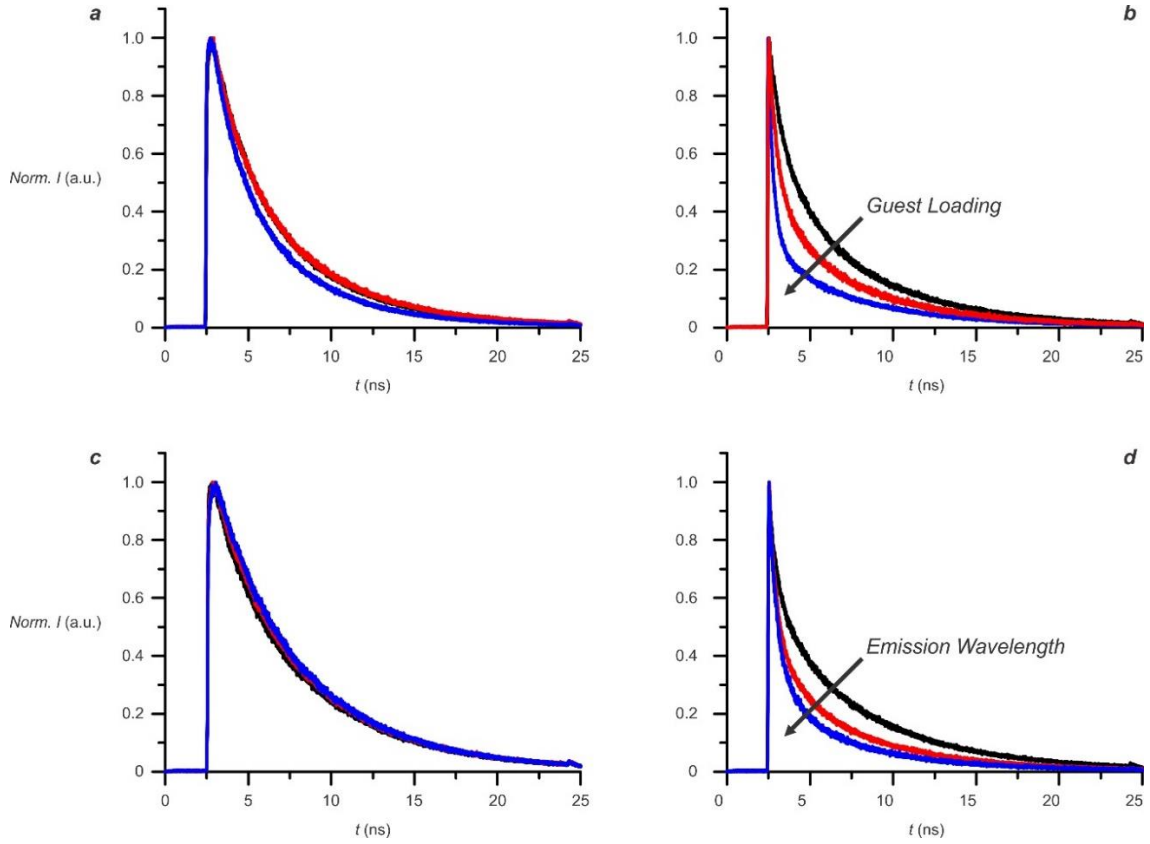

Figure 3.7: Fluorescence intensity decays of **6** encapsulated within nanoparticles of either **1a** (***a*** and ***c***) and **1e** (***b*** and ***d***) dispersed in PBS. Panels ***a*** and ***b*** show the effect of increasing guest loading and panels ***c*** and ***d*** show the effect of increasing emission wavelength. ***a***: λ_{Ex} = 525 nm, λ_{Em} = 555 nm, concentration of **6** = 3.0 (blue), 1.9 (red) or 1.6 μM (black). ***b***: λ_{Ex} = 525 nm, λ_{Em} = 555 nm, concentration of **6** = 2.3 (blue), 1.0 (red) or 0.5 μM (black). ***c***: λ_{Ex} = 500 nm, concentration of **6** = 2.5 μM, λ_{Em} = 570 (blue), 550 (red) or 530 nm (black). ***d***: λ_{Ex} = 500 nm, concentration of **6** = 1.0 μM, λ_{Em} = 570 (blue), 555 (red) or 540 nm (black). Decays were fitted with a sum of exponentials (Table 4.1).

The same wavelength-dependent behavior observed with **6** encapsulated in **1e** was also observed in measurements of **6** dissolved in an ethanol/water (1:10, v/v) mixture (Figure 4.6 and Table 4.1) and was also reported for a similar BODIPY in organic solvent/water mixtures.[47] This trend is consistent with the formation of excimers, which are formed when the hydrophobic chromophore is exposed to water. These interchromophoric interactions occur to a greater extent in **1e** than **1a**, because the

hydrophilic character of the former polymer limits the ability of the supramolecular host to protect the fluorescent guests from the surrounding water molecules.

The difference between the environments that nanoparticles of **1a** and **1e** provide to the encapsulated chromophores is also evident from their response to the presence of quenchers in the surrounding aqueous medium. Specifically, the emission intensity of **6**, entrapped within nanocarriers of **1e** at a guest loading of 1.9% w/w, decreases to 57% (Figure 4.9) after the addition of 4,000 equivalents of NaI, relative to the BODIPY guest, and remains constant for hours. When **1a** is employed in place of **1e**, under otherwise identical conditions, the emission intensity drops to 36% (Figure 4.9), immediately after the addition of the quencher, and decreases further to a stationary value over the course of tens of minutes. The same experiment performed in the absence of macromolecules with a water-soluble analog of **6**, in the shape of **8**,[94] shows a behavior very similar to that observed for **1e**. The emission intensity decreases to 40% (Figure 4.9), but then remains constant for hours. These observations suggest that the hydrophobic character of **1a** slows access of the iodide quenchers to the BODIPY fluorophores, delaying the time required to reach a stationary state, but ultimately enhances quenching efficiency, leading to a pronounced fluorescence decrease. Consistently, Stern–Volmer plots, performed with equilibrated solutions of nanoparticles of **1a**, **1b**, **1d** and **1e**, containing **6** at a guest loading of 1.9% w/w in the presence of increasing amounts of NaI, show linear correlations (Figure 4.10) with a significant dependence of the slope on *m*:*n*. In particular, the Stern–Volmer constant (K_{SV} in Table 3.2) increases from only 8 M^{-1} for the most hydrophilic polymer (*i.e.*, **1e**) to 72 M^{-1} for the most hydrophobic macromolecule (*i.e.*, **1a**).[95]

Fluorescence Correlation Spectroscopy. Fluorescence correlation spectroscopy (FCS) measurements were carried out using nanoparticles of **1a** and **1e**, containing **6** at different fluorophore/polymer ratios. Briefly, FCS is a technique that relies on the measurement of the fluorescence intensity fluctuations of a small number of molecules contained in an optically-restricted volume.[96, 97] The temporal behavior of the measured fluorescence fluctuations are analyzed by means of the autocorrelation function (G(τ)), which contains dynamic information of the different processes that give rise to the measured fluctuations. Brownian motion is the main source of fluorescence fluctuations on the millisecond timescale, under the experimental conditions used in this work.[96] Therefore, the analysis of the measured autocorrelation function yields the diffusion coefficient of the diffusing particles (in this case the guest-filled supramolecular hosts). The autocorrelation function of a solution containing *N* fluorescent species is described by:[96]

$$G(\tau) = \frac{\sum_{i=1}^{N} N_i B_i^2 \left(1 + \frac{4D_i\tau}{{r_0}^2}\right)^{-1}}{(\sum_{i=1}^{N} N_i B_i)^2} \qquad (3.1)$$

where τ is the correlation lag time, r_0 is the radial semiaxis of the Gaussian observation volume, N_i is the average number of molecules of species *i* in the observation volume, B_i is their molecular brightness, and D_i their diffusion coefficient. This equation assumes that the volume is elongated in the axial direction (*i.e.*, fluctuations in the axial direction do not contribute to the autocorrelation function), which is the case of our experimental setup.

For a single species ($N = 1$), the amplitude of the autocorrelation function ($\tau = 0$ in Eq. 3.1) equals the inverse of the average number of particles ($G_0 = \langle N \rangle^{-1}$) present in the observation volume (V), and is related to the average concentration of diffusing

particles (C) as $G_0 = (V N_a C)^{-1}$, where N_a is Avogadro's number. A value of V = 7.4 fL was obtained from the linear relationship between G_0^{-1} and C using 0.1–100 nM solutions of **6** in ethanol (inset in ***a*** of Figure 3.8). If species of different relative brightnesses are simultaneously present in the observation volume (*e.g.*, hosts containing different amounts of guests), G_0 takes the form:

$$G_0 = \frac{\sum_{i=1}^{N} N_i B_i^2}{(\sum_{i=1}^{N} N_i B_i)^2} = \frac{1}{(\sum_i N_i)} \frac{\langle B_i^2 \rangle}{\langle B_i \rangle^2} = \frac{1}{N_T} \frac{\sigma^2 + \mu^2}{\mu^2} \qquad (3.2)$$

Where σ^2 and μ are the variance and mean of the probability density function describing the distribution of brightnesses. Therefore, the inverse of G_0 gives an apparent number of particles that deviates from the true number of particles N_T by the factor $(1 + \sigma^2/\mu^2)^{-1}$.

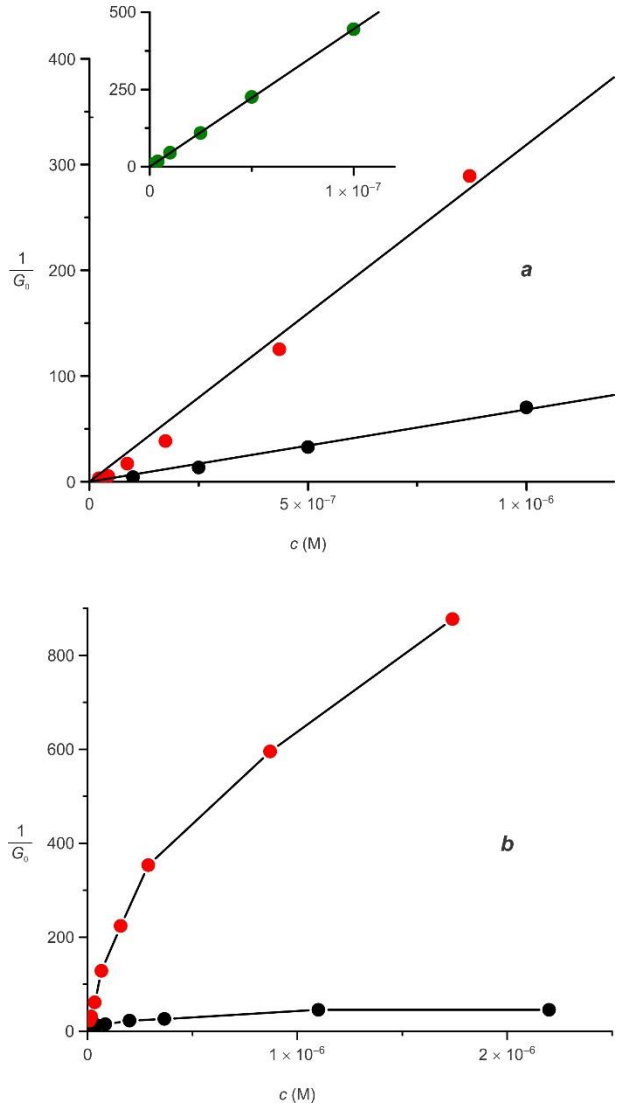

Figure 3.8: Plots of the inverse G_o values, obtained from fitting all autocorrelation decays to Eq. 1, against the concentration of **6**. (***a***) The nanoparticles were prepared with the highest guest concentration and were subsequently diluted with PBS buffer. (***b***) The nanoparticles were prepared with the highest guest concentration and were subsequently diluted with solutions of empty supramolecular hosts. Results for **1a** and **1e** are shown as red and black circles respectively. The inset in panel ***a*** shows data measured for **6** in EtOH. Lines in panel ***a*** are the result of linear regression. Lines in ***b*** are just visual guides.

Measurements with **6** incorporated into nanoparticles of either **1a** or **1e** resulted in FCS amplitudes that appeared to be off by more than one order of magnitude with respect to what was expected for a given concentration of dye (***a*** in Figure 3.8). For example, the FCS amplitude of a 1 μM solution of **6**, encapsulated within nanoparticles of **1a**, was the

same as the amplitude measured with a 71 nM solution of **6** in ethanol. Taking into account that the observation volume measured with solutions of **6** in ethanol was 7.4 fL, and assuming that the distribution of guests follows a Poisson distribution and that the brightness of each nanoparticle is proportional to the number of guests, these results translate into an average number of guests per host of 13. This number is about five times higher than the average number of fluorophores per nanoparticle expected from the N_G values determined as the ratio between the molar concentrations of the molecular guests and the supramolecular host (Table 3.2). This is somewhat expected given that the absorption spectrum and fluorescence intensity decay of these nanoparticles already show signs of some aggregation, so it is likely that the brightness of each particle is not truly proportional to the number of encapsulated guests. The results of experiments with **6** incorporated into nanoparticles of **1e** (***a*** in Figure 3.8) show even greater deviations from the values expected at a given concentration of dye. The ratio of the slopes of the measurements with **1e** and ethanol translates to 63 guests per host, which is implausible in light of the spectroscopic results that suggest that **1e** cannot accommodate fluorescent guests efficiently because of its hydrophilic character. The shape of the fluorescence intensity decay measured with these nanoparticles (***b*** in Figure 3.7) suggests that the distribution of brightnesses is very broad, and that a significant fraction of particles will not be detected during data acquisition because of severe quenching. These two factors contribute to an apparent number of particles that is significantly lower than that measured with **1a** (Eq. 3.2).

All autocorrelation decays could be fitted with one diffusion term (Eq. 3.1), suggesting a narrow distribution of the nanoparticle dimensions consistently with the

DLS measurements. In addition, the position of the autocorrelation function does not change, when the samples are diluted sequentially using aqueous buffer (Figure 4.12). These observations show that the amount of free guests in the aqueous buffer is negligible. Significant amounts of free guests would give rise to a clear second faster component in the autocorrelation function, provided that the partition equilibrium between the nanocarriers core and the aqueous medium is slow compared with diffusion.[98] If the guest exchange is faster than the diffusion of either species, then the two species cannot be resolved by FCS and an average diffusion coefficient is obtained instead. In this case, the mean diffusion time is expected to increase with polymer concentration, as the free guest partitions into the supramolecular hosts.[98] These results are consistent with the very low solubility of **6** in PBS, which was determined to be less than 100 pM (Supporting Information), and with energy-transfer experiments,[87] which suggested that the hydrophobic chromophores do not separate from the amphiphilic polymers to escape into the bulk aqueous solution.

The results of the FCS experiments are significantly different if solutions of filled hosts are diluted with solutions of empty hosts, instead of buffer. In the experiments discussed above, sequential dilutions with buffer do not change the guest/polymer ratio, and because the hydrophobic chromophores are not soluble in the aqueous phase, the average number of molecular guests per supramolecular host does not vary upon dilution. This results in a linear change of the inverse amplitude of the autocorrelation function when the nanoparticles are diluted with PBS buffer (***a*** in Figure 3.8). In this new set of experiments, solutions of guest-filled hosts were diluted with solutions of hosts prepared without guests (empty), in order to decrease the guest/polymer ratio while keeping the

total concentration of polymer constant. As shown in ***b*** of Figure 3.8, the reciprocal of the FCS amplitude (G_0^{-1}) does no longer increase linearly with guest concentration. The fact that diluting with empty hosts leads to markedly different results than diluting with aqueous buffer indicates that hosts containing guests exchange their cargo with empty hosts, which may lead to changes in the mean and variance of the distribution of particle brightnesses. For **1e**, the apparent number of particles in the observation volume does not change when particles containing a total of 2.2 μM BODIPY dye are diluted twofold, in sharp contrast to the factor of two expected because of the increase in the sample volume. A comparison between the TCSPC decays observed at high and low guest concentrations indicates that the distribution of lifetimes shifts to a lower average value and gets broader as the concentration of guest increases. Both effects contribute to the lower apparent number of particles observed at high guest concentrations, as observed experimentally (***b*** in Figure 3.8). The curvature observed with **1a** is not as marked as with **1e**, which is consistent with the results of the spectroscopic experiments that show a lower degree of interchromophoric effects at the same dye concentration.

Conclusions

Amphiphilic macromolecules with a random distribution of decyl and oligo(ethylene glycol) side chains along a common poly(methacrylate) backbone can be prepared from the corresponding hydrophobic and hydrophilic methacrylate monomers under the influence of a radical initiator. The resulting macromolecules readily dissolve in neutral buffer, if the ratio (*m*:*n*) between their hydrophobic and hydrophilic components is lower than 8:1, and assemble spontaneously into particles with nanoscaled dimensions, when *m*:*n* is higher than 1:3. The hydrodynamic diameter (D_H) of the self-

assembling nanoparticles ranges from 6 to 36 nm. Their supramolecular weight (W_S) varies from 16 to 1130 kDa. The average number of macromolecules per nanoparticle (N_M) changes from 2.5 to 59. All three parameters (D_H, W_S and N_M) increase monotonically with *m*:*n*.

Hydrophobic BODIPY chromophores can be encapsulated within the hydrophobic interior of all self-assembling nanoparticles in neutral buffer, if the polymer concentration is greater than a critical value (C_c) ranging from 7.1 to 76.8 μg mL^{-1} with the composition of the macromolecule. Specifically, C_c decreases as *m*:*n* increases. When the average number (N_G) of encapsulated molecular guests per supramolecular host is lower than 0.63, the absorption and emission bands of the entrapped chromophores are identical to those observed in organic solvents and remain unaffected upon storage for days, as long as *m*:*n* is greater than 1:2. At these loading conditions, the fluorescence quantum yield (ϕ_F) increases from 0.39 to 0.78 with *m*:*n* and, for the polymer with the highest relative hydrophobic content, is essentially identical to that measured in THF. As the guest loading increases, interchromophoric interactions lead to significant changes in the shape of the absorption spectrum and a depressive effect on the radiative efficiency of the encapsulated guests. Consistently, the fluorescence of the entrapped chromophores decays multiexponentially with fractional contributions that change with guest loading and emission wavelength. Once again, these effects are also related to *m*:*n*. A decrease in the relative hydrophobic content tends to promote interactions between encapsulated guests and excimer formation can even be observed for the most hydrophilic supramolecular host. Similarly, an increase in the relative hydrophilic content also

facilitates the access of hydrophilic quenchers to the encapsulated guests, which remain relatively shielded in the most hydrophobic supramolecular host instead.

FCS measurements confirm the entrapment of the small fluorescent guests into large supramolecular hosts and do not reveal any free fluorophores diffusing in the bulk aqueous solution. These experiments also show that groups of chromophores are entrapped within the same supramolecular container at high guest loading conditions, and that guests redistribute when mixed with empty hosts.

In summary, our results concur in demonstrating that *m*:*n* is the main structural parameter that ultimately controls the properties of these self-assembling supramolecular hosts. The tendency of the amphiphilic building blocks to form nanoparticles, the physical dimensions of the resulting assemblies and the ability of these supramolecular hosts to encapsulate fluorescent guests, while preserving their photophysical properties and shielding them from the surrounding environment, all increase with the relative hydrophobic content. Indeed, an excess of hydrophobic side chains, relative to their hydrophilic counterparts, is essential to produce optimal supramolecular hosts. When the former components are decyl chains, the latter are oligo(ethylene glycol) tails and the macromolecular backbone is a poly(methacrylate) scaffold, the best choice for *m*:*n* is a value of 6:1 in the shape of polymer **1a**. Thus, this particular structural composition appears to be the ideal one for the further development of our experimental protocols to deliver and operate photoresponsive molecules within live cells and developing embryos.[79-89]

Experimental Procedures

Materials and Methods. Chemicals were purchased from commercial sources and used as received. CH_2Cl_2 and MeCN were distilled over CaH_2. THF was distilled over Na and benzophenone. H_2O (18.2 MΩ-cm) was purified with a Barnstead International NANOpure DIamond Analytical system. Compounds **3**, **4**, **6** and **7** (Figure 4.7) were prepared according to literature procedures.[79, 99, 100] GPC was performed with a Phenomenex Phenogel 5-μm MXM column (7.8 × 300 mm) operated with a Varian ProStar system, coupled to a ProStar 330 photodiode array detector, in THF at a flow rate of 1.0 mL min^{-1}. Monodisperse polystyrene standards (2,700–200,000) were employed to determine the M_n and PDI of the polymers from the GPC traces, following a literature protocol.[101] Matrix-assisted laser-desorption ionization (MALDI) mass spectra were recorded with a Bruker BioFlex IV spectrometer. NMR spectra were recorded with a Bruker Avance 400 spectrometer. DLS measurements were performed with a Malvern ZEN1600 apparatus. The values listed for D_H in Table 3.1 are averaged over ten independent experiments of ten runs of 10 s each. SLS measurements were performed with the same apparatus. The values of W_S listed in Table 3.1 were determined from the concentration dependence of the scattering intensity, following a literature protocol.[101] Absorption spectra were recorded with a Varian Cary 100 Bio spectrometer, using quartz cells with a path length of 1.0 cm. Emission spectra were recorded with a Varian Cary Eclipse spectrometer in aerated solutions. Fluorescence quantum yields were determined with a rhodamine 6G standard, following a literature protocol.[102]

Synthesis of 1a–e. A solution of **3** (**a** = 565 mg, 3 mmol; **b** and **c** = 452 mg, 2 mmol; **d** = 113 mg, 0.5 mmol; **e** = 23 mg, 0.1 mmol; **f** = 11 mg, 0.05 mmol), **4** (1.0 g, 0.5 mmol) and AIBN (**a**, **b** and **d**–**f** = 5 mg, 0.03 mmol; **c** = 0.5 mg, 0.003 mmol) in degassed THF (8

mL) was heated at 75 °C for 3 days in a sealed tube. After cooling down in an ice bath, the solvent was distilled off under reduced pressure. The residue was purified by column chromatography [SiO_2, $CHCl_3$/MeOH (40:1, v/v)] to give the corresponding polymer as a white solid.

1a (1.13 g): GPC: M_n = 19.0 kDa, PDI = 1.28. ^{1}H NMR ($CDCl_3$): δ = 0.84–0.93 (18H, br s), 0.97–1.09 (6H, br s), 1.22–1.39 (54H, br s), 1.69–1.77 (6H, br s), 3.37–3.41 (3H, s), 3.54–3.77 (~180H, m), 3.87–4.02 (7H, br s), 4.06–4.16 (2H, br s).

1b (813 mg): GPC: M_n = 21.0 kDa, PDI = 1.32. ^{1}H NMR ($CDCl_3$): δ = 0.84–0.93 (11H, br s), 0.97–1.09 (3H, br s), 1.22–1.39 (33H, br s), 1.69–1.77 (5H, br s), 3.37–3.41 (3H, s), 3.54–3.77 (~180H, m), 3.87–4.02 (4H, br s), 4.06–4.16 (2H, br s).

1c (613 mg): GPC: M_n = 81.0 kDa, PDI = 1.11. ^{1}H NMR ($CDCl_3$): δ = 0.84–0.93 (11H, br s), 0.97–1.09 (4H, br s), 1.22–1.39 (35H, br s), 1.69–1.77 (8H, br s), 3.37–3.41 (3H, s), 3.54–3.77 (~180H, m), 3.87–4.02 (4H, br s), 4.06–4.16 (2H, br s).

1d (745 mg): GPC: M_n = 21.0 kDa, PDI = 1.16. ^{1}H NMR ($CDCl_3$): δ = 0.84–0.93 (3H, br s), 0.97–1.09 (3H, br s), 1.22–1.39 (9H, br s), 1.69–1.77 (6H, br s), 3.37–3.41 (3H, s), 3.54–3.77 (~180H, m), 3.87–4.02 (1H, br s), 4.06–4.16 (2H, br s).

1e (710 mg): GPC: M_n = 17.0 kDa, PDI = 1.16. ^{1}H NMR ($CDCl_3$): δ = 0.84–0.93 (2H, br s), 0.97–1.09 (3H, br s), 1.22–1.39 (5H, br s), 1.69–1.77 (6H, br s), 3.37–3.41 (3H, s), 3.54–3.77 (~180H, m), 3.87–4.02 (1H, br s), 4.06–4.16 (2H, br s).

1f (548 mg): GPC: M_n = 22.0 kDa, PDI = 1.23. ^{1}H NMR ($CDCl_3$): δ = 0.84–0.93 (1H, br s), 0.97–1.09 (3H, br s), 1.22–1.39 (4H, br s), 1.69–1.77 (5H, br s), 3.37–3.41 (3H, s), 3.54–3.77 (~180H, m), 3.87–4.02 (1H, br s), 4.06–4.16 (2H, br s).

Synthesis of 2a–c. A solution of **3** (**a** = 1.13 g, 5 mmol; **b** = 262 mg, 1 mmol; **c** = 75 mg, 0.3 mmol), **5** (640 mg, 1 mmol) and AIBN (5 mg, 0.03 mmol) in degassed THF (8 mL) was heated at 75 °C for 3 days in a sealed tube. After cooling down in an ice bath, the solvent was distilled off under reduced pressure. The residue was purified by column chromatography [SiO_2, $CHCl_3$/MeOH (40:1, v/v)] to give the corresponding polymer as a colorless oil.

2a (833 mg): GPC: M_n = 23.0 kDa, PDI = 1.14. ^{1}H NMR ($CDCl_3$): δ = 0.84–0.93 (36H, br s), 0.97–1.09 (7H, br s), 1.22–1.39 (115H, br s), 1.69–1.77 (5H, br s), 3.37–3.41 (3H, s), 3.54–3.77 (~52H, m), 3.87–4.02 (15H, br s), 4.06–4.16 (2H, br s).

2b (416 mg): GPC: M_n = 19.0 kDa, PDI = 1.26. ^{1}H NMR ($CDCl_3$): δ = 0.84–0.93 (10H, br s), 0.97–1.09 (3H, br s), 1.22–1.39 (24H, br s), 1.69–1.77 (3H, br s), 3.37–3.41 (3H, s), 3.54–3.77 (~52H, m), 3.87–4.02 (4H, br s), 4.06–4.16 (2H, br s).

2c (368 mg): GPC: M_n = 19.0 kDa, PDI = 1.16. ^{1}H NMR ($CDCl_3$): δ = 0.84–0.93 (4H, br s), 0.97–1.09 (3H, br s), 1.22–1.39 (9H, br s), 1.69–1.77 (2H, br s), 3.37–3.41 (3H, s), 3.54–3.77 (~52H, m), 3.87–4.02 (1H, br s), 4.06–4.16 (2H, br s).

Synthesis of 5. A solution of *N*,*N*'-dicyclohexylcarbodiimide (DCC, 4.6 g, 22 mmol) in CH_2Cl_2 (20 mL) was added dropwise, over the course of 20 min, to a solution of polyethylene glycol (M_n = 0.6 kDa, 12.0 g, 20 mmol), 4-dimethylaminopyridine (DMAP, 2.3 g, 20 mmol), and methacrylic acid (1.8 g, 22 mmol) in CH_2Cl_2 (100 mL) maintained at 0 °C. The reaction mixture was allowed to warm up to ambient temperature and then was stirred for 12 hours under these conditions. The resulting precipitate was filtered off and the solvent of the filtrate was distilled off under reduced pressure. The residue was purified by column chromatography [SiO_2, CH_2Cl_2/MeOH (10:1, v/v) to afford **5** (6.8 g,

53%) as a colorless oil. ESIMS: *m/z* =659 $[M + H]^+$. ^1H NMR ($CDCl_3$): δ = 1.89 (3H, s), 3.39 (3H, s), 3.50–3.72 (~44H, m), 4.25 (2H, s), 5.52 (1H, s), 6.08 (1H, s).

Synthesis of 8. A solution of **7** (106 mg, 0.3 mmol), poly(ethylene glycol) methyl ether (M_n = 2,000, 600 mg, 0.3 mmol), and 4-(*N*,*N*-dimethylamino)pyridine (DMAP, 31 mg, 0.3 mmol) in CH_2Cl_2 (30 mL) was stirred for 10 min at 0 °C. *N*,*N*'-Dicyclohexylcarbodiimide (DCC, 62 mg, 0.3 mmol) was added and the resulting solution was stirred for a further 30 min at 0 °C. The mixture was allowed to warm up to ambient temperature, stirred for 24 hours under these conditions and filtered. The filtrate was concentrated under reduced pressure and the residue was purified by column chromatography [SiO_2, CH_2Cl_2/ MeOH (95:5, v/v)] to give **8** (162 mg, 27%) as a red solid. MALDI: *m/z* = 2404 $[M + H]^+$; ^1H NMR ($CDCl_3$): δ = 8.20 (2H, d, 8 Hz), 7.42 (2H, d, 8 Hz), 4.00–3.51 (176H, m), 3.40 (3H, s), 2.53 (6H, s), 2.32 (4H, q, 8 Hz), 1.28 (6H, s), 1.00 (6H, t, 8 Hz).

Doped Polymer Nanoparticles. CH_2Cl_2 solutions of **6** (0.1 mM, 1–1000 μL) and one of the polymers (2.5 mg mL^{-1}, 0.2 mL or 1 mg mL^{-1}, 0.5 mL) were combined. The solvent was distilled off under reduced pressure, the residue was dispersed in PBS (1 mL) and the mixture was sonicated for 5 min. After storage for 10 min at ambient temperature, the dispersion was passed through a syringe filter with a pore size of 200 nm and the filtrate was used for the imaging and spectroscopic experiments without further purification. The concentration of **6** in the filtrate was estimated from the absorbance at λ_{Ab} (Table 3.2), using the molar absorption coefficient measured for this compound in THF.

TCSPC. Lifetime measurements were performed in a TCSPC setup. The excitation light was a Fianium supercontinuum laser (SC-450-4-PP) operating at 20 MHz equipped

with an Acousto-Optic Tunable Filter (AOTF) to select the excitation wavelength. A polarizer in the excitation pathway was used to excite the sample with vertically-polarized light. Samples were contained in standard 1 cm path length fluorescence cuvettes. The emission polarizer was set at the magic angle (54.7° with respect to the excitation) to eliminate artefacts in the data due to anisotropic properties, such as rotational diffusion. The wavelengths of collected emission were selected by an emission monochromator and the signal was detected with a Hamamatsu MCP-PMT R3809U-50 photomultiplier tube. The TCSPC decay curves were recorded by a Becker and Hickl TCSPC Timing Card (B&H SPC830). All TCSPC decay curves were analyzed using ASUFIT, a MATLAB-based program developed at ASU (http://www.public.asu.edu/~laserweb/asufit) that uses a standard deconvolution procedure and nonlinear regression. The instrument response function (IRF) was measured by scattering excitation light off of a 3% Ludox solution. Typically, the IRF was around 50–80 ps. The fluorescence intensity decay was fit to a sum of exponentials. The goodness of the fit was judged by the χ^2 value and the randomness of the residuals.

FCS. Measurements were carried out using a setup built in-house and described elsewhere.[103, 104] Briefly, the instrument uses a continuous 532 nm Coherent Compass 215M-10 laser, an oil-immersion objective lens (Olympus Apochromat 100x/1.4 NA), avalanche photodiode detectors (Perkin Elmer SPCM AQR-14) and a dedicated hardware correlator card (ALV-5000/EPP Multiple Tau Digital Correlator). The samples were placed in silicone perfusion chambers on a glass coverslip. For every series of FCS measurements, the setup was calibrated with a rhodamine dye of known diffusion coefficient (TAMRA, 420 $\mu m^2\ s^{-1}$).[105, 106] Autocorrelation curves of free TAMRA were

fit with Equation 1 with the known diffusion coefficient fixed in order to determine the radial semi-axis of the observation volume (r_0). The autocorrelation curves obtained with the micelles were then analyzed with the same equation to determine the diffusion coefficient (D).

Acknowledgements. FMR acknowledges support from the National Science Foundation (CHE-1049860). ML acknowledges use of the Ultrafast Laser Spectroscopy Facility at Arizona State University and support from the National Science Foundation (MCB-1157765).

Supporting Information Available. DLS measurements of **1a**–**1f**, **2b** and **2c**; Temporal evolution of D_H for **1a**, **1b** and **1d**–**1f**; temporal evolution of the emission intensity of **6**; absorption and emission spectra of **6**; fluorescence decays and fitting parameters of **6**; synthesis of **8**; absorption and emission spectra of **8**; temporal evolution of the emission intensity of **1a**, **1e** and **8**; Stern–Volmer plot for **1a**, **1b**, **1d**, **1e** and **8**; FCS measurements of **6**. This material is available free of charge via the Internet at http://pubs.acs.org.

Notes. The authors declare no competing financial interest.

CHAPTER FOUR

SUPPORTING INFORMATION

STRUCTURAL IMPLICATIONS ON THE PROPERTIES OF SELF-ASSEMBLING SUPRAMOLECULAR HOSTS FOR FLUORESCENT GUESTS

Sicheng Tang,[†, §] Bryan Donaphon,[‡, §] Marcia Levitus[*,‡] and Françisco M. Raymo[*,†]

Laboratory for Molecular Photonics, Department of Chemistry, University of Miami, 1301 Memorial Drive, Coral Gables, Florida, 33146-0431 and School of Molecular Sciences and The Biodesign Institute, Arizona State University, Tempe, Arizona, 85287-5601

E-Mail: Marcia.Levitus@asu.edu; fraymo@miami.edu

---

† University of Miami

‡ Arizona State University

§ Contributed equally to this work

* Correspondence authors

DLS Measurements of 1a–1f, 2b and 2c, Temporal Evolution of D_H for 1a, 1b and 1d–1f, and Temporal Evolution of the Emission Intensity of 6

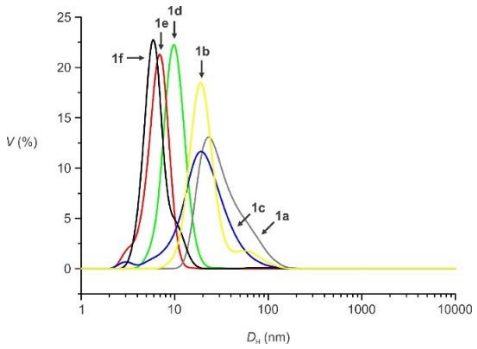

Figure 4.1: Statistical distributions of D_H for **1a–f** (0.5 mg mL^{-1}) determined by DLS in PBS at 22 °C.

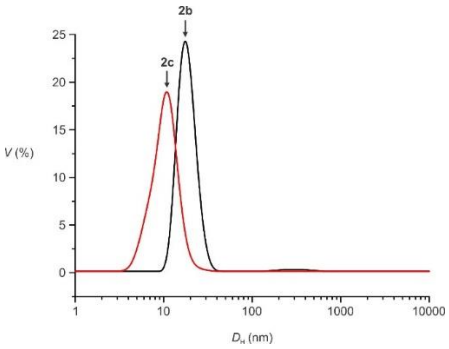

Figure 4.2: Statistical distributions of D_H for **2b** and **2c** (0.5 mg mL^{-1}) determined by DLS in PBS at 22 °C.

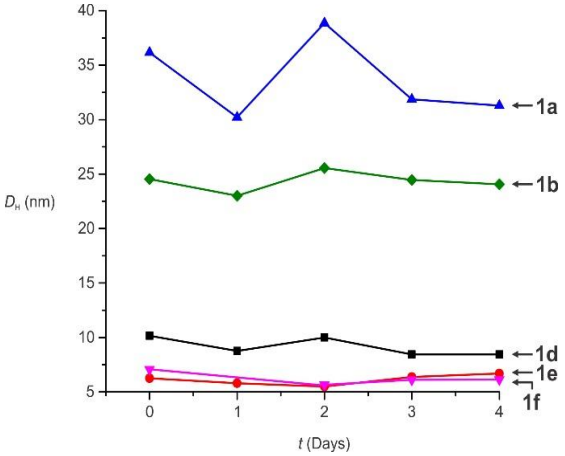

Figure 4.3: Temporal dependence of D_H for **1a**, **1b** and **1d–f** (0.5 mg mL^{-1}) in PBS at 22 °C.

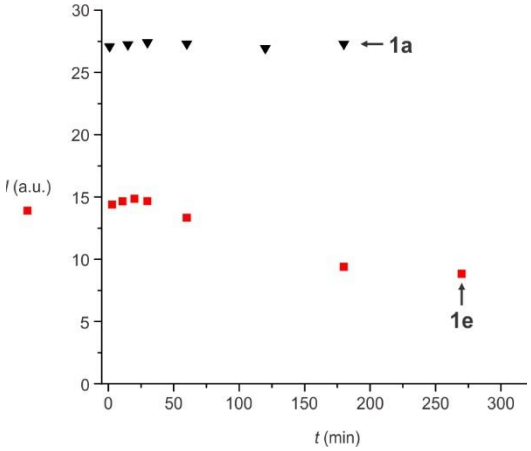

Figure 4.4: Emission intensity (λ_{Ex} = 500 nm, λ_{Em} = 540 nm) of nanoparticles of either **1a** or **1e**, containing **6** (6.6 µM for **1a** and 3.9 µM for **1e**), recorded in PBS at 25 °C.

Absorption and Emission Spectra of 6 and Fluorescence Decays and Fitting Parameters of 6

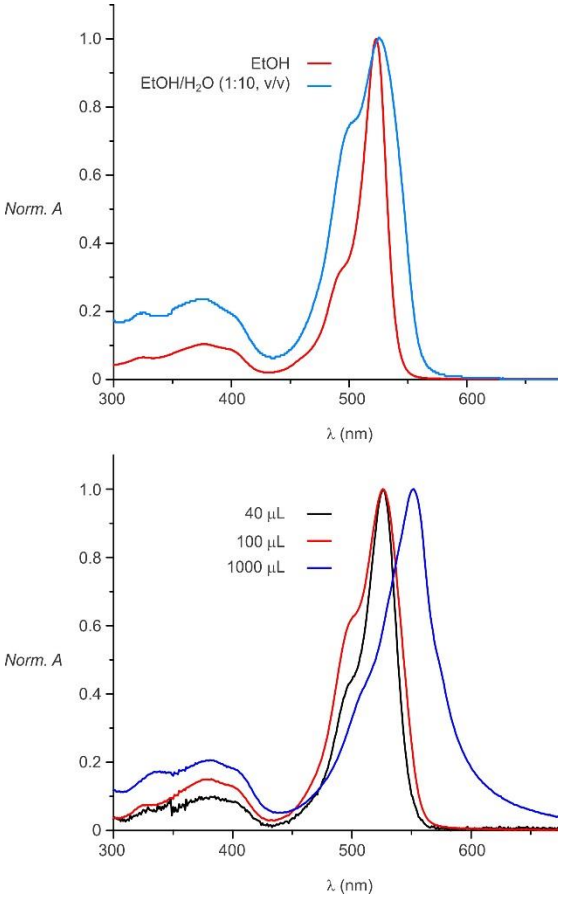

Figure 4.5: Normalized absorption spectra of **6** in EtOH, EtOH/H_2O (1:10, v/v) or after combining CH_2Cl_2 solutions of **6** (0.1 mM, volume indicated in the chart) and **1e** (1 mg mL^{-1}, 0.5 mL), distilling the solvent off under reduced pressure, dispersing the residue in PBS (1 mL) and passing the resulting dispersion through a nanoporous membrane.

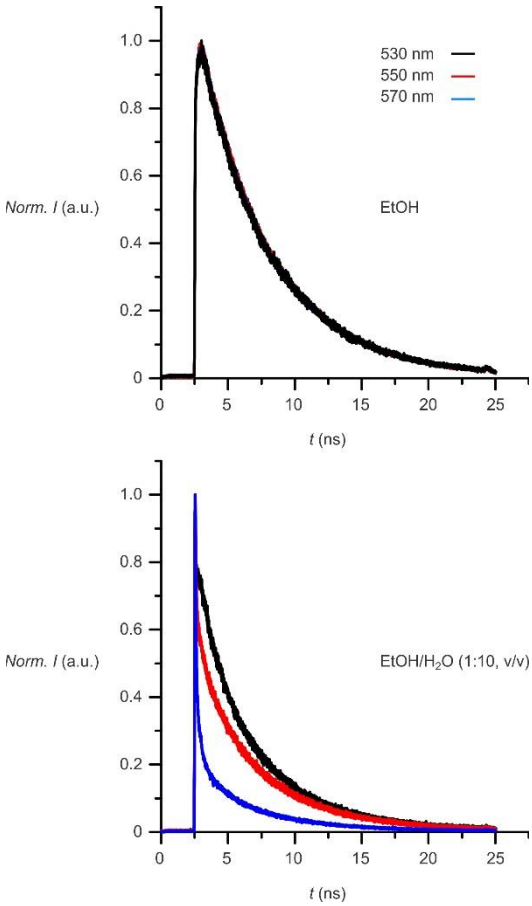

Figure 4.6: Fluorescence intensity decays [λ_{Ex} = 500 nm, λ_{Em} = 570 (blue), 550 (red) or 530 nm (black)] of **6** in EtOH or EtOH/H_2O (1:10, v/v). Decays were fitted with a sum of exponentials (Table 4.1).

Table 4.1: Fitting parameters [a] for the fluorescence decays of 6 [b].

	λ_{Ex} (nm)	λ_{Em} (nm)	τ_1 (ns)	%	τ_2 (ns)	%	τ_3 (ns)	%
1a (2.48 μM)	500	530	5.8	78	1.3	22%	—	—
	500	550	5.8	82	1.8	18%	—	—
	500	570	5.9	77	3.0	23%	—	—
1e (1 μM)	500	540	6.1	34	1.1	19%	0.1	47
	500	555	5.8	22	1.2	22%	0.2	56
	500	570	5.6	16	1.1	25%	0.2	59
1a (1.64 μM)	525	555	5.1	64	1.9	36%	—	—
1a (1.93 μM)	525	555	5.4	63	1.8	37%	—	—
1a (3.04 μM)	525	555	4.7	53	1.7	47%	—	—
1e (0.52 μM)	525	555	5.8	30	1.2	26%	0.08	44
1e (1 μM)	525	555	5.7	24	1.1	24%	0.2	52
1e (2.3μM)	525	555	5.8	14	0.7	17%	0.1	69
EtOH/H_2O (1:10, v/v)	500	530	5.0	14	1.5	7%	0.02	79
	500	550	5.1	19	1.3	7%	0.05	74
	500	570	4.8	6	0.7	6%	0.05	88
	500	530	5.3	100	—	—	—	—
EtOH	500	550	5.3	100	—	—	—	—
	500	570	5.2	100	—	—	—	—

[a] The fluorescence decays (Figures 3.7 and 4.6) were fitted with one, two or three exponential terms, as needed to obtain random residuals.
[b] The concentration of **6** is listed in parentheses for the experiments with **1a** and **1e**.

Synthesis of 8, Absorption and Emission Spectra of 8, and, Temporal Evolution of the Emission Intensity of 1a, 1e and 8

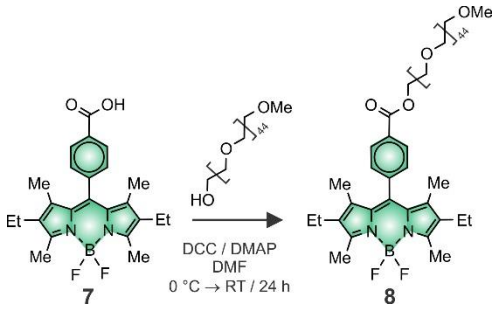

Figure 4.7: Synthesis of **8**.

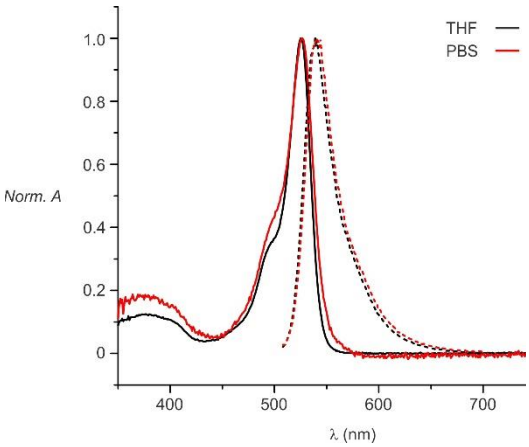

Figure 4.8: Normalized absorption and emission (λ_{Ex} = 500 nm) spectra of **8** in THF or PBS at 25 °C.

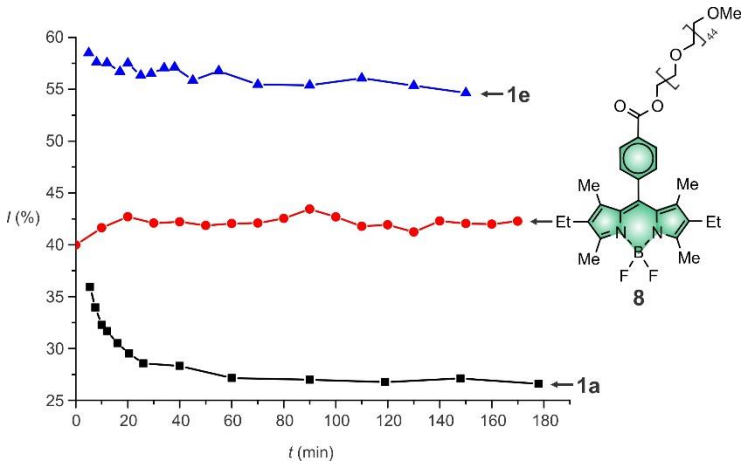

Figure 4.9: Temporal evolution of the emission intensity (λ_{Ex} = 500 nm, λ_{Em} = 540 nm) of nanoparticles of **1a** or **1e**, containing **6** (7.2 μM for **1a** and 2.8 μM for **1e**), recorded in PBS at 25 °C after the addition of NaI (0.1 mM) and reported relative to that measured in the absence of NaI, together with the relative emission intensity of **8** (0.1 mM) recorded after the addition of NaI (0.1 mM) under the same conditions.

Stern–Volmer Plots for 1a, 1b, 1d, 1e and 8

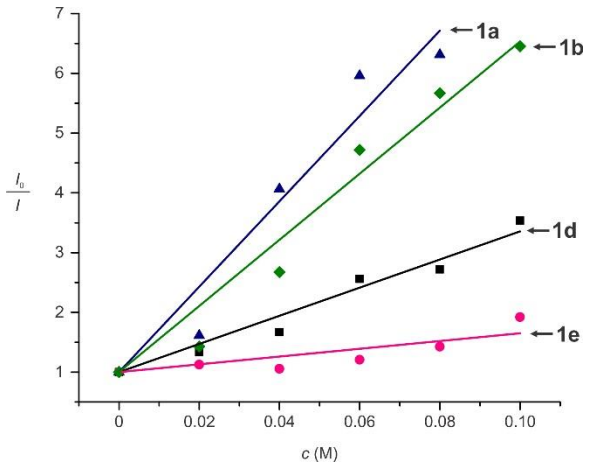

Figure 4.10: Plots of the relative emission intensity (λ_{Ex} = 500 nm, λ_{Em} = 540 nm) of nanoparticles of **1a**, **1b**, **1d** or **1e**, containing **6** (7.2 µM for **1a**, 7.8 µM for **1b**, 2.8 µM for **1d** and 2.8 µM for **1e**), recorded in PBS at 25 °C after the addition of increasing amounts of NaI and storage in the dark for 3 hours, against the iodide concentration.

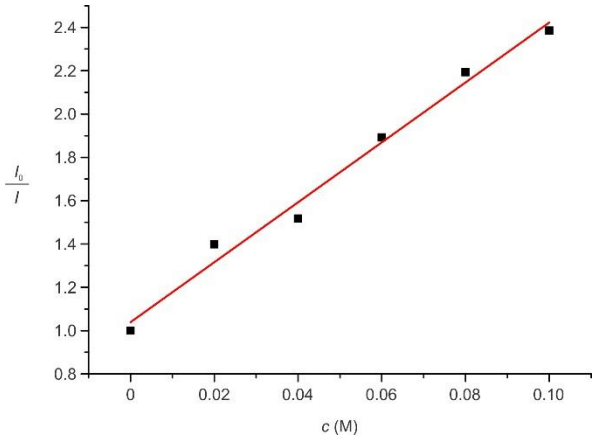

Figure 4.11: Plot of the relative emission intensity (λ_{Ex} = 500 nm, λ_{Em} = 540 nm) of **8** (25 µM), recorded at 25 °C in PBS and the presence of increasing amounts of NaI, against the iodide concentration.

FCS Measurements of 6.

First, EtOH solutions of **6** at different concentrations were prepared and the photon count rate of each solution was measured in the same FCS instrument used to acquire the autocorrelation functions reported in the manuscript. The lowest concentration with a photon count rate three times above the background was 100 pM and, therefore, it was concluded that the limit of detection of compound **6** in our instrument was 100 pM. Then, **6** was dissolved in PBS buffer and the photon count rate was measured in the same instrument. The result was indistinguishable from background, from which we conclude that the solubility of **6** in PBS is less than 100 pM.

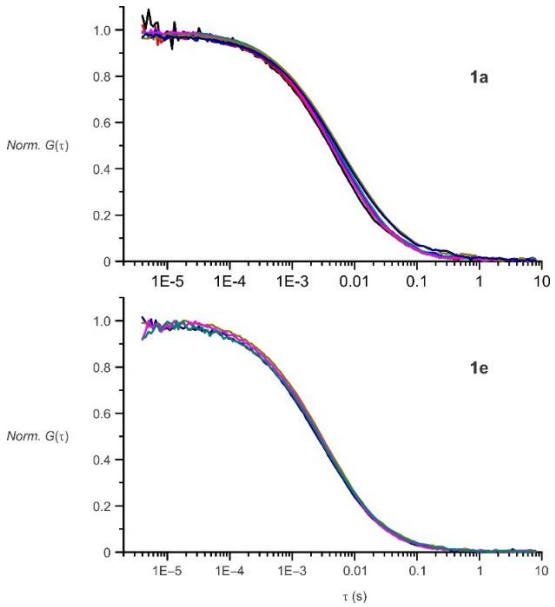

Figure 4.12: Autocorrelation decays of **6** incorporated into nanoparticles of either **1a** or **1e**. Samples were prepared using a concentration of 0.5 mg mL^{-1} for the polymer. The concentration of guest, after filtration, was 2.4 μM for **1a** and 1.0 μM for **1e** The solutions were sequentially diluted using PBS buffer in 6 steps, until the concentration of polymer was 6.25 μg mL^{-1} (1:80) for **1a** and 50 μg mL^{-1} (1:10) for **1e** (the supramolecular hosts are not stable at lower polymer concentrations). Results show negligible changes in the autocorrelation function.

CHAPTER FIVE

INTERCHROMOPHORIC EFFECTS OF TMR AND ALEXA FLUOR DYES ON *E. COLI* DNA PROCESSIVITY CLAMPS

5.1 Motivation and Introduction for the Project

The DNA Processivity Clamps in *E. coli* are referred to as β clamps. The β clamps are loaded onto DNA by another protein called clamp loader. When DNA Polymerase binds to a loaded β clamp, the loaded β clamp ensures that the DNA Polymerase does not diffuse away from the DNA template in the middle of DNA replication.[107] *E. coli* β clamps are homodimeric proteins with an outer diameter of 80 Å and an inner diameter of 35 Å.[108, 109] It should also be noted that the clamp loader only loads β clamps with DNA in the presence of ATP and magnesium and that the clamp loader only opens one of the two interfaces of the β clamp.[110]

Anirban Purohit et al. studied the electrostatic interactions at the dimer interface that holds the β clamp together. FCS measurements of β clamps doubly-labeled at the interfaces revealed microsecond-timescale fluorescence fluctuations. These microsecond-timescale fluorescence fluctuations were absent from FCS measurements with β clamps singly-labeled at the interfaces. Therefore, these fluorescence fluctuations could not be attributed to diffusion. Ideally, the fluorescence fluctuations would report protein dynamics at the interface. However, dynamics within the rhodamine dimer at a static interface could also account for the fluorescence fluctuations. β clamps doubly-labeled away from the interface revealed the same fluorescence fluctuations suggesting that dynamics within the rhodamine dimer were the source of the signal. [34]

Hence, the goal of this project was to study the interchromophoric interactions at the doubly-labeled interfaces of *E. coli* DNA Processivity β clamps. Four rhodamine dyes were investigated: TMR, TMR C6, Alexa Fluor 546, and Alexa Fluor 488. The doubly-labeled interface can be viewed at Figure 5.17. Singly-labeled β clamps and free dye were used as controls. In Figure 5.18, for the singly-labeled β clamps, the distance between two labeling sites (one per interface) is shown to be roughly 65 Å. Therefore, we can expect negligible interchromophoric interactions in the singly-labeled constructs.

At the interface doubly-labeled with identical dyes, two self-quenching mechanisms can be considered: static quenching and dynamic quenching. In static quenching, dimerization occurs in the ground state. These ground-state dimers will be nonfluorescent if the transition dipoles are exactly parallel. Therefore, these dark ground-state dimers will not contribute to the TCSPC decay kinetics. In this scenario of static quenching, only the fluorescence intensity is quenched while the fluorescence lifetime is unaffected. In contrast, the dynamic quenching mechanisms occur in the excited state with a concomitant quenching of both the fluorescence intensity and fluorescence lifetime. In order to determine which quenching mechanisms were present, ensemble absorbance and fluorescence measurements were performed on the doubly-labeled β clamps with singly-labeled β clamps and free dye as controls. Three methodologies were employed to disrupt the doubly-labeled interfaces: 1) the addition of sodium dodecyl sulfate (SDS) detergent to denature the proteins, 2) the addition of clamp loader (γ complex) to open one of the two interfaces, and 3) the use of subunit exchange to decrease the number of dyes per interface. Upon disruption of the doubly-labeled

interfaces, the absorbance and fluorescence measurements were repeated to assess the changes in photophysics.

5.2 Materials and Methods

A. Purification and Fluorescent Labeling of β

At the Department of Biochemistry and Molecular Biology at the University of Florida in Gainesville, FL, Dr. Linda Bloom and her students expressed, purified, and labeled the *E. coli* β clamps. To prevent unwanted labeling, some surface cysteine residues were replaced with serine (Cys-260 and Cys-333). For β clamps singly-labeled at the interfaces, a single cysteine residue was engineered at a specific site, Ile-305 to cysteine or Arg-103 to cysteine (I or R mutations), to allow for site-specific labeling with a maleimide derivative of TMR, TMR C6, Alexa Fluor 546, or Alexa Fluor 488. The maleimide of the reactive dye reacts with the thiol in cysteine. Three dyes came from Molecular Probes/Invitrogen/ThermoFisher Scientific: Tetramethylrhodamine-5-Maleimide, single isomer (Catalog number: T6027), Alexa Fluor 546 C_5 Maleimide (Catalog number: A10258), and 5(6)-Alexa Fluor 488 C_5 Maleimide (Catalog number: A10254). The fourth dye came from AAT Bioquest, Inc.: 5-TAMRA C6 Maleimide (Catalog number: 424). For β clamps doubly-labeled at the interfaces, two cysteine residues were engineered at specific sites, Arg-103 to cysteine and Ile-305 to cysteine. All β clamps were overexpressed in *E. coli* and purified as described previously.[111, 112] Site-directed mutagenesis and fluorescent labeling of β-C260S/C333S/I305C, β-C260S/C333S/R103C and β-C260S/C333S/R103C/I305C were done as described

previously.[113] For the sake of brevity, from this point onward, the serine mutations will be omitted in the designations of the constructs.

Constructs like β-R103C/I305C-$(TMR)_2$ had four TMR dyes per β clamp because there were two doubly-labeled interfaces. Constructs like β-I305C-TMR had two TMR dyes per β clamp because there were two singly-labeled interfaces.

Dye-labeling efficiencies represent the molar ratios of dye to protein. The protein concentrations were determined by a Bradford-type Assay (Bio-Rad) using native unlabeled wild-type β standards that were quantified by performing absorbance measurements at 280 nm under denaturing conditions (to denature the β clamp dimer to monomer).[111] The concentration of TMR was calculated from the absorbance measured at 555 nm using an extinction coefficient of 98 000 M^{-1} cm^{-1}. A similar protocol was followed for the three other dyes. The two samples β-R103C/I305C-$(TMR)_2$ and β-I305C-TMR had dye-labeling efficiencies of 87% and 110% respectively. Dye-labeling efficiencies of 80% and 90% were determined for β-R103C/I305C-$(TMR\ C6)_2$ and β-R103C-TMR C6 respectively. β-R103C/I305C-$(Alexa\ Fluor\ 546)_2$ and β-I305C-Alexa Fluor 546 were labeled with 128% and 114% efficiency. β-R103C/I305C-$(Alexa\ Fluor\ 488)_2$ and β-I305C-Alexa Fluor 488 were labeled with 110% and 81% efficiency.

The TRIS buffer used in the experiments was 20 mM TRIS-HCl (pH 7.5), 50 mM NaCl, 0.5 mM EDTA, 5 mM DTT, 40 μg/mL bovine serum albumin (BSA), and 10% glycerol

B. Subunit Exchange Measurements

For subunit exchange measurements unless otherwise noted, 0.5 μM dye-labeled β was mixed with a twenty-fold excess of unlabeled wild-type β (10 μM). The subunit-exchanged β samples were stored for two days at room temperature in the dark prior to absorbance and fluorescence measurements.

C. Clamp Loader Measurements

The clamp loader (γ complex) was purified as described previously.[114] For the clamp loader measurements, the same TRIS buffer was used with the following additions: 0.5 mM ATP and 80 mM $MgCl_2$. The concentration of γ complex was 2 μM.

D. SDS Measurements

For the SDS measurements, 1% SDS (% wt/v) was used.

E. Ensemble Absorbance Measurements

Ensemble absorbance measurements were performed with the Shimadzu UV-1700 PharmaSpec UV-VIS spectrophotometer. Micro Quartz Cuvettes with path lengths of 1 cm were used.

F. Ensemble Excitation and Emission Scans

Ensemble excitation and emission scans were performed with on a PTI Quantamaster. Micro Quartz Cuvettes with path lengths of 1 cm were used. For the excitation scans of TMR-, TMR C6-, and Alexa Fluor 546-labeled β clamps, unless otherwise noted, the excitation was scanned from 400 nm to 610 nm, and the emission

was collected at 625 nm. For the emission scans of TMR-, TMR C6-, and Alexa Fluor 546-labeled β clamps, unless otherwise noted, the excitation was fixed at 490 nm, and the emission was scanned from 505 nm to 700 nm. For the excitation scans of Alexa Fluor 488-labeled β clamps, unless otherwise noted, the excitation was scanned from 400 nm to 535 nm, and the emission was collected at 540 nm. For the emission scans of Alexa Fluor 488-labeled β clamps, the excitation was fixed at 465 nm, and the emission was scanned from 475 nm to 700 nm. All excitation and emission scans were corrected for variations in the lamp's intensity/power.

G. Ensemble Fluorescence Lifetime Measurements

The Time-Correlated Single Photon Counting (TCSPC) setup used for the fluorescence lifetime measurements was described in full detail elsewhere.[115] Briefly, the samples were excited with vertically polarized light in Micro Quartz Cuvettes with path lengths of 1 cm, and the emission was collected perpendicular to the direction of excitation. The polarizer in front of the emission monochromator was set to the magic angle (54.7° with respect to the excitation). The Instrument Response Function (IRF) was measured by scattering the excitation light off of a 3% Ludox solution. The Full-Width at Half Maximum of the IRF was around 50 ps. The data was analyzed with in-house software (ASUFIT, URL: www.public.asu.edu/~laserweb/asufit/asufit.html). The data was fit with IRF reconvolution and nonlinear regression using a model of discrete exponential decays (Equation 5.1). For the TMR, TMR C6, and AF546-labeled clamps, the excitation was 540 nm, and the emission was collected at 575 nm. For the AF488-labeled β clamps, the excitation was 500 nm, and the emission was collected at 540 nm.

$$I(t) = \sum_{i=1}^{n} A_i e^{-t/\tau_i} \quad (5.1)$$

H. Ensemble Time-Resolved Fluorescence Anisotropy

The ensemble time-resolved fluorescence anisotropy experiments were performed in the same TCSPC setup described in the previous section. Fluorescence intensity decays were collected under the following two polarization conditions: 1) vertical excitation and vertical emission and 2) vertical excitation and horizontal emission. The anisotropy decay was calculated with Equation 5.2.

$$r(t) = \frac{I_{VV}(t) - G \times I_{VH}(t)}{I_{VV}(t) + 2 \times G \times I_{VH}(t)} \quad (5.2)$$

The G factor accounts for the polarization bias of the emission monochromator and was measured with the tail-matching of free fluorescein and free Cy3B.[1, 2] For the time being, the anisotropy decays have not been fit. Instead, the focus will be on the trends of the anisotropy decays.

I. β Clamp Digestion with Proteinase K

The β clamps were digested with a protease called Proteinase K (from *Tritirachium album*, ≥ 800 units/mL, P4850 SIGMA). For the digestion, the β clamps were incubated with 6 µL of Proteinase K for two hours at 60°C in the dark. After the two hour incubation, the β clamp solution was allowed to cool slowly to room temperature. Absorbance and fluorescence measurements were then performed.

5.3 Ensemble Absorbance and Excitation Scans of Dye-Labeled β Clamps

Absorbance scans were performed on β-R103C/I305C-$(TMR)_2$ and β-I305C-TMR before and after clamp loader (γ complex) and sodium dodecyl sulfate (SDS) detergent were added. The two samples β-R103C/I305C-$(TMR)_2$ and β-I305C-TMR had dye-labeling efficiencies of 87% and 110% respectively. As shown in Figure 5.1a, β-R103C/I305C-$(TMR)_2$ had a pronounced blue-shifted peak around 520 nm indicating that H-dimers (sandwich stacks) were present at the doubly labeled interfaces. When clamp loader and SDS detergent were added to β-R103C/I305C-$(TMR)_2$, the peak at 520 nm decreased while the monomeric dye peak at 555 nm grew. The trends of the two peaks indicated that both opening the β clamp interface with clamp loader and denaturing/dissociating the β clamp with SDS detergent disrupted the TMR H-dimers at the interfaces. The actions of the clamp loader did not produce as much monomeric dye as SDS detergent did because the clamp loader only opened one of the two interfaces.[110]

In Figure 5.1b, absorbance measurements of the control β-I305C-TMR did reveal a pronounced short-wavelength shoulder at 520 nm. Absorbance spectra of free TMR maleimide dye (structure in Figure 6.7a) and unreactive 5-TAMRA without and with SDS were measured and shown in Figures 6.1a and 6.1e to determine whether the pronounced shoulder was a spectral characteristic of the dye. The absorbance scans of the free TMR dyes revealed small changes in the absorbance shoulders upon addition of SDS detergent. However, the changes with the free dyes were not as pronounced as they were with β-I305C-TMR. Hence, the pronounced shoulder in β-I305C-TMR could indicate a small degree of aggregated dye due to nonspecific binding of the dye to the β clamp dimer or interactions between the attached dye and nearby amino acid residues. However, since the shoulder at 520 nm only responded to SDS detergent (not γ complex),

the shoulder at 520 nm probably did not correspond to unintended TMR dimers at the interfaces. Therefore, β-I305C-TMR was still considered to be a suitable control.

Absorbance scans of subunit exchanged β-R103C/I305C-$(TMR)_2$ and β-I305C-TMR were also recorded. For β-R103C/I305C-$(TMR)_2$, the trends of the two peaks were consistent with the above case of clamp loader and SDS detergent: in Figure 5.1c, the peak at 520 nm decreased while the peak at 555 nm grew. This consistency indicated that subunit exchange (mixing dye-labeled β with a twenty-fold excess of unlabeled wild-type β) decreased the number of dyes per interface and disrupted the TMR H-dimers at those same interfaces. Similar to the clamp loader, the effects of the subunit exchange were intermediate compared to those of the SDS detergent. Even though a twenty-fold excess of unlabeled wild-type β was used, the exchange kinetics are limited by the long lifetime of the β clamp dimer as monomer association is virtually instantaneous above the dissociation constant K_d. In an earlier study, the K_d of the β clamp dimer was calculated to be 6.5-65 pM.[33] Since all the experiments in this present study were performed with protein concentrations of 0.5 μM or higher, it can safely be assumed that dimer dissociation, not monomer association, was the limiting factor. In that same earlier study, the lifetime of the β clamp dimer at room temperature in 50 mM NaCl buffer was found to be 43 ± 3 hours.[33] Since the subunit exchanged samples had been stored in the dark at room temperature for 48 hours, roughly 33% of the β clamp dimers ($e^{-48/43}$) had not yet dissociated. Therefore, about 33% of the dimers had not yet exchanged their subunits.

For the control β-I305C-TMR in Figure 5.1d, subunit exchange had no impact on the short-wavelength shoulder at 520 nm suggesting that the interaction responsible for the pronounced shoulder was not due to unintentional rhodamine dimers at the interfaces.

Excitation scans were measured of β-R103C/I305C-$(TMR)_2$ and β-I305C-TMR before and after γ complex and SDS detergent were added. In Figure 5.2a, the excitation scans of β-R103C/I305C-$(TMR)_2$ revealed a substantial enhancement of the fluorescence intensity at the peak of 553 nm with SDS. Multiple repeats with SDS indicated that the range of the fluorescence intensity enhancement was around 40 to 60 fold. In contrast, the fluorescence intensity enhancement with γ complex was moderate with multiple repeats indicating a 10-fold enhancement. In Figure 5.2c, for β-R103C/I305C-$(TMR)_2$, the normalized overlaps revealed negligible changes in the shapes of the excitation scans as H dimers were converted to monomers via SDS. This trend made sense because H-dimers should not appear in the excitation as they are non-fluorescent or weakly fluorescent. Since the absorbance spectra of β-R103C/I305C-$(TMR)_2$ revealed ground-state complexes while the fluorescence intensity was severely quenched, these measurements suggested that static quenching occurred at the doubly labeled interfaces.

In Figure 5.2b, excitation scans of β-I305C-TMR revealed a modest fluorescence enhancement (around 1-3 fold) with SDS in contrast to the pronounced (40-60 fold) enhancement observed for β-$(TMR)_2$. In Figure 5.2d, for β-TMR, the normalized overlaps revealed negligible changes in the excitation scan shapes. Excitation scans of free TMR maleimide and unreactive 5-TAMRA before and after SDS were measured and shown in Figures 6.3a and 6.3c where negligible changes in the fluorescence intensity were observed with SDS. In Figures 6.3d and 6.3f, the normalized overlaps indicate negligible changes in the excitation scan shapes with the exception of a bathochromic shift with SDS. In Figure 6.8, the emission scans of β-$(TMR)_2$ and β-TMR revealed the same trends with clamp loader and SDS as were observed with the excitation scans.

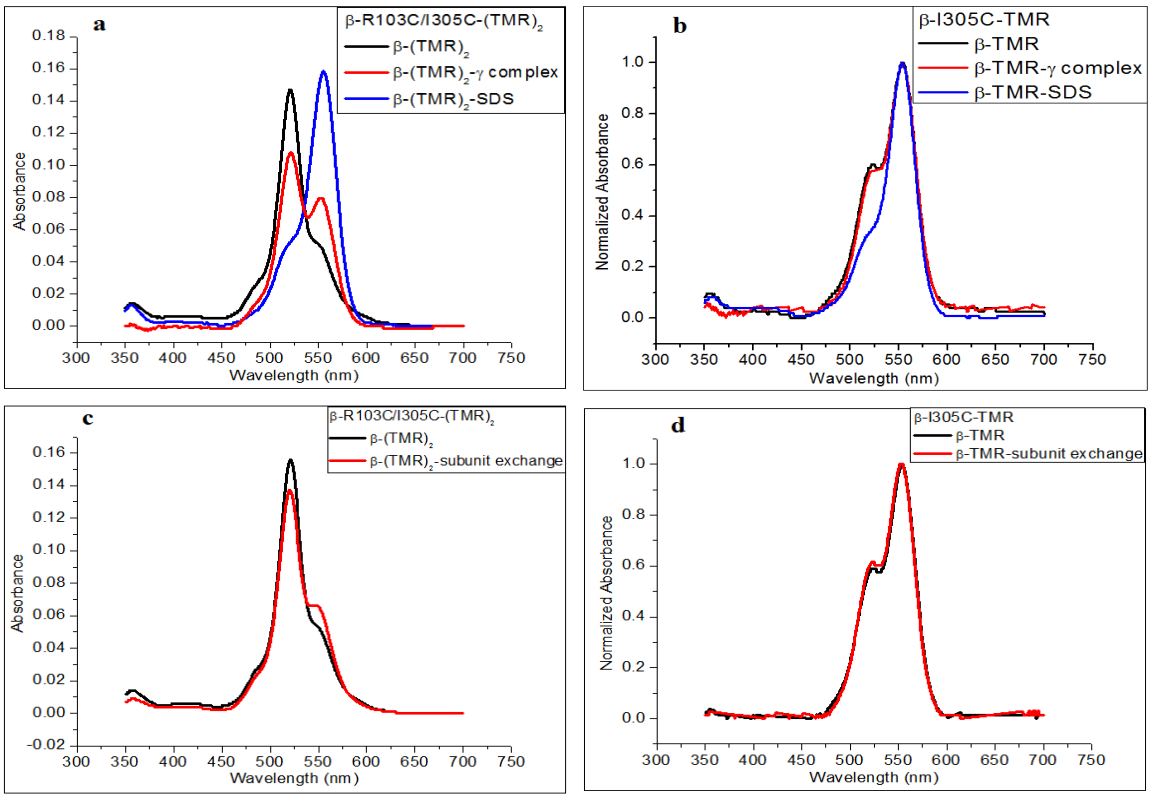

Figure 5.1: Absorbance scans of β-R103C/I305C-$(TMR)_2$ (a and c) and β-I305C-TMR (b and d). All dye-labeled β were 0.5 μM. For subunit exchange, 10 μM unlabeled wild-type β was mixed with 0.5 μM dye-labeled β. The subunit-exchanged samples were stored for two days at room temperature in the dark. Panels (a-b) show the effects of 2 μM γ complex and 1% SDS detergent on the shapes of the absorbance spectra. Panels (c-d) show the effects of subunit exchange on the shapes of the absorbance spectra.

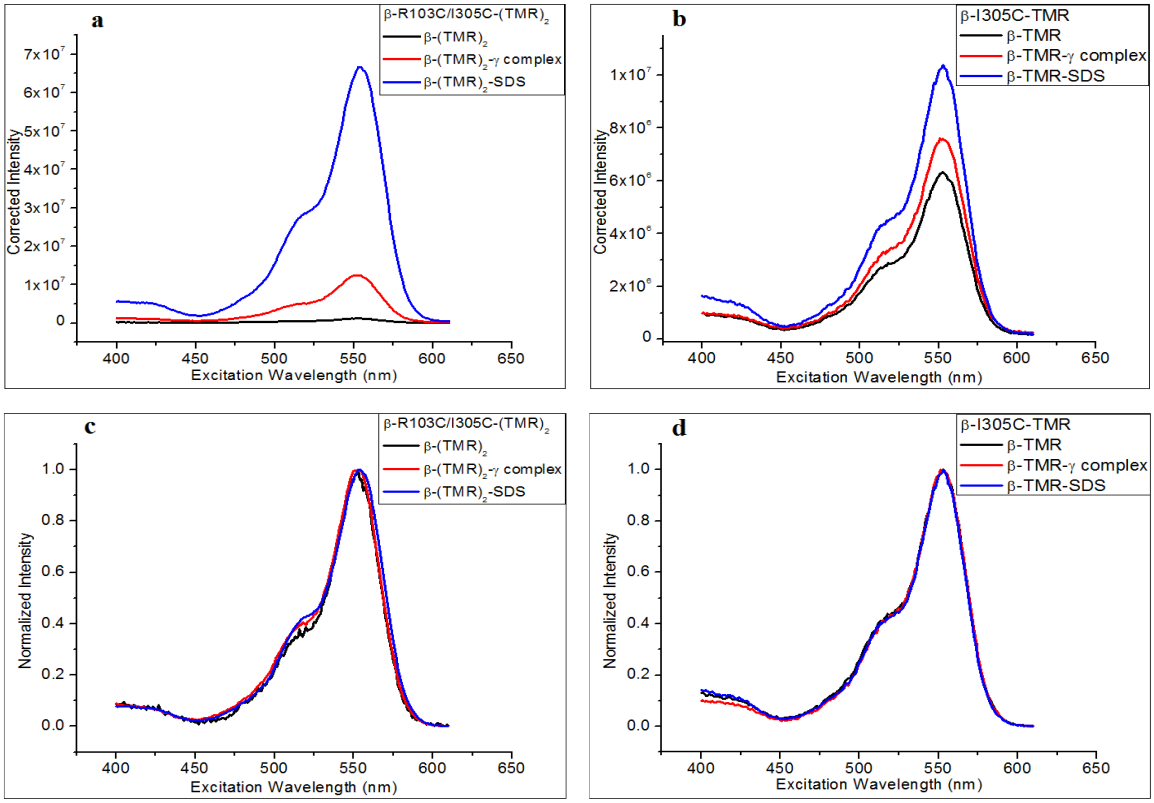

Figure 5.2: Excitation scans of β-R103C/I305C-$(TMR)_2$ (a and c) and β-I305C-TMR (b and d). All dye-labeled β were 0.5 μM. The excitation was scanned from 400 nm to 610 nm, and the emission was collected at 625 nm. Panels (a-b) and panels (c-d) show the effects of 2 μM γ complex and 1% SDS detergent on the intensities and shapes of the excitation spectra.

Absorbance scans were also performed on β-R103C/I305C-$(TMR\ C6)_2$ and β-R103C-TMR C6 which were labeled with a longer TMR linker. The two samples β-R103C/I305C-$(TMR\ C6)_2$ and β-R103C-TMR C6 had dye-labeling efficiencies of 80% and 90% respectively. As shown in Figures 5.3a and 5.3b, the same trends were observed for both the doubly labeled and singly labeled β clamps. For β-R103C/I305C-$(TMR\ C6)_2$, both subunit exchange and the addition of SDS detergent resulted in a diminishing of the peak at 520 nm and concomitant rise in the peak at 555 nm. Clamp loader also had the same impact as shown in Figure 6.9. For the control β-R103C-TMR C6, subunit exchange had no impact on the shoulder at 520 nm (only SDS) ruling out

unintentional rhodamine dimers at the interfaces. Absorbance scans of free TMR C6 maleimide (structure shown in Figure 6.7b) without and with SDS were measured and shown in Figure 6.1c where a drop in the absorbance shoulder with SDS was also observed. Once again, this trend suggested that the pronounced shoulder in β-R103C-TMR C6 could partly be a spectral characteristic of the dye as well as partly nonspecific binding or interactions with nearby amino acids.

Excitation scans of β-R103C/I305C-(TMR C6)$_2$ and β-R103C-TMR C6 were also measured. In Figure 5.4a, for β-R103C/I305C-(TMR C6)$_2$, the excitation scans revealed a substantial fluorescence enhancement (around 20-25 fold) at the peak of 553 nm when SDS interrupted the H-dimers (static quenching). The fluorescence enhancement for the longer linker β-R103C/I305C-(TMR C6)$_2$ was smaller compared to that of the shorter linker β-R103C/I305C-(TMR)$_2$ (40-60 fold). The different enhancements can be explained by the degree of H-dimer formation as shown in the absorbance. If Figure 5.1a is compared with Figure 5.3a, it can be observed that β-R103C/I305C-(TMR)$_2$ had a more substantial peak at 520 nm. Thus, β-(TMR)$_2$ had more H-dimers for SDS to disrupt. Figure 5.4c revealed no changes in the excitation scan shapes of β-(TMR C6)$_2$ with SDS.

In Figures 5.4b and 5.4d, for β-R103C-TMR C6, the excitation scans revealed an enhancement (around 1-2 fold) with SDS, but they did not change shape with SDS. Excitation scans of free TMR C6 maleimide before and after SDS were measured and shown in Figure 6.3b where negligible changes in the intensity were observed with SDS. In Figure 6.3e, the normalized overlaps indicated only a bathochromic shift with SDS. In Figure 6.10, the emission scans of β-(TMR C6)$_2$ and β-TMR C6 revealed the same trends with SDS as were observed with the excitation scans.

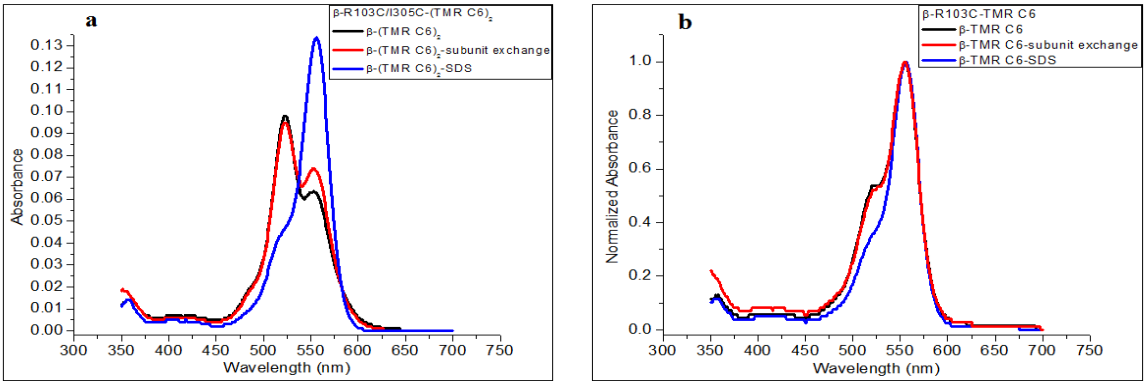

Figure 5.3: Absorbance scans of β-R103C/I305C-(TMR C6)$_2$ (a) and β-R103C-TMR C6 (b). All dye-labeled β were 0.5 µM. Subunit exchange: Unlabeled wild-type β (10 µM) was mixed with 0.5 µM dye-labeled β. The subunit-exchanged samples were stored for two days at room temperature. Panels (a-b) show the effects of subunit exchange and 1% SDS detergent on the shapes of the absorbance spectra.

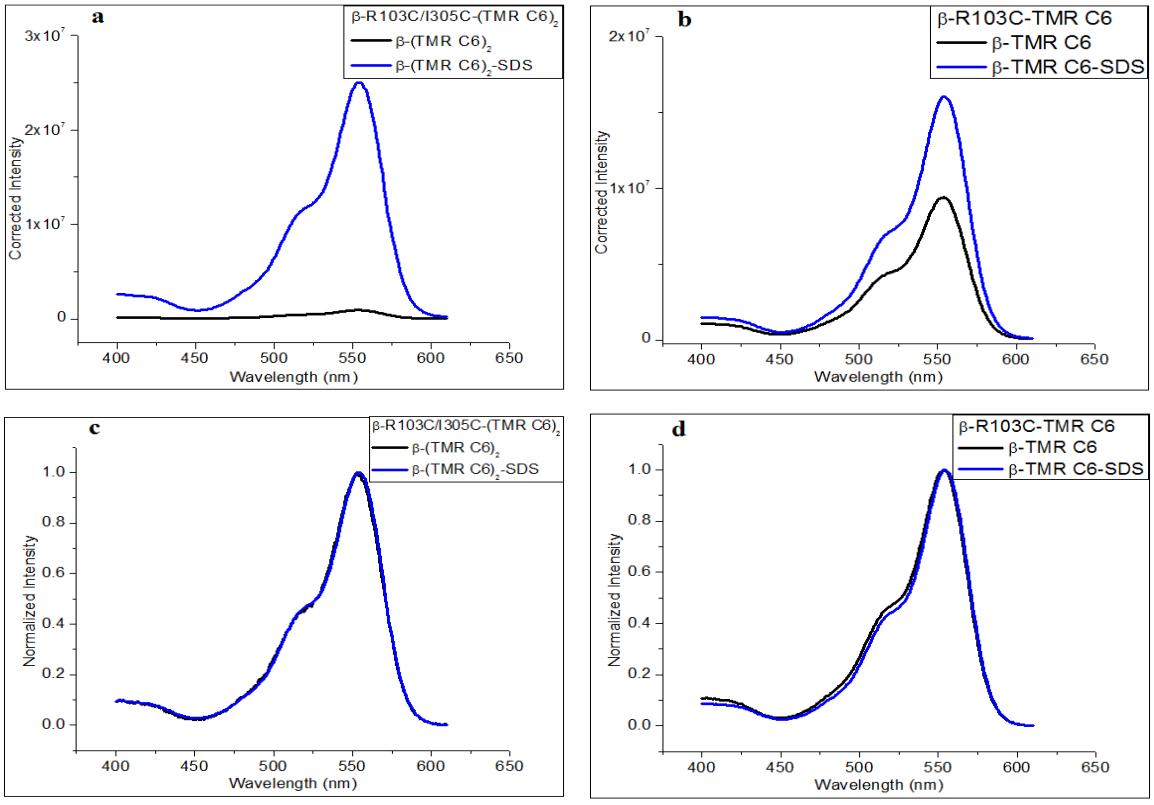

Figure 5.4: Excitation scans of β-R103C/I305C-(TMR C6)$_2$ (a and c) and β-R103C-TMR C6 (b and d). All dye-labeled β were 0.5 µM. The excitation was scanned from 400 nm to 610 nm, and the emission was collected at 625 nm. Panels (a-b) and panels (c-d) show the effects of 1% SDS on the intensities and shapes of the excitation spectra.

Absorbance scans of β-R103C/I305C-(Alexa Fluor 546)$_2$ and β-I305C-Alexa Fluor 546 revealed slightly different trends. The two samples β-R103C/I305C-(Alexa Fluor 546)$_2$ and β-I305C-Alexa Fluor 546 had dye-labeling efficiencies of 128% and 114% respectively. In Figure 5.5a, for β-R103C/I305C-(Alexa Fluor 546)$_2$, a main peak around 556 nm was present, but clear H-dimers were not present. In fact, Alexa Fluor dyes have been advertised as relatively non-interacting because of their sulfonation.

Alexa Fluor dyes have been praised for their bright, photostable conjugates. Protein conjugates of Alexa Fluor dyes have been compared with those of traditional rhodamines and cyanines. The relative fluorescence of the conjugates was higher with Alexa Fluor dyes than it was with the rhodamines and cyanines. Furthermore, as the fluorophore-to-protein molar ratios were increased, the relative fluorescence of the Alexa Fluor protein conjugates plateaued less than that of rhodamines and cyanines. These results suggested that the Alexa Fluor dyes interacted less with each other and were less susceptible to self-quenching.[14] The negatively-charged sulfonate groups improve water solubility, and the charge repulsions among sulfonates minimize dye stacking.

However, in Figure 5.5a, for β-R103C/I305C-(Alexa Fluor 546)$_2$, the short-wavelength shoulder at 525 nm did display peculiar trends that were unexpected. While γ complex did not affect the shoulder, SDS detergent did drop the short-wavelength shoulder. The slightly raised shoulder for β-R103C/I305C-(Alexa Fluor 546)$_2$ could indicate weak aggregation/coupling. Even though Alexa Fluor dyes are famous for not stacking as readily as rhodamines and cyanines, recent evidence has emerged to suggest that even Alexa Fluor dyes can aggregate. Aggregation of Alexa Fluor 610 and Alexa Fluor 633 was reported in a work studying FRET between quantum dot donors and Alexa

Fluor dye acceptors which were conjugated to the quantum dots through peptide linkers. Absorbance scans of the hetero-FRET assemblies revealed H-dimers.[116] The published structure of Alexa Fluor 610-X NHS Ester (Succinimidyl Ester) indicates a sulfonated rhodamine.[117] The structure of Alexa Fluor 633 C_5 maleimide has not been published, but it is suspected of being a sulfonated rhodamine as well.[118] Since Alexa Fluor 546 C_5 maleimide is also a sulfonated rhodamine (Figure 6.7c), it could aggregate too. As further proof, in Figure 5.5e, the absorbance scans of free Alexa Fluor 546 at low micromolar and low millimolar concentrations were overlapped. Figure 5.5e showed that the higher free dye millimolar concentration had a slightly raised short-wavelength shoulder similar to that of β-R103C/I305C-(Alexa Fluor 546)$_2$. This similarity suggested that the slightly raised short-wavelength shoulder of β-R103C/I305C-(Alexa Fluor 546)$_2$ was due to a true interchromophoric interaction at the doubly labeled interface. Figure 5.5c showed that for β-R103C/I305C-(Alexa Fluor 546)$_2$, subunit exchange slightly dropped the short-wavelength shoulder, but SDS detergent dropped the shoulder more completely.

In Figure 5.5b, for the β-I305C-Alexa Fluor 546 control, the absorbance scans did not change shape upon addition of SDS detergent. Figure 5.5d revealed that for β-I305C-Alexa Fluor 546, the short-wavelength shoulder did not drop with subunit exchange or SDS detergent and that β-I305C-Alexa Fluor 546 was a suitable control. Absorbance scans of free Alexa Fluor 546 maleimide without and with SDS were measured and shown in Figure 6.1b where no drop in the absorbance shoulder with SDS was observed.

Excitation scans were performed on β-R103C/I305C-(Alexa Fluor 546)$_2$ and β-I305C-Alexa Fluor 546 before and after γ complex and SDS were added. In Figure 5.6a,

for β-R103C/I305C-(Alexa Fluor 546)$_2$, excitation scans revealed only a modest 2-fold enhancement with γ complex at the peak of 556 nm whereas a higher moderate fluorescence intensity enhancement of around 4-7 fold was observed with SDS detergent. Surprisingly, in contrast to β-R103C/I305C-(TMR)$_2$ and β-R103C/I305C-(TMR C6)$_2$, Figure 5.6c showed that the shoulder of the excitation scan at 525 nm dropped with SDS just as the shoulder of the absorbance scan dropped with SDS in Figures 5.5a and 5.5c. This trend indicated that the interaction or species responsible for the slightly raised shoulder of the absorbance scan was both absorbing and fluorescent. In a study by Gakamsky et al. of singly-labeled β_2-microglobulin with Texas Red (a sulfonated rhodamine), protein oligomerization resulted in dye oligomerization. The excitation scans of β_2m-TR revealed both blue-shifted and red-shifted bands indicating an intermediate geometry between that of H-dimers and J-dimers.[31] Therefore, these interactions in β-R103C/I305C-(Alexa Fluor 546)$_2$ were not H-dimers, but potential intermediate dimers. Since the absorbance spectra revealed an interaction while the fluorescence intensity was slightly quenched, these measurements suggested that static quenching occurred.

In Figure 5.6b, for β-I305C-Alexa Fluor 546, excitation scans revealed negligible changes in the fluorescence intensity upon addition of SDS detergent. The lack of even a modest fluorescence intensity enhancement (as observed with β-I305C-TMR and β-R103C-TMR C6) agreed with the absorbance trends established in Figures 5.5b and 5.5d where SDS had no impact. Figure 5.6d revealed negligible changes in the shapes of the excitation scans of β-I305C-Alexa Fluor 546 with SDS. In contrast to β-I305C-Alexa Fluor 546, excitation scans of free Alexa Fluor 546 maleimide in Figure 6.5a revealed a

2-fold increase in the fluorescence intensity with SDS. In Figure 6.5c, the normalized overlaps indicate only a slight bathochromic shift with SDS.

In Figure 5.6e, an overlap of the excitation scans for both β-R103C/I305C-(Alexa Fluor 546)$_2$ and β-I305C-Alexa Fluor 546 showed that β-R103C/I305C-(Alexa Fluor 546)$_2$ did have a raised shoulder compared to that of β-I305C-Alexa Fluor 546. Addition of SDS dropped the shoulder of β-R103C/I305C-(Alexa Fluor 546)$_2$ to the same level as β-I305C-Alexa Fluor 546.

In Figure 6.11, the emission scans of β-(Alexa Fluor 546)$_2$ and β-Alexa Fluor 546 revealed the same trends with clamp loader and SDS as were observed with the excitation scans.

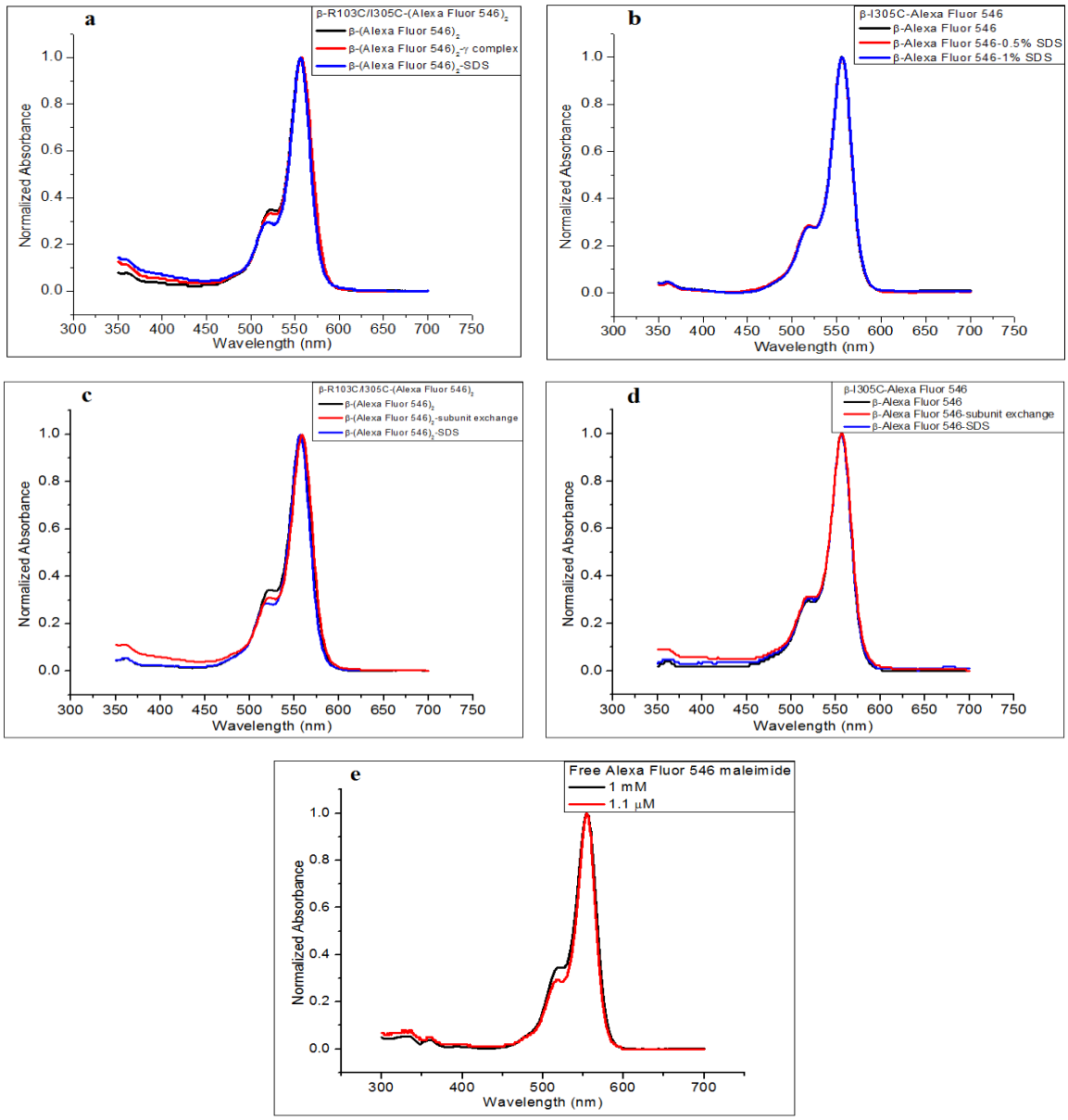

Figure 5.5: Absorbance scans of β-R103C/I305C-(Alexa Fluor 546)$_2$ (a and c), β-I305C-Alexa Fluor 546 (b and d), and free Alexa Fluor 546 (e). All dye-labeled β concentrations were 0.5 μM. For subunit exchange, a twenty-fold excess of unlabeled wild-type β (10 μM) was mixed with 0.5 μM dye-labeled β. The subunit-exchanged samples were stored for two days at room temperature in the dark. Panels (a) and (b) show the effects of 2 μM γ complex and 1% SDS detergent on the shapes of the absorbance spectra. Panels (c) and (d) show the effects of subunit exchange and SDS detergent on the shapes of the absorbance spectra. Panel (e) shows the effects of concentration on the shapes of the absorbance spectra of free Alexa Fluor 546.

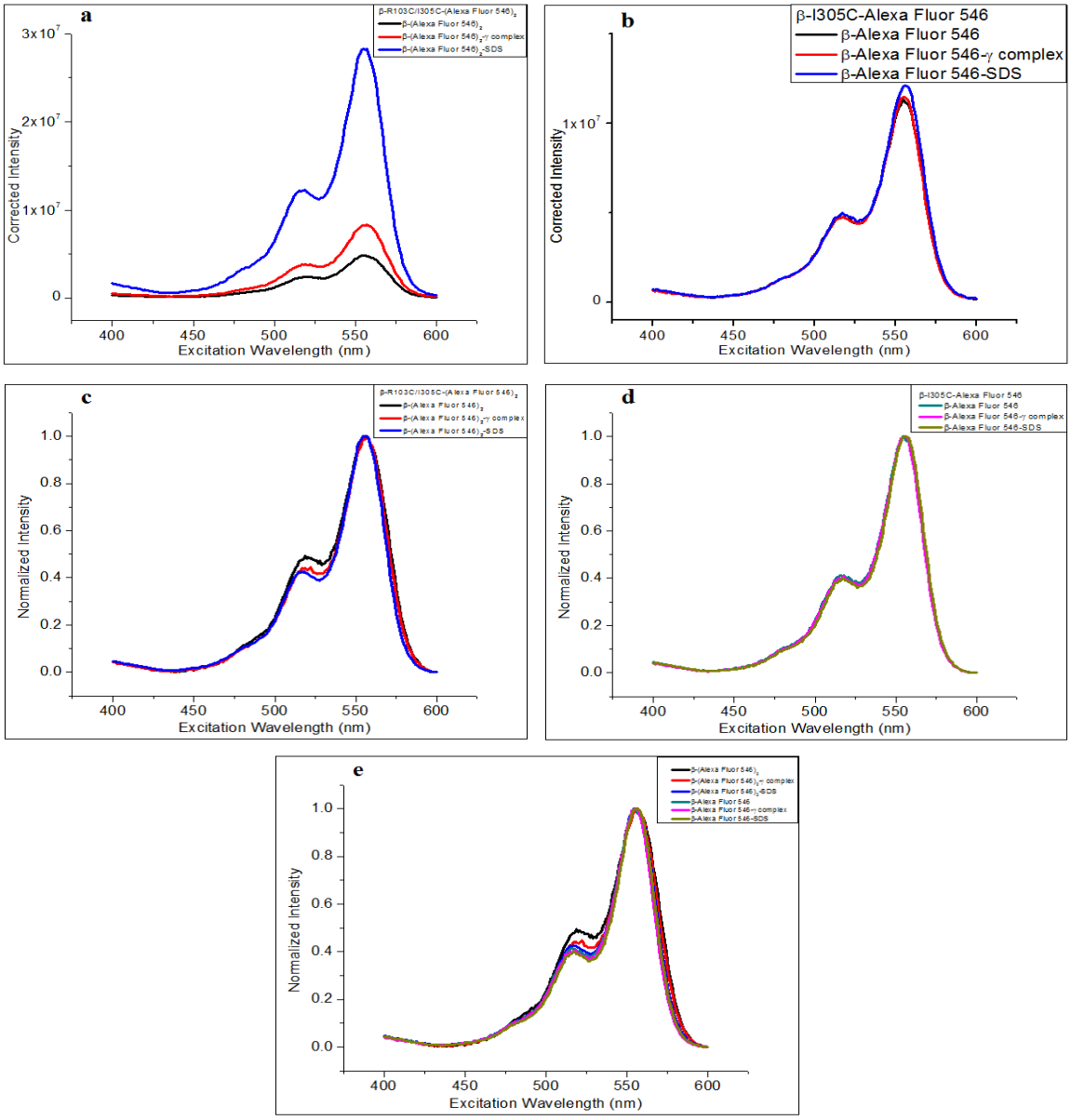

Figure 5.6: Excitation scans of β-R103C/I305C-(Alexa Fluor 546)$_2$ (a and c) and β-I305C-Alexa Fluor 546 (b and d). All dye-labeled β concentrations were 0.5 µM. The excitation was scanned from 400 nm to 600 nm, and the emission was collected at 605 nm. Panels (a) and (b) and panels (c) and (d) show the effects of 2 µM γ complex and 1% SDS detergent on the intensities and shapes of the excitation spectra respectively. Panel (e) shows the overlap of the excitation scans of β-R103C/I305C-(Alexa Fluor 546)$_2$ with those of β-I305C-Alexa Fluor 546.

Absorbance scans of β-R103C/I305C-(Alexa Fluor 488)$_2$ and β-I305C-Alexa Fluor 488 were also recorded. The two samples β-R103C/I305C-(Alexa Fluor 488)$_2$ and

β-I305C-Alexa Fluor 488 had dye-labeling efficiencies of 110% and 81% respectively. In Figure 5.7a, for β-R103C/I305C-(Alexa Fluor 488)$_2$, a main peak around 495 nm was present, but clear H-dimers were not present. Furthermore, the short-wavelength shoulder around 475 nm did not respond to subunit exchange or SDS detergent. The only noticeable effect from SDS was a slight hypsochromic shift. There were no signs of weak aggregation/coupling. In Figure 5.7b, for β-I305C-Alexa Fluor 488, no changes in the shapes or positions of the absorbance spectra were observed upon subunit exchange or the addition of SDS. Absorbance scans of free Alexa Fluor 488 maleimide (structure in Figure 6.7d) without and with SDS were measured and shown in Figure 6.1d where no changes in the shapes of the absorbance scans were observed.

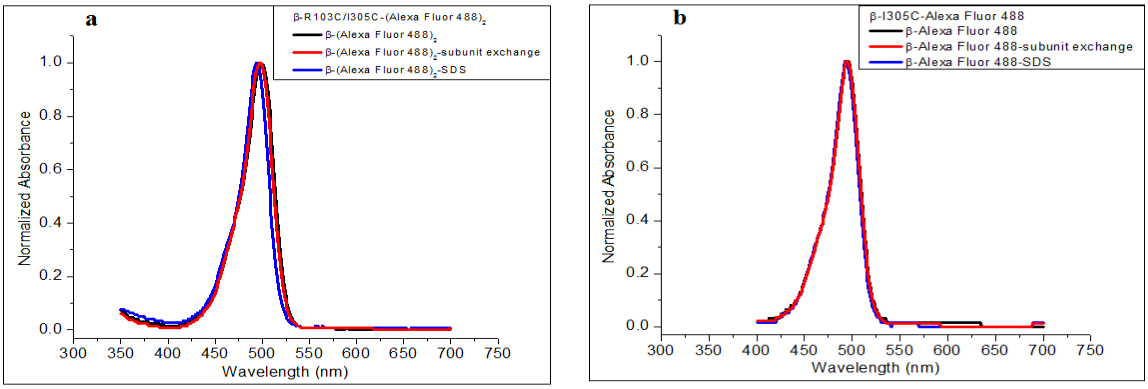

Figure 5.7: Absorbance scans of β-R103C/I305C-(Alexa Fluor 488)$_2$ (a) and β-I305C-Alexa Fluor 488 (b). All dye-labeled β concentrations were 0.5 μM. Subunit exchange: a twenty-fold excess of unlabeled wild-type β (10 μM) was mixed with 0.5 μM dye-labeled β. The subunit-exchanged samples were stored for two days at room temperature in the dark. Panels (a-b) show the effects of subunit exchange and 1% SDS detergent on the shapes of the absorbance spectra.

Excitation scans of β-R103C/I305C-(Alexa Fluor 488)$_2$ and β-I305C-Alexa Fluor 488 were also recorded. In Figure 5.8a, for β-(Alexa Fluor 488)$_2$, excitation scans revealed a moderate fluorescence intensity enhancement of around 6-7 fold at the peak of 492 nm with SDS. In contrast to β-(Alexa Fluor 546)$_2$, Figure 5.8c revealed that SDS did

not change the shapes of the excitation scans of β-(Alexa Fluor 488)$_2$. Since the absorbance spectra of β-(Alexa Fluor 488)$_2$ revealed no ground-state complexes while the intensity was quenched, these measurements suggested that dynamic quenching occurred at the doubly-labeled interfaces in β-(Alexa Fluor 488)$_2$. Figures 5.8b and 5.8d displayed negligible changes in the intensities at the peak of 492 nm and in the shapes of the excitation scans with SDS for β-Alexa Fluor 488. Figures 6.5b and 6.5d revealed no changes in the intensity and shapes of the excitation scans with SDS for free Alexa Fluor 488 maleimide. In Figure 6.12, the emission scans of β-(Alexa Fluor 488)$_2$ and β-Alexa Fluor 488 revealed the same trends with SDS as were observed with the excitation scans.

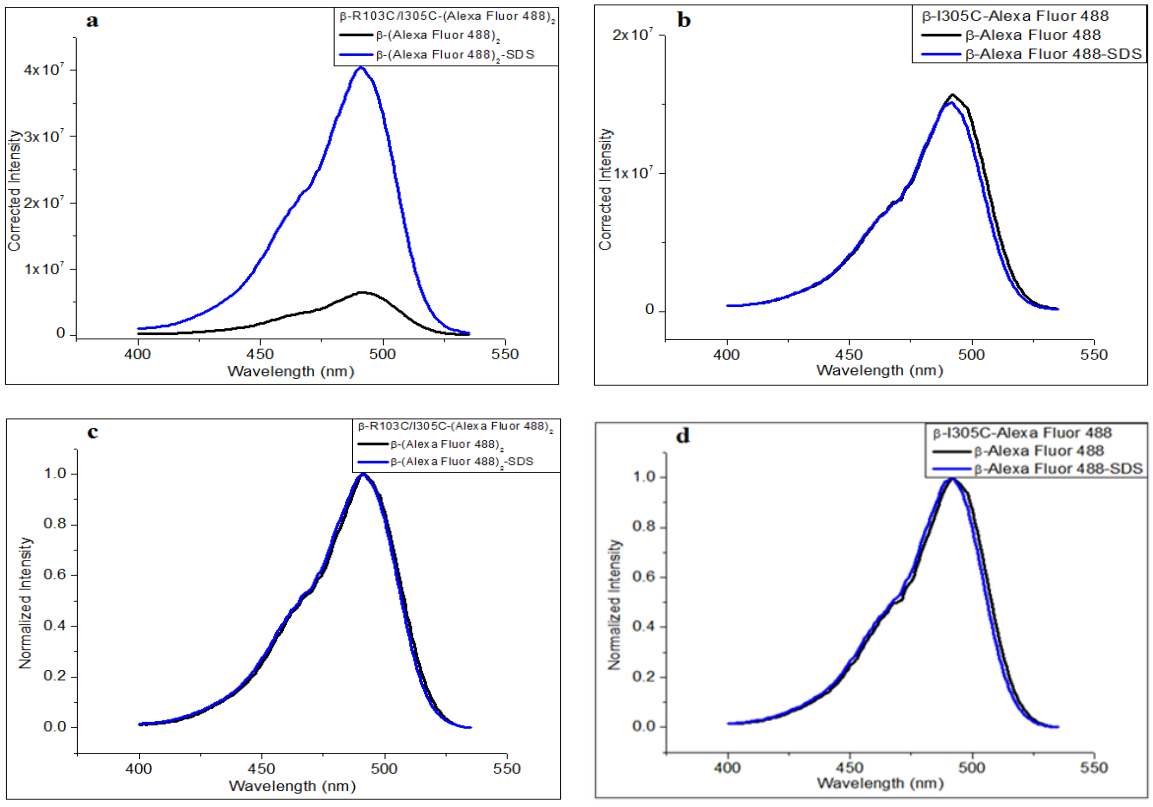

Figure 5.8: Excitation scans of β-R103C/I305C-(Alexa Fluor 488)$_2$ (a and c) and β-I305C-Alexa Fluor 488 (b and d). All dye-labeled β were 0.5 μM. The excitation was scanned from 400 nm to 535 nm, and the emission was collected at 540 nm. Panels (a-b) and (c-d) show the effects of 1% SDS on the intensity and shape of the excitation spectra.

5.4 Ensemble TCSPC and Time-Resolved Anisotropy of Dye-Labeled β Clamps

For β-R103C/I305C-$(TMR)_2$ and β-I305C-TMR, TCSPC decays were collected before and after γ complex and SDS were added and before and after subunit exchange was carried out. The TCSPC fitting parameters are reported in Table 6.1. As shown in Figures 5.9a and 5.9c, the TCSPC decay of β-R103C/I305C-$(TMR)_2$ was initially quenched with three fluorescence lifetimes recovered from the fitting (τ_1 = 2.9 ns (42%), τ_2 = 1.2 ns (28%), and τ_3 = 0.1 ns (30%)). Three exponentials were required in the fitting to obtain random residuals. The average fluorescence lifetime of β-R103C/I305C-$(TMR)_2$ was 1.6 ns.

The first lifetime (τ_1 = 2.9 ns) was assumed to be associated with incompletely labeled interfaces because the labelling efficiency is never a perfect 100%. Therefore, some interfaces might have been singly-labeled instead of doubly-labeled. The second lifetime (τ_2 = 1.2 ns) was attributed to the protein environment of the dye because the second lifetime was also present in the control β-I305C-TMR. The third lifetime (τ_3 = 0.1 ns) was associated with interchromophoric interactions. The geometries of the rhodamine dimers at the doubly-labeled interfaces possibly deviated from exactly parallel transition dipoles (deviation from H-dimer geometry). Therefore, these rhodamine dimers were weakly fluorescent rather than truly non-fluorescent.

In Figures 5.9a and 5.9c, for β-R103C/I305C-$(TMR)_2$, when γ complex was added or when subunit exchange was carried out, the decay kinetics moderately lengthened with an average fluorescence lifetime of 2.2 ns. The intermediate effects of γ complex and subunit exchange in the TCSPC measurements mirrored the intermediate effects of γ complex and subunit exchange in the absorbance scan and excitation scan measurements.

However, when SDS detergent was added to denature and dissociate the β clamps, the H-dimers were disrupted resulting in a longer lifetime of 3.4 ns. As shown in Figure 5.9e, the free TMR maleimide had a monoexponential decay with a lifetime of 2.3 ns. When SDS was added to the free TMR, a longer lifetime of 3.3 ns was also recovered. While the longer lifetime with SDS might be an artifact, the substantial fluorescence enhancement of β-R103C/I305C-$(TMR)_2$ with SDS from Figure 5.2a indicated that H-dimers were truly disrupted. Furthermore, when β-R103C/I305C-$(TMR)_2$ was digested with a protease called Proteinase K, a longer lifetime of 2.6 ns was obtained as shown in Figure 5.9f. Since Proteinase K, unlike SDS, does not enhance the brightness of TMR dyes, the presence of the longer lifetime suggested that disruption of the doubly-labeled interfaces resulted in dissociation of the H-dimers. In Figure 6.13, absorbance and excitation/emission scans of β-R103C/I305C-$(TMR)_2$ with Proteinase K indicated that H-dimers were disrupted with concomitant growth of the monomer absorption peak around 551 nm and pronounced fluorescence intensity enhancements of around 50-60 fold.

In Figures 5.9b and 5.9d, the TCSPC decays of β-I305C-TMR could be fit with two lifetimes (τ_1 = 2.7 ns (81%) and τ_2 = 0.6 ns (19%)). The presence of a second lifetime close to 1 ns in β-I305C-TMR strongly suggested that the second lifetime was characteristic of the protein environment. The addition of γ complex and the actions of subunit exchange had no impact on the TCSPC decay kinetics in agreement with the absorbance trends in Figures 5.1b and 5.1d and the excitation trends in Figure 5.2b. However, the addition of SDS detergent to β-I305C-TMR in Figure 5.9b resulted in a longer lifetime of 3.4 ns in agreement with the absorbance trends from Figure 5.1b and the excitation trends from Figure 5.2b.

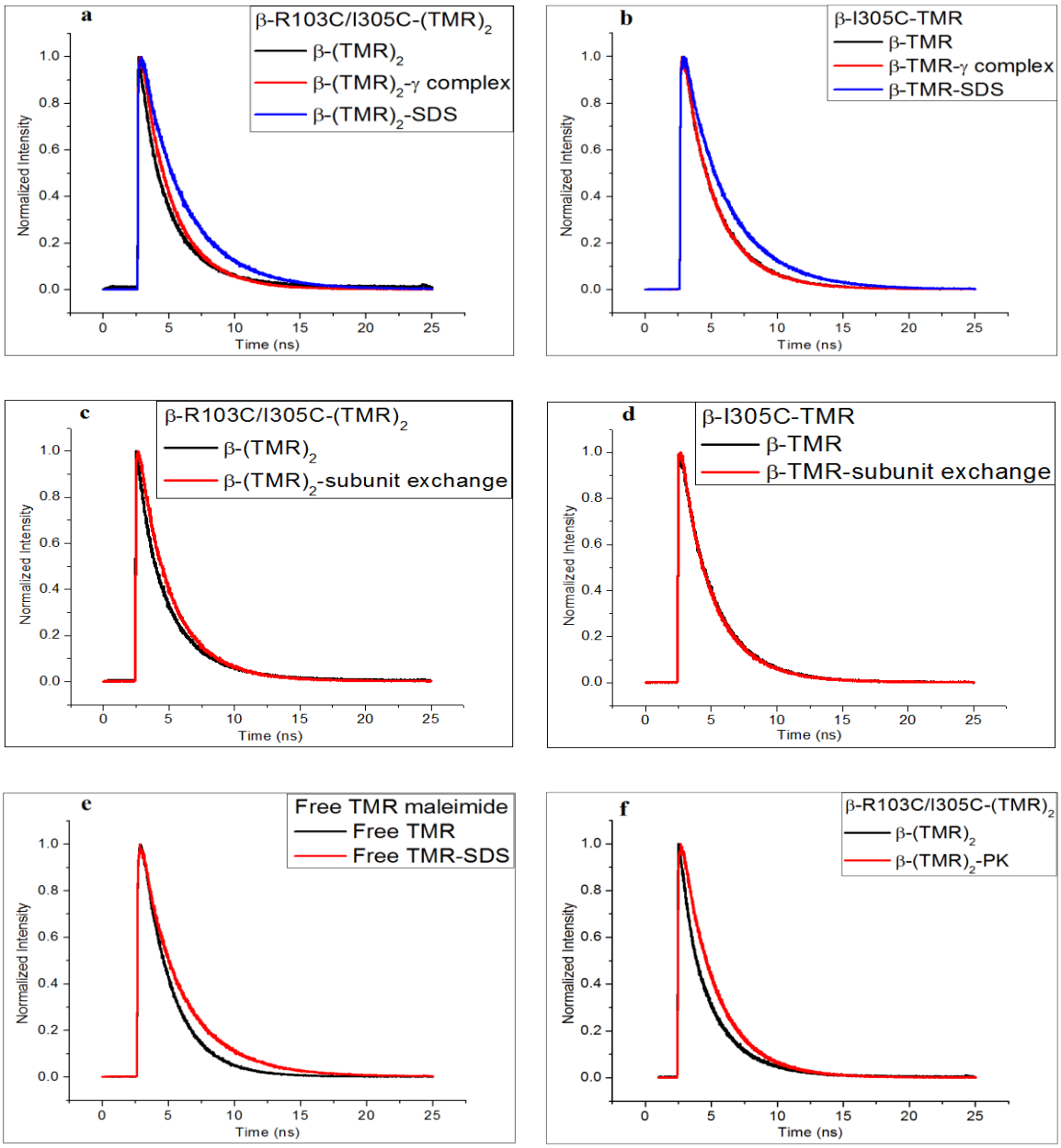

Figure 5.9: TCSPC decays of β-R103C/I305C-$(TMR)_2$ (a, c, and f), β-I305C-TMR (b and d), and free TMR maleimide (e). All dye-labeled β concentrations were 0.5 µM. For subunit exchange, a twenty-fold excess of unlabeled wild-type β (10 µM) was mixed with 0.5 µM dye-labeled β. The subunit-exchanged samples were stored for two days at room temperature in the dark. The excitation wavelength was 540 nm while the wavelength of collected emission was 575 nm. Panels (a) and (b) show the effects of 2 µM γ complex and 1% SDS on the TCSPC decays. Panels (c) and (d) show the effects of subunit exchange on the TCSPC decays. Panel (e) shows the effects of 1% SDS on the TCSPC decay of 1 µM free TMR maleimide in water. Panel (f) shows the effects of Proteinase K on the TCSPC decay of β-R103C/I305C-$(TMR)_2$.

As shown in Figures 5.10a through 5.10e, the TMR C6-labeled β clamps and free TMR C6 maleimide displayed similar TCSPC trends with γ complex, SDS, and subunit exchange. The TCSPC fitting parameters are reported in Table 6.2. For β-R103C/I305C-(TMR C6)$_2$, the TCSPC decay was initially quenched with three fluorescence lifetimes (τ_1 = 2.7 ns (24%), τ_2 = 0.8 ns (23%), and τ_3 = 0.1 ns (53%)). The average fluorescence lifetime of β-R103C/I305C-(TMR C6)$_2$ was 0.9 ns. The labeling efficiency of β-R103C/I305C-(TMR C6)$_2$ was 80%, and the amplitude of τ_1 was 24% suggesting that incompletely labeled interfaces alone were responsible for τ_1. In Figures 5.10a and 5.10c, when γ complex was added or when subunit exchange was carried out, the TCSPC decay kinetics of β-R103C/I305C-(TMR C6)$_2$ moderately lengthened with an average fluorescence lifetime of 2.0 ns. However, when SDS was added to β-R103C/I305C-(TMR C6)$_2$, a longer lifetime of 3.4 ns was recovered. In Figure 5.10e, the TCSPC decay of free TMR C6 maleimide was a monoexponential decay with a lifetime of 2.4 ns. Upon addition of SDS to the free dye, a longer lifetime of 3.4 ns was also recovered. While the longer lifetime with SDS might be an artifact, the pronounced fluorescence enhancement of β-R103C/I305C-(TMR C6)$_2$ with SDS from Figure 5.4a indicated that H-dimers were truly disrupted.

In Figure 5.10d, the TCSPC decay of β-R103C-TMR C6 could be fit with two lifetimes (τ_1 = 3.0 ns (82%) and τ_2 = 0.6 ns (18%)). As previously mentioned, the second lifetime was probably characteristic of the protein environment. When subunit exchange was carried out, the TCSPC decay kinetics did not change in agreement with the absorbance trends from Figure 5.3b. When SDS was added, the TCSPC decay kinetics negligibly changed.

In Figure 5.10f, an overlap of β-R103C/I305C-$(TMR)_2$ with β-R103C/I305C-$(TMR\ C6)_2$ revealed that the longer linker had a more quenched TCSPC decay than the shorter linker despite the fact that the absorbance scans and excitation scans indicated that the shorter linker had a larger extent of H-dimer formation. The only way to explain this apparent contradiction is that the H-dimers in the shorter linker β-R103C/I305C-$(TMR)_2$ were so strongly quenched that the only detected fluorescence came from incompletely labeled interfaces. Hence, the shorter linker β-R103C/I305C-$(TMR)_2$ displayed static quenching where the fluorescence intensity was quenched but the fluorescence lifetime was not quenched because the dark ground-state complexes did not participate in the TCSPC decay kinetics. However, the quenching was not entirely static because the lifetime was not entirely unaffected (the TCSPC decays of β-R103C/I305C-$(TMR)_2$ had a third short lifetime component τ_3). Therefore, for β-R103C/I305C-$(TMR)_2$, the quenching was a combination of static and dynamic but with a larger degree of static quenching. In contrast, the longer linker β-R103C/I305C-$(TMR\ C6)_2$ displayed dynamic quenching where both the fluorescence intensity and fluorescence lifetime were quenched. However, since H-dimers (static quenching) were also detected in the absorbance scans of β-R103C/I305C-$(TMR\ C6)_2$, the quenching could be described as a combination of static and dynamic but with a larger degree of dynamic quenching.

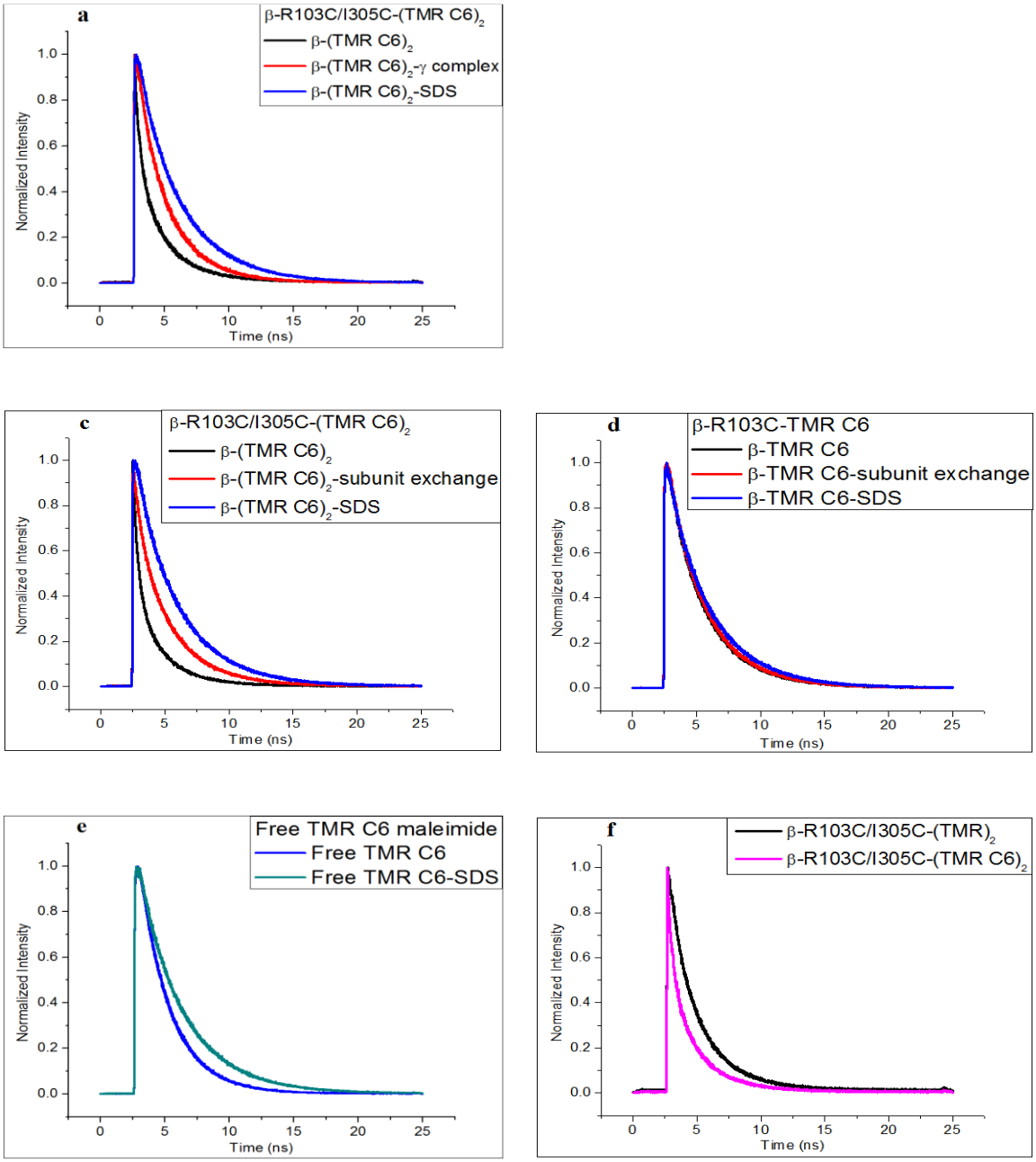

Figure 5.10: TCSPC decays of β- R103C/I305C-(TMR C6)$_2$ (a and c), β- R103C-TMR C6 (d), and free TMR C6 maleimide (e). All dye-labeled β concentrations were 0.5 µM. For subunit exchange, a twenty-fold excess of unlabeled wild-type β (10 µM) was mixed with 0.5 µM dye-labeled β. The samples were stored for two days at room temperature in the dark. The excitation wavelength was 540 nm while the wavelength of collected emission was 575 nm. Panels (a-b) show the effects of 2 µM γ complex and 1% SDS on the TCSPC decays. Panels (c-d) show the effects of subunit exchange and 1% SDS on the decays. Panel (e) shows the effects of 1% SDS on the decay of 1 µM free TMR C6 in water. Panel (f) is an overlap of the decays for β-(TMR C6)$_2$ and β-(TMR)$_2$.

In Figures 5.11a through 5.11g, the time-resolved fluorescence anisotropy decays of β-R103C/I305C-$(TMR)_2$, β-I305C-TMR, β-R103C/I305C-$(TMR\ C6)_2$, and β-R103C-TMR C6 were recorded before and after subunit exchange was carried out. As a control, the anisotropy decays of free TMR maleimide and free TMR C6 maleimide were also recorded. Figures 5.11a and 5.11b indicated that the anisotropy decays of both β-R103C/I305C-$(TMR)_2$ and β-R103C/I305C-$(TMR\ C6)_2$ rose upon subunit exchange. Figure 5.11c overlapped β-R103C/I305C-$(TMR)_2$, β-R103C/I305C-$(TMR\ C6)_2$, and their corresponding subunit-exchanged samples. The overlap revealed that β-R103C/I305C-$(TMR\ C6)_2$ had a lower fundamental anisotropy r_0 (close to 0.2) than β-R103C/I305C-$(TMR)_2$. This property indicated that a rapid depolarization occurred in the anisotropy decay of β-R103C/I305C-$(TMR\ C6)_2$. Simulations of convolutions of anisotropy decays with excitation pulse functions of finite width demonstrated that ultrafast processes within the Instrument Response Function (IRF) can lower the fundamental anisotropy.[119] Instantaneous depolarizations in the anisotropy decays of *Azotobacter vinelandii* apoflavodoxin have been attributed to a 50-ps energy migration among tryptophans.[120, 121] The anisotropy decays of constructs of fluorescent proteins such as Cerulean-Cerulean and Venus-Venus displayed rapid depolarizations suggesting energy migrations/energy transfers between "like" molecules.[122] The trends from Figures 5.11a through 5.11c suggested that energy transfers like homo-Förster Resonance Energy Transfer (homo-FRET) were occurring at the doubly-labeled interfaces and that subunit exchange disrupted the energy transfers by decreasing the number of dyes per interface. FRET is considered to be a dynamic quenching mechanism. Therefore, the stronger degree of

energy transfer observed with β-R103C/I305C-(TMR C6)$_2$ caused the greater degree of dynamic quenching in the TCSPC decay of β-R103C/I305C-(TMR C6)$_2$ in Figure 5.10f.

Figure 5.11d revealed that the anisotropy decay of β-I305C-TMR did not change upon subunit exchange. Figure 5.11e indicated that the anisotropy decays of subunit-exchanged β-R103C/I305C-(TMR)$_2$ and β-R103C/I305C-(TMR C6)$_2$ closely overlapped with those of β-I305C-TMR suggesting that enough subunit exchange occurred to disrupt the likely energy transfers at the doubly labeled interfaces. Figure 5.11f showed the anisotropy decays of free TMR maleimide and free TMR C6 maleimide decaying quickly with a rotational correlation time of a few hundred picoseconds as would be expected of free dyes. Figure 5.11g revealed that the anisotropy decay of β-R103C-TMR C6 did not significantly change upon subunit exchange.

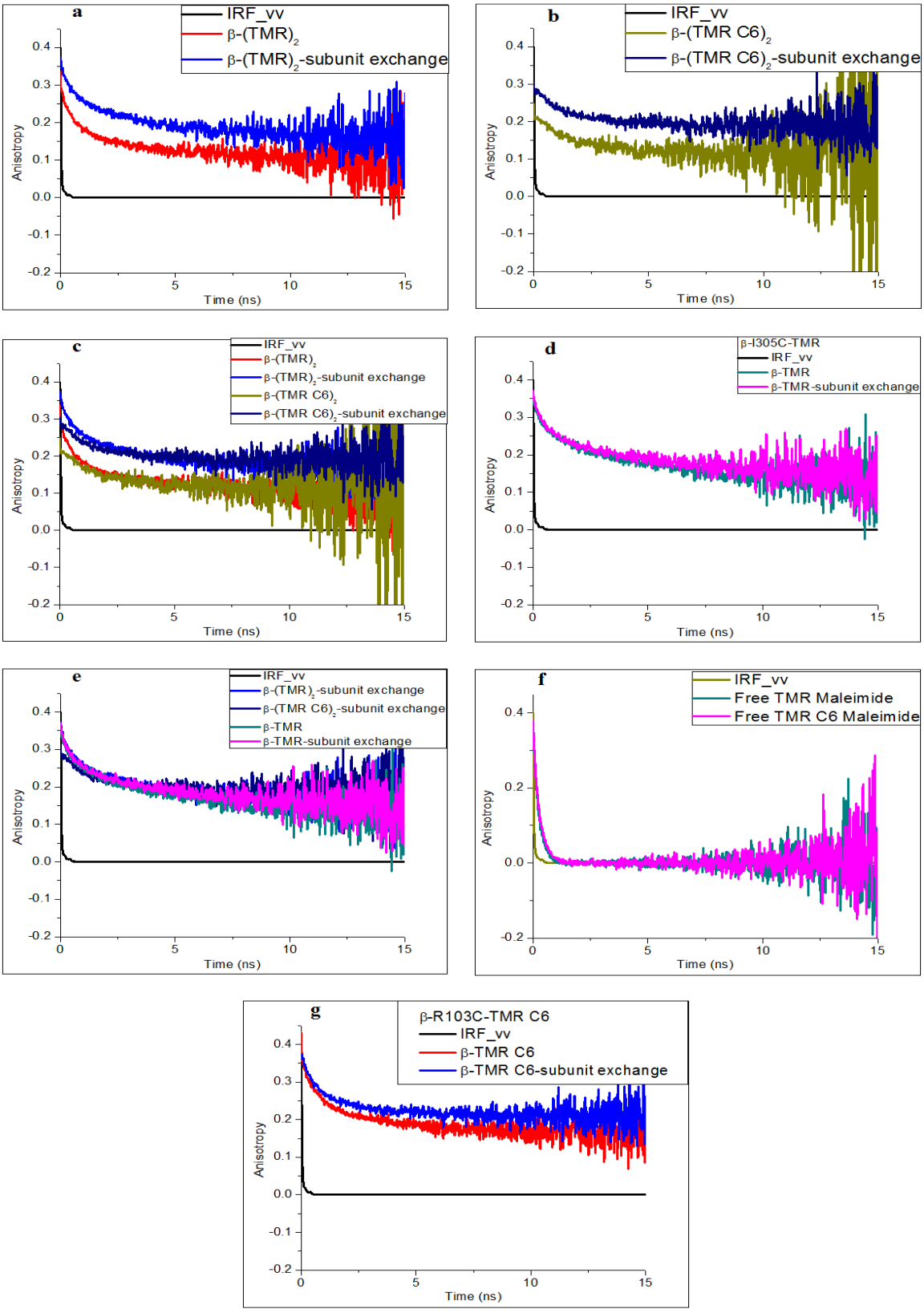
a
IRF_vv
β-(TMR)2
β-(TMR)2-subunit exchange
b
IRF_vv
β-(TMR C6)2
β-(TMR C6)2-subunit exchange
c
IRF_vv
β-(TMR)2
β-(TMR)2-subunit exchange
β-(TMR C6)2
β-(TMR C6)2-subunit exchange
d
β-I305C-TMR
IRF_vv
β-TMR
β-TMR-subunit exchange
e
IRF_vv
β-(TMR)2-subunit exchange
β-(TMR C6)2-subunit exchange
β-TMR
β-TMR-subunit exchange
f
IRF_vv
Free TMR Maleimide
Free TMR C6 Maleimide
g
β-R103C-TMR C6
IRF_vv
β-TMR C6
β-TMR C6-subunit exchange
Anisotropy
Time (ns)

Figure 5.11: Anisotropy decays before and after subunit exchange of β-R103C/I305C-$(TMR)_2$ (a,c, and e), β-I305C-TMR (d and e), β-R103C/I305C-$(TMR\ C6)_2$ (b,c and e), β-R103C-TMR C6 (g), free TMR maleimide (f), and free TMR C6 maleimide (f). All dye-labeled β concentrations were 0.5 μM. For subunit exchange, a twenty-fold excess of unlabeled wild-type β (10 μM) was mixed with 0.5 μM dye-labeled β. The subunit-exchanged samples were stored for two days at room temperature in the dark. All free dye concentrations were 1 μM in water. The excitation wavelength was 540 nm while the wavelength of collected emission was 575 nm.

For β-R103C/I305C-$(Alexa\ Fluor\ 546)_2$ and β-I305C-Alexa Fluor 546, TCSPC decays were collected before and after γ complex and SDS were added and before and after subunit exchange was carried out. The TCSPC fitting parameters are reported in Table 6.3. As shown in Figure 5.12a, the TCSPC decay of β-$(Alexa\ Fluor\ 546)_2$ was initially quenched with three fluorescence lifetimes recovered from the fitting (τ_1 = 3.1 ns (16%), τ_2 = 0.8 ns (34%), and τ_3 = 0.1 ns (50%)). The average fluorescence lifetime of β-$(Alexa\ Fluor\ 546)_2$ was 0.8 ns. It was surprising that this short τ_3 was still present because no clear H-dimers were detected in the absorbance scans of Figures 5.5a and 5.5c. However, that slightly raised absorbance shoulder of β-$(Alexa\ Fluor\ 546)_2$ could indicate weak aggregation.

In Figure 5.12a, when γ complex was added or when subunit exchange was carried out, the TCSPC decay kinetics of β-$(Alexa\ Fluor\ 546)_2$ moderately lengthened with an average fluorescence lifetime of 1.5 ns. When SDS was added to β-$(Alexa\ Fluor\ 546)_2$, a longer lifetime of 3.8 ns was recovered.

In Figure 5.12b, the TCSPC decay of β-I305C-Alexa Fluor 546 could be fit with two lifetimes (τ_1 = 3.8 ns (90%) and τ_2 = 1.3 ns (10%)). When γ complex was added and when subunit exchange was carried out, the TCSPC decay kinetics did not change in agreement with the absorbance trends from Figure 5.5d and the excitation trends from Figure 5.6b. When SDS was added, the TCSPC decay kinetics negligibly changed in

agreement with the absorbance trends from Figures 5.5b and 5.5d and the excitation trends from Figure 5.6b.

In Figure 5.12c, the TCSPC decay of free Alexa Fluor 546 C_5 maleimide was initially quenched with three lifetime components (τ_1 = 3.4 ns (21%), τ_2 = 1.6 ns (41%), and τ_3 = 0.2 ns (38%)). The TCSPC decay kinetics of this free dye were surprising because a monoexponential decay had been expected. Dissolving the free Alexa Fluor 546 in D_2O also resulted in a triexponential decay (τ_1 = 3.5 ns (32%), τ_2 = 1.5 ns (32%), and τ_3 = 0.2 ns (36%)). However, the addition of SDS to the aqueous solution or dissolving the dye in ethanol resulted in biexponential decays that were not as quenched.

Matsumoto et al. reported that a donor-excited photoinduced electron transfer (PET) can occur between BODIPY dyes and maleimide reactive groups. The position of the maleimide group was varied to determine the effects of the maleimide on the PET. Ortho-substituted maleimide derivatives of BODIPY displayed the strongest PET and therefore the strongest fluorescence quenching. Meta-substituted maleimide derivatives of BODIPY displayed somewhat weaker PET and therefore less fluorescence quenching. Para-substituted maleimide derivatives of BODIPY displayed the least PET, the least fluorescence quenching, and the strongest fluorescence signal. However, when the *o*-maleimideBODIPY was reacted with thiols, there was a substantial enhancement of the fluorescence (350-fold).[123]

In light of these findings, we decided to do TCSPC measurements of all free dyes before and after the addition of dithiothreitol (DTT). The TCSPC fitting parameters are reported in Table 6.4. Figures 5.14a and 5.14c indicated that the TCSPC decay kinetics of free TMR maleimide and free TMR C6 maleimide were unaffected by DTT. Figures

6.7a and 6.7b reveal that both TMR dyes have para-substituted maleimide groups. Hence, any PET will be minimized before DTT is even added. In contrast, when DTT was added to free Alexa Fluor 546 maleimide in Figure 5.14b, the quenched triexponential TCSPC decay (τ_1 = 3.1 ns (32%), τ_2 = 1.3 ns (33%), and τ_3 = 0.2 ns (35%)) became a monoexponential decay with a fluorescence lifetime of 3.8 ns. Figure 6.7c reveals that the free Alexa Fluor 546 has a meta-substituted maleimide group. Hence, there will be appreciable PET between the Alexa Fluor 546 and its maleimide moiety. In Figure 5.14d, when DTT was added to free Alexa Fluor 488 maleimide, the biexponential TCSPC decay (τ_1 = 4.0 ns (81%) and τ_2 = 1.7 ns (19%)) became a monoexponential decay with a fluorescence lifetime of 4.0 ns. Figure 6.7d reveals that the free Alexa Fluor 488 consists of a mixture of meta- and para-substituted maleimide groups. Hence, the degree of PET between Alexa Fluor 488 and its maleimide moiety will be intermediate to that of TMR and Alexa Fluor 546.

Absorbance scans and excitation scans of the free rhodamine maleimide dyes without and with DTT supported the trends in the TCSPC measurements. Figure 6.2 revealed no changes in the shapes of the absorbance scans of any of the free rhodamine maleimide dyes with DTT. Figure 6.4 indicated negligible changes to the fluorescence intensities and shapes of the excitation scans of free TMR maleimide, free TMR C6 maleimide, and free unreactive TAMRA with DTT. While Figures 6.6c and 6.6d displayed no changes to the shapes of the excitation scans of free Alexa Fluor 546 maleimide and free Alexa Fluor 488 maleimide with DTT, Figure 6.6a indicated a 2-fold increase in the fluorescence intensity of free Alexa Fluor 546 maleimide with DTT, and Figure 6.6b indicated a modest increase in the fluorescence intensity of free Alexa Fluor

488 maleimide with DTT. The higher enhancement in fluorescence intensity observed with free Alexa Fluor 546 maleimide upon addition of DTT matched the pronounced increase in its fluorescence lifetime under the same conditions. The modest enhancement in fluorescence intensity observed with free Alexa Fluor 488 maleimide upon addition of DTT matched the modest increase in its fluorescence lifetime under the same conditions.

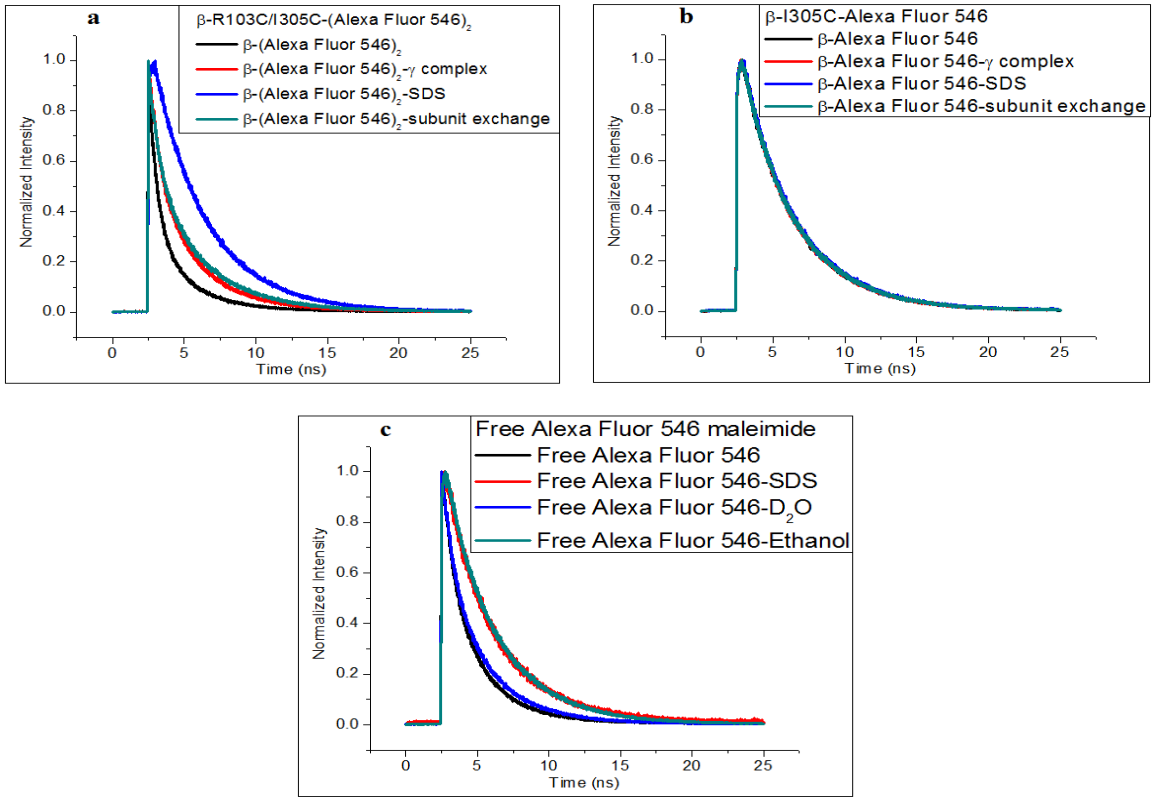

Figure 5.12: TCSPC decays of β-R103C/I305C-(Alexa Fluor 546)$_2$ (a), β-I305C-Alexa Fluor 546 (b), and free Alexa Fluor 546 maleimide (c). All dye-labeled β concentrations were 0.5 μM. For subunit exchange, a twenty-fold excess of unlabeled wild-type β (10 μM) was mixed with 0.5 μM dye-labeled β. The subunit-exchanged samples were stored for two days at room temperature in the dark. The excitation wavelength was 540 nm while the wavelength of collected emission was 575 nm. Panels (a) and (b) show the effects of 2 μM γ complex, 1% SDS, and subunit exchange on the TCSPC decays. Panel (c) shows the effects of 1% SDS, D_2O, and ethanol on the TCSPC decay of free Alexa Fluor 546 maleimide.

In Figures 5.13a and 5.13b, the time-resolved fluorescence anisotropy decays of β-R103C/I305C-(Alexa Fluor 546)$_2$ and β-I305C-Alexa Fluor 546 were recorded before

and after subunit exchange was carried out. As a control, the anisotropy decay of free Alexa Fluor 546 maleimide was also recorded. Figure 5.13a indicated that the anisotropy decay of β-R103C/I305C-(Alexa Fluor 546)$_2$ displayed an instantaneous depolarization with a r_0 close to 0.2 as was observed with β-R103C/I305C-(TMR C6)$_2$ and that the anisotropy decay rose upon subunit exchange. This rapid depolarization strongly suggested that energy transfers and dynamic quenching were occurring at the doubly labeled interfaces. It should also be noted both TMR C6 and Alexa Fluor 546 had longer linkers. In summary, the quenching in β-(Alexa Fluor 546)$_2$ was a combination of static and dynamic quenching but with a larger degree of dynamic quenching.

Figure 5.13b revealed that the anisotropy decay of β-I305C-Alexa Fluor 546 did not change upon subunit exchange. Figure 5.13b also showed the anisotropy decay of free Alexa Fluor 546 maleimide decaying quickly with a rotational correlation time of a few hundred picoseconds as would be expected of free dyes.

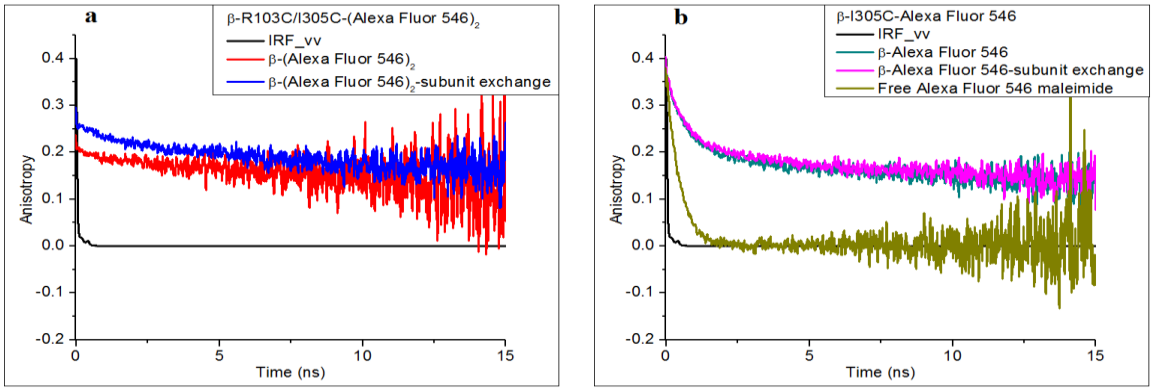

Figure 5.13: Anisotropy decays before and after subunit exchange of β-R103C/I305C-(Alexa Fluor 546)$_2$ (a), β-I305C-Alexa Fluor 546 (b), and free Alexa Fluor 546 maleimide (b). All dye-labeled β were 0.5 μM. For subunit exchange, 10 μM unlabeled wild-type β was mixed with 0.5 μM dye-labeled β. The samples were stored for two days at room temperature in the dark. All free dye were 1 μM in water. The excitation wavelength was 540 nm while the wavelength of collected emission was 575 nm.

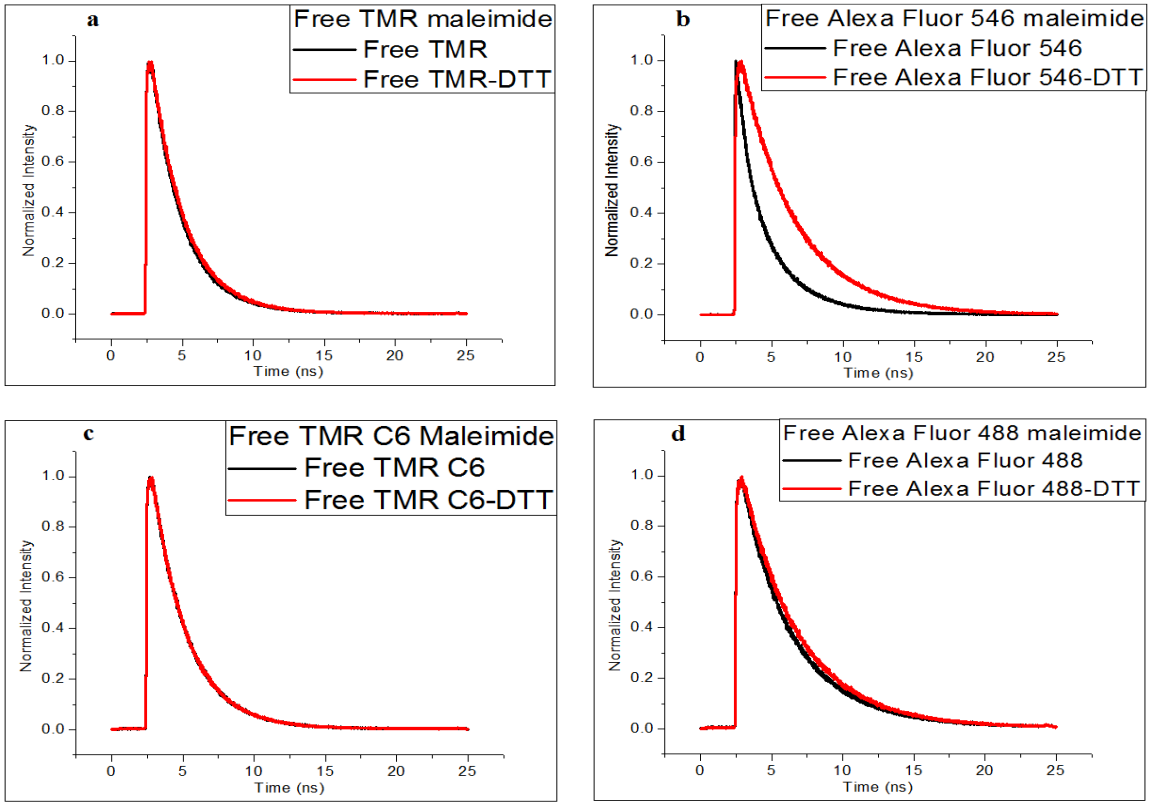

Figure 5.14: TCSPC decays of free TMR maleimide (a: λ_{Ex} = 540 nm, λ_{Em} = 590 nm), free Alexa Fluor 546 maleimide (b: λ_{Ex} = 540 nm, λ_{Em} = 570 nm), free TMR C6 maleimide (c: λ_{Ex} = 540 nm, λ_{Em} = 590 nm), and free Alexa Fluor 488 maleimide (d: λ_{Ex} = 500 nm, λ_{Em} = 540 nm) in water. Panels (a-d) show the effects of 5 mM DTT on the TCSPC decays of the 1 µM free dyes.

For β-R103C/I305C-(Alexa Fluor 488)$_2$ and β-I305C-Alexa Fluor 488, TCSPC decays were collected before and after γ complex and SDS were added and before and after subunit exchange was carried out. The TCSPC fitting parameters are reported in Table 6.5. As shown in Figures 5.15a and 5.15c, the TCSPC decay of β-(Alexa Fluor 488)$_2$ was initially quenched with three fluorescence lifetimes recovered from the fitting (τ_1 = 3.3 ns (21%), τ_2 = 1.1 ns (13%), and τ_3 = 0.1 ns (67%)). The average fluorescence lifetime of β-(Alexa Fluor 488)$_2$ was 0.9 ns. It was surprising that this short τ_3 was still present because no clear H-dimers were detected in the absorbance scans of Figure 5.7a. Unlike β-(Alexa Fluor 546)$_2$, there was no slightly raised short-wavelength absorbance

shoulder indicating weak aggregation. This fact suggested that the quenching in β-(Alexa Fluor 488)$_2$ was entirely dynamic.

In Figures 5.15a and 5.15c, when γ complex was added or when subunit exchange was carried out, the TCSPC decay kinetics of β-R103C/I305C-(Alexa Fluor 488)$_2$ moderately lengthened with an average fluorescence lifetime of 2.1 ns. When SDS was added to β-R103C/I305C-(Alexa Fluor 488)$_2$, a longer lifetime of 4.0 ns was recovered.

In Figures 5.15b and 5.15d, the TCSPC decay of β-I305C-Alexa Fluor 488 could be fit with two lifetimes (τ_1 = 3.9 ns (89%) and τ_2 = 1.1 ns (11%)). When γ complex was added and when subunit exchange was carried out, the TCSPC decay kinetics did not change in agreement with the absorbance trends from Figure 5.7b and the excitation trends from Figure 5.8b. When SDS was added, the TCSPC decay kinetics negligibly changed in agreement with the absorbance trends from Figure 5.7b and the excitation trends from Figure 5.8b.

In Figures 5.16a through 5.16c, the time-resolved fluorescence anisotropy decays of β-R103C/I305C-(Alexa Fluor 488)$_2$ and β-I305C-Alexa Fluor 488 were recorded before and after subunit exchange was carried out. As a control, the anisotropy decay of free Alexa Fluor 488 maleimide was also recorded. Figure 5.16a indicated that the anisotropy decay of β-R103C/I305C-(Alexa Fluor 488)$_2$ displayed an instantaneous depolarization with a r_0 close to 0.2 as was observed with β-R103C/I305C-(TMR C6)$_2$ and β-R103C/I305C-(Alexa Fluor 546)$_2$. Figure 5.16a also indicated that the anisotropy decay rose upon subunit exchange. This rapid depolarization strongly suggested that energy transfers and dynamic quenching were occurring at the doubly labeled interfaces. A similar rapid depolarization was reported for anisotropy decays of phospholipid

bilayers with a high membrane surface density of Alexa Fluor 488-labeled lysozyme.[124] It should also be noted that TMR C6, Alexa Fluor 546, and Alexa Fluor 488 all had longer linkers. With no signs of aggregation in the absorbance scans and with evidence of energy transfers, the quenching in β-R103C/I305C-(Alexa Fluor 488)$_2$ was entirely dynamic.

Unfortunately, it was difficult to determine which dynamic quenching mechanism was responsible for the quenched TCSPC decays of β-R103C/I305C-(Alexa Fluor 488)$_2$. We did have strong evidence for homo-FRET occurring at the doubly labeled interfaces, and FRET is considered to be a dynamic quenching mechanism. However, homo-FRET only decreases the fluorescence anisotropy, not the fluorescence lifetime or intensity. Since both donor and acceptor are chemically identical, the gain of the acceptor's lifetime and intensity should be offset by the loss of the donor's lifetime and intensity. Hence, there should be no overall change in the fluorescence lifetime or intensity.[125] Interestingly, recent evidence in literature have indicated that homo-FRET might decrease the fluorescence lifetime. Homo-FRET was reported as shortening the fluorescence lifetime of constructs of fluorescent proteins such as Cerulean-Cerulean and Venus-Venus by a few hundred picoseconds.[122] The fluorescence lifetime of enhanced Green Fluorescent Protein (eGFP) decreased by a few hundred picoseconds upon the expression of eGFP in expanded, aggregated polyglutamine (polyQ) tracts.[126] Studies of antibodies labeled with multiple Seta-670 dyes observed decreases in fluorescence lifetime that were once again attributed to homo-FRET.[127] Nicoli et al. studied energy cascades on DNA origami constructs. For one of their constructs triply-labeled with cyanines, they observed instantaneous depolarizations in the anisotropy decays indicating

homo-FRET and a concomitant fluorescence lifetime shortening. Nicoli et al. speculated that homo-FRET can decrease the fluorescence lifetime if the identical dyes are not in identical environments.[128] This present study suggested that the dynamic quenching mechanism responsible for the quenched TCSPC decays of β-(Alexa Fluor 488)$_2$ was homo-FRET.

Figure 5.16b revealed that the anisotropy decay of β-I305C-Alexa Fluor 488 did not change upon subunit exchange. Figure 5.16c showed the anisotropy decay of free Alexa Fluor 488 maleimide decaying quickly with a rotational correlation time of a few hundred picoseconds as would be expected of free dyes.

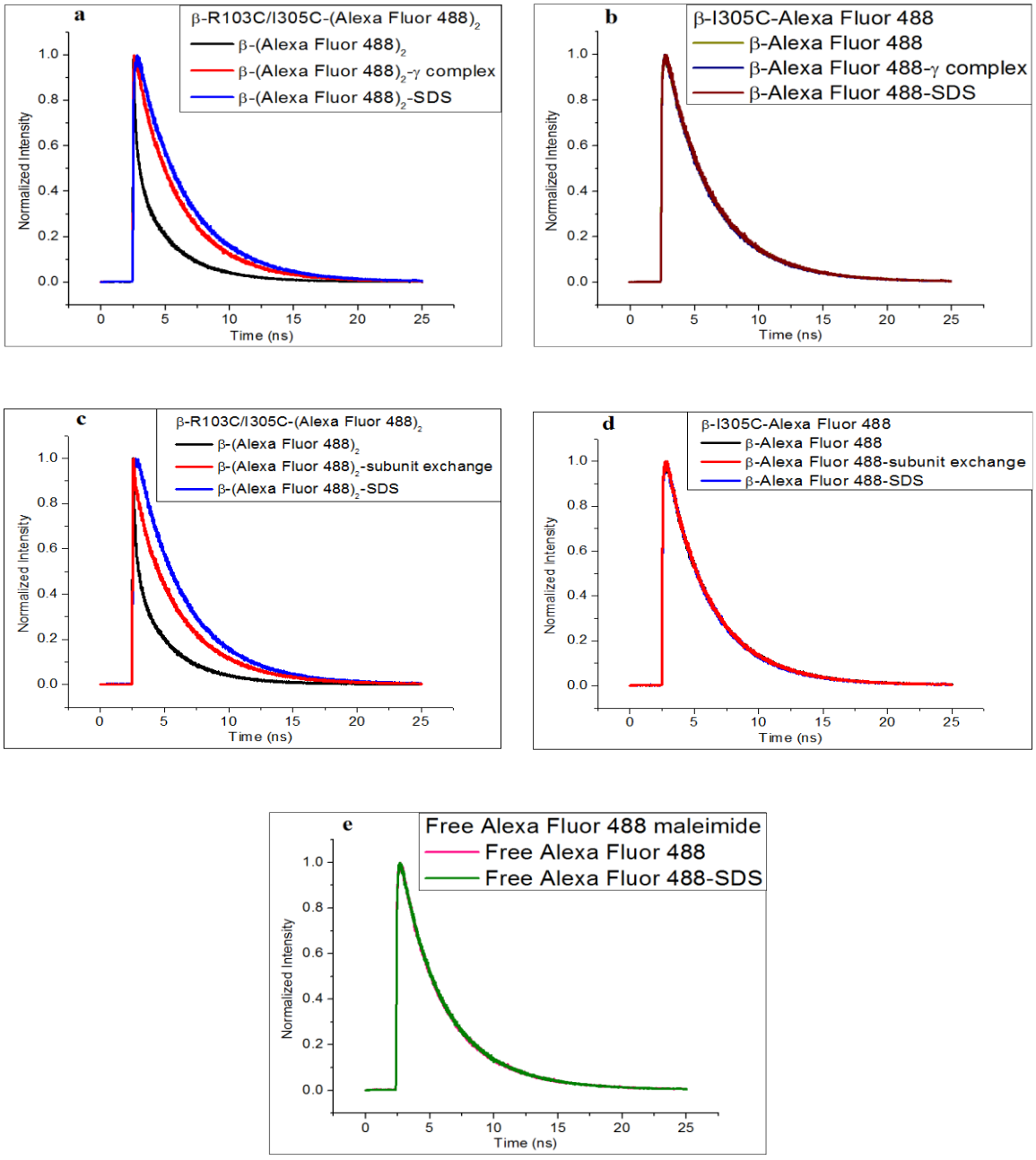

Figure 5.15: TCSPC decays of β-R103C/I305C-(Alexa Fluor 488)$_2$ (a and c), β-I305C-Alexa Fluor 488 (b and d), and free Alexa Fluor 488 maleimide (e). All dye-labeled β were 0.5 μM. For subunit exchange, 10 μM unlabeled wild-type β was mixed with 0.5 μM dye-labeled β. The samples were stored for two days at room temperature in the dark. The excitation wavelength was 500 nm while the wavelength of collected emission was 540 nm. Panels (a-b) show the effects of 2 μM γ complex and 1% SDS on the decays. Panels (c-d) show the effects of subunit exchange on the decays. Panel (e) shows the effects of 1% SDS on the decay of 2 μM free Alexa Fluor 488 maleimide in water.

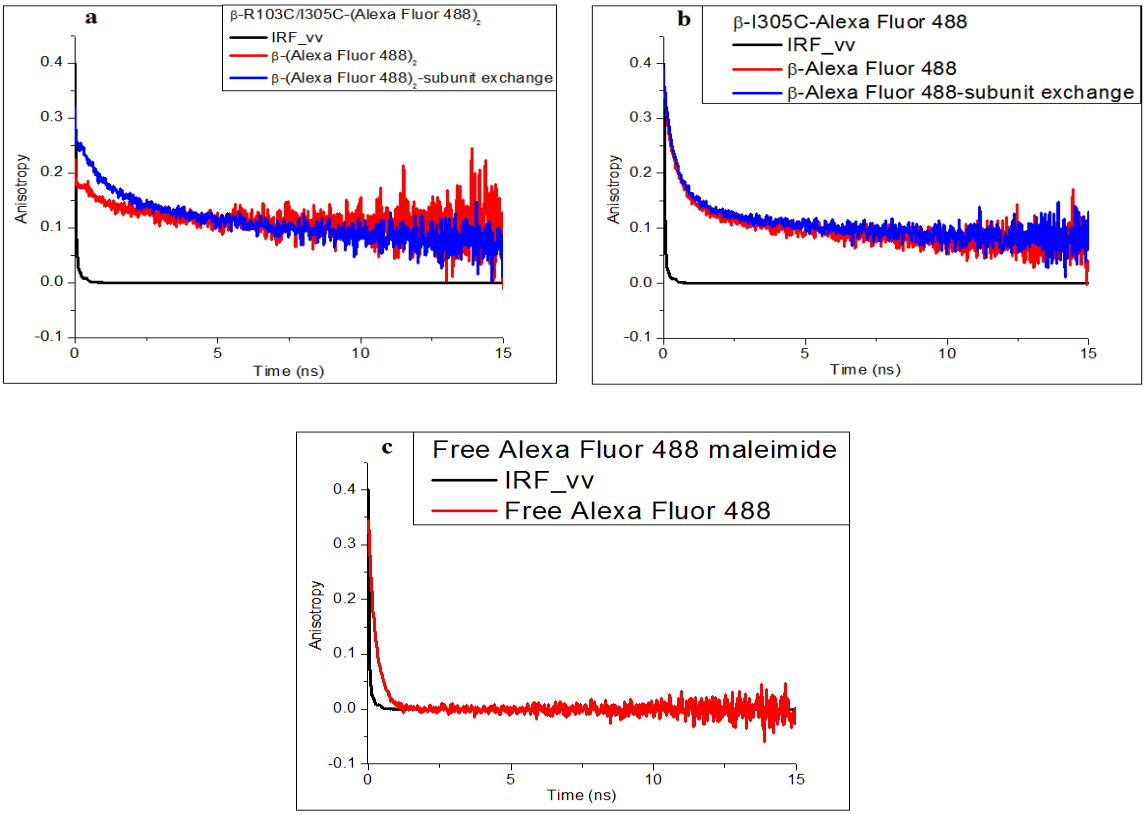

Figure 5.16: Anisotropy decays of β-R103C/I305C-(Alexa Fluor 488)$_2$ (a), β-I305C-Alexa Fluor 488 (b), and free Alexa Fluor 488 maleimide (c). All dye-labeled β concentrations were 0.5 μM. For subunit exchange, a twenty-fold excess of unlabeled wild-type β (10 μM) was mixed with 0.5 μM dye-labeled β. The subunit-exchanged samples were stored for two days at room temperature in the dark. All free dye concentrations were 1 μM in water. The excitation wavelength was 500 nm while the wavelength of collected emission was 540 nm.

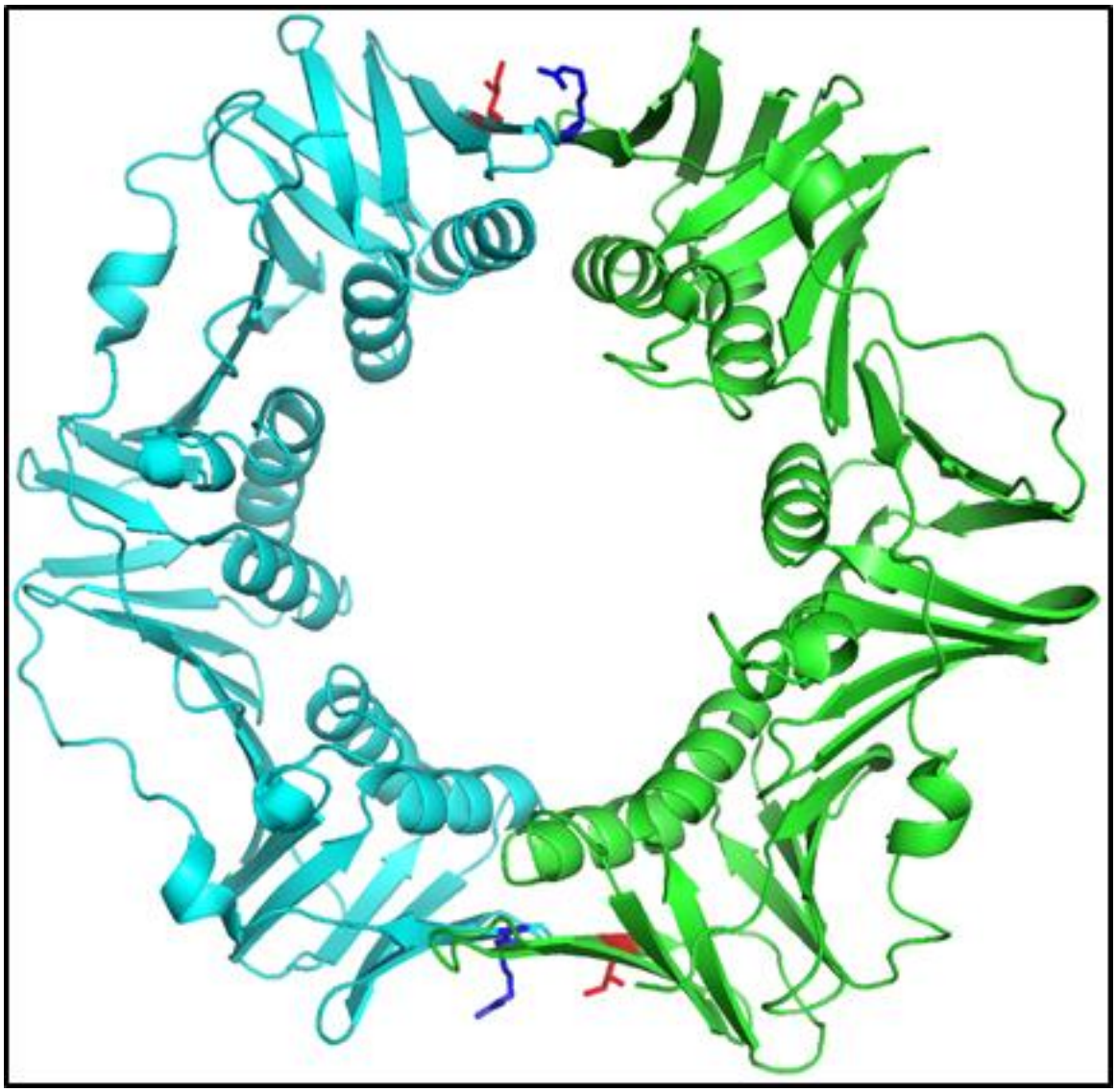

Figure 5.17: PyMOL Image of *E. coli* β clamp. Red and blue indicate the locations of the two amino acid residues at the interface that were mutated into cysteines and labeled with rhodamine dyes. Red is I305 and blue is R103.

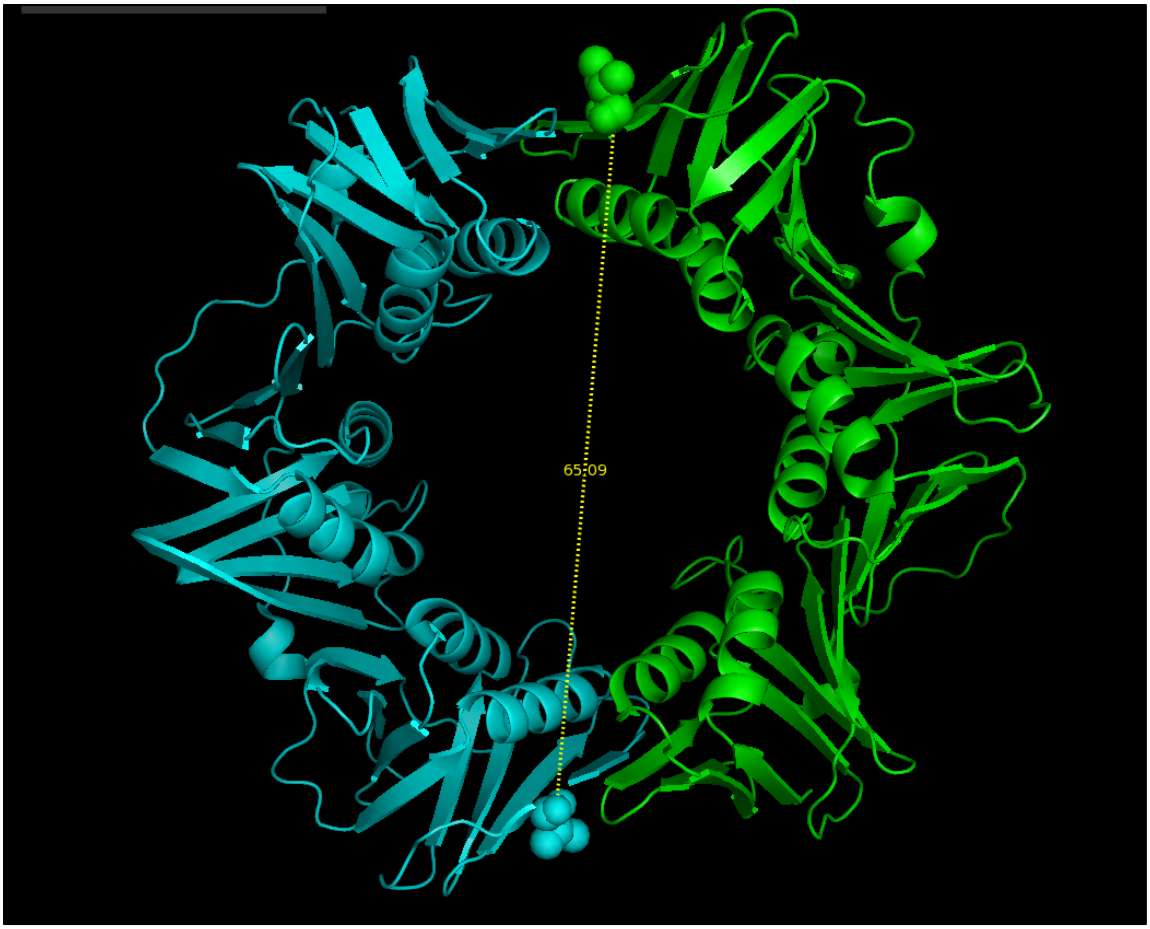

Figure 5.18: Distance between the two I305 residues on the *E. coli* β clamp. The distance was calculated from alpha carbon to alpha carbon. Figure by courtesy of Anirban Purohit.

5.5 Conclusions

This study demonstrated that both TMR and TMR C6 dyes can readily form H-dimers at the doubly-labeled interfaces of the β clamps. The formation of ground-state H-dimers indicated static quenching for both TMR and TMR C6. However, the shorter linker TMR displayed a larger degree of static quenching while the longer linker TMR C6 displayed a larger degree of dynamic quenching with concomitant instantaneous depolarizations in the anisotropy decays indicating homo-FRET and fluorescence lifetime

shortenings. For Alexa Fluor 546 at the doubly-labeled interfaces, absorbance scans and excitation scans suggested weak aggregation with intermediate geometry between that of H-dimers and J-dimers. However, for Alexa Fluor 546, the degree of dynamic quenching was stronger with concomitant instantaneous depolarizations in the anisotropy decays indicating homo-FRET and fluorescence lifetime shortenings. For Alexa Fluor 488 at the doubly-labeled interfaces, there were no clear signs of ground-state dimerization in the absorbance scans. Instead, for Alexa Fluor 488, the quenching was entirely dynamic with concomitant instantaneous depolarizations in the anisotropy decays indicating homo-FRET and fluorescence lifetime shortenings. The three dyes (TMR C6, Alexa Fluor 546, and Alexa Fluor 488) that displayed a greater degree of dynamic quenching all had longer linkers. Therefore, the linker length might play a role in governing the interchromophoric interactions.

CHAPTER SIX

SUPPORTING INFORMATION:

INTERCHROMOPHORIC EFFECTS OF TMR AND ALEXA FLUOR DYES ON *E. COLI* DNA PROCESSIVITY CLAMPS

6.1 Ensemble Absorbance and Excitation Scans of Free Dyes

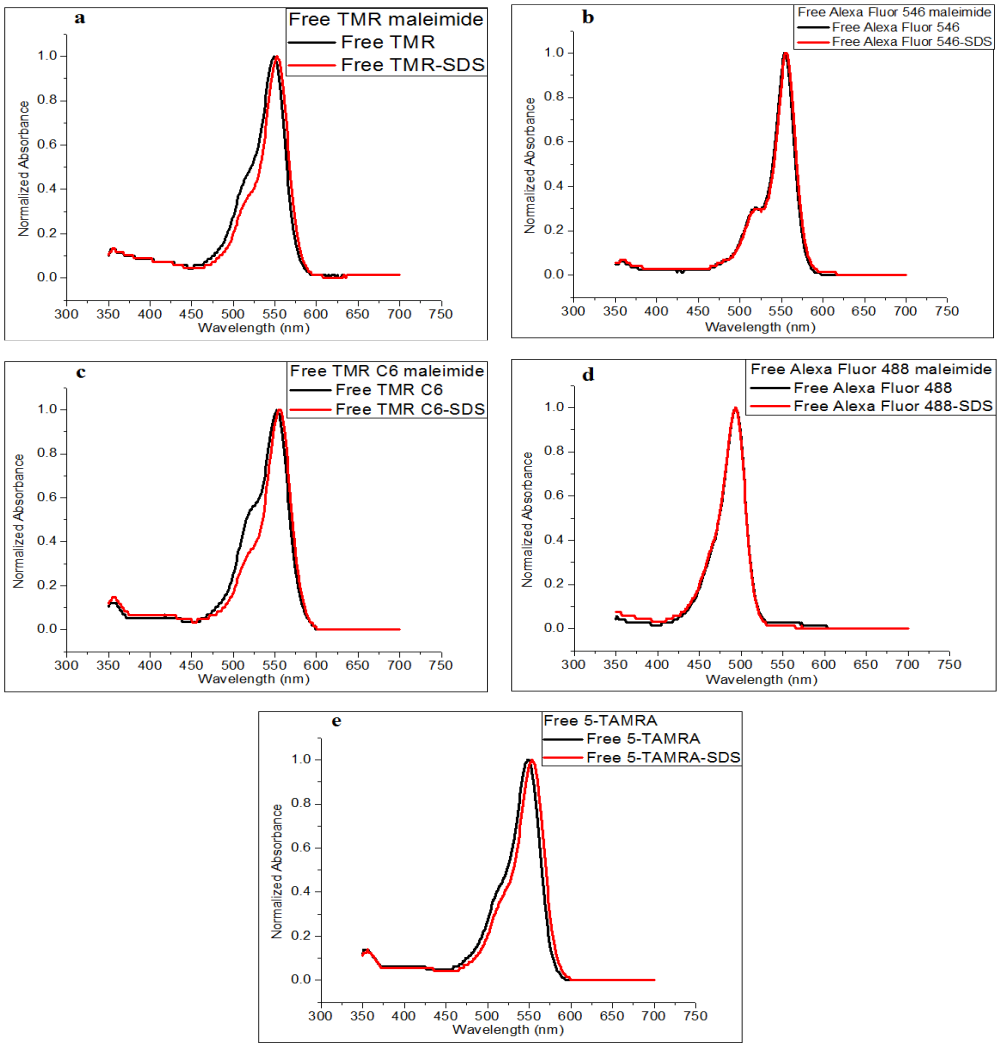

Figure 6.1: Absorbance scans of free TMR maleimide (a), free Alexa Fluor 546 maleimide (b), free TMR C6 maleimide (c), free Alexa Fluor 488 maleimide (d), and free unreactive 5-TAMRA in water (e). Panels (a-e) show the effects of 1% SDS on the shapes of the absorbance scans of 1 µM free dyes.

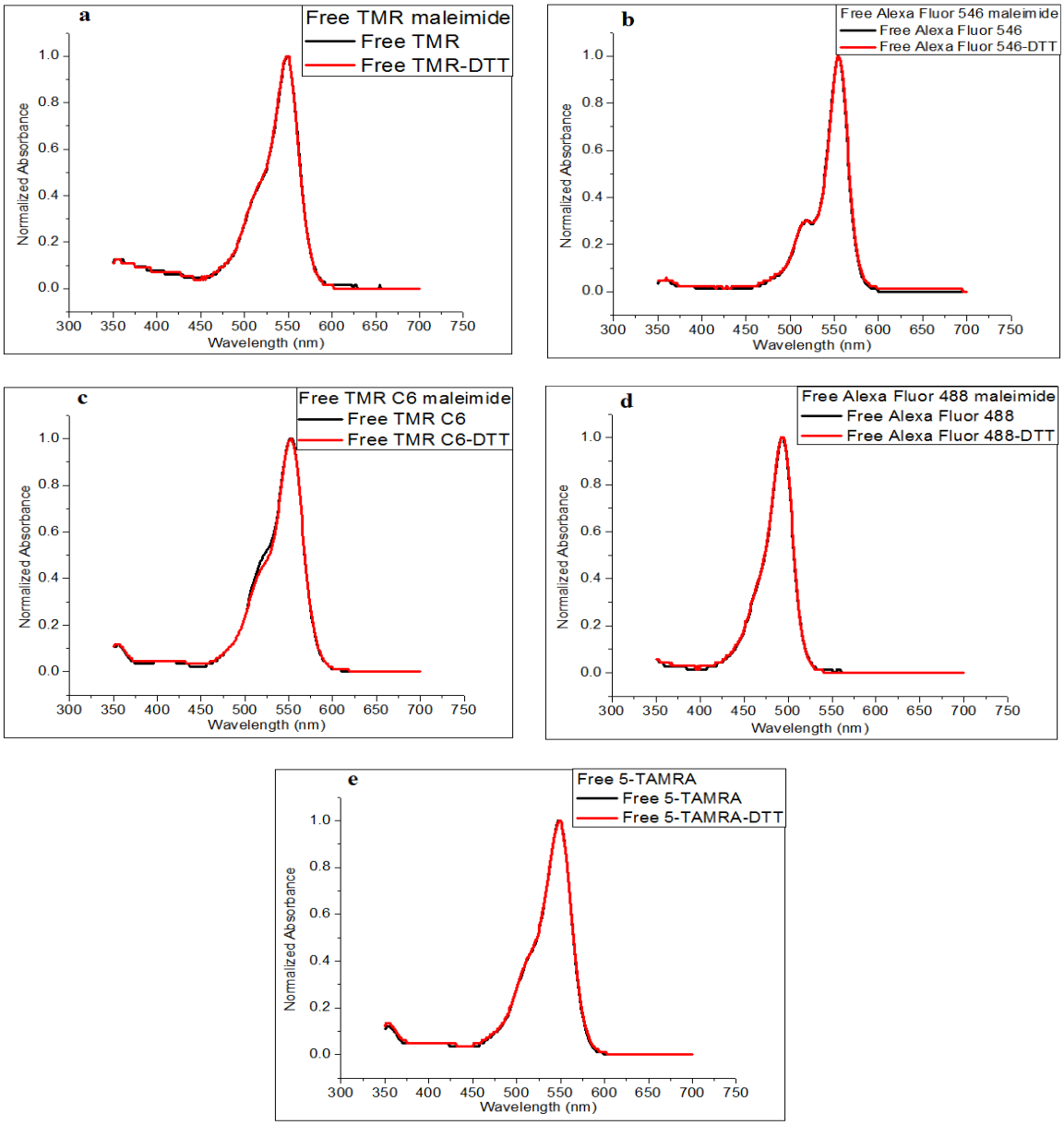

Figure 6.2: Absorbance scans of free TMR maleimide (a), free Alexa Fluor 546 maleimide (b), free TMR C6 maleimide (c), free Alexa Fluor 488 maleimide (d), and free unreactive 5-TAMRA in water (e). Panels (a-e) show the effects of 5 mM DTT on the shapes of the absorbance scans of 1 µM free dyes.

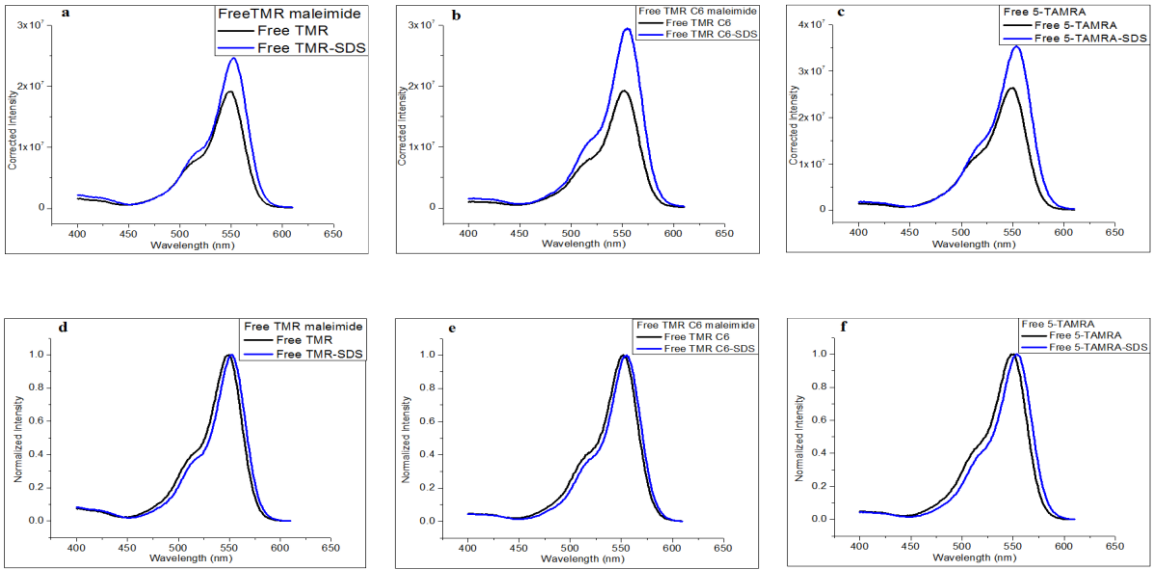

Figure 6.3: Excitation scans of free TMR maleimide (a and d), free TMR C6 maleimide (b and e), and free unreactive 5-TAMRA (c and f). All dye concentrations were 1 µM. The excitation was scanned from 400 nm to 610 nm, and the emission was collected at 625 nm. Panels (a-c) and panels (d-f) show the effects of 1% SDS on the intensities and shapes of the excitation spectra.

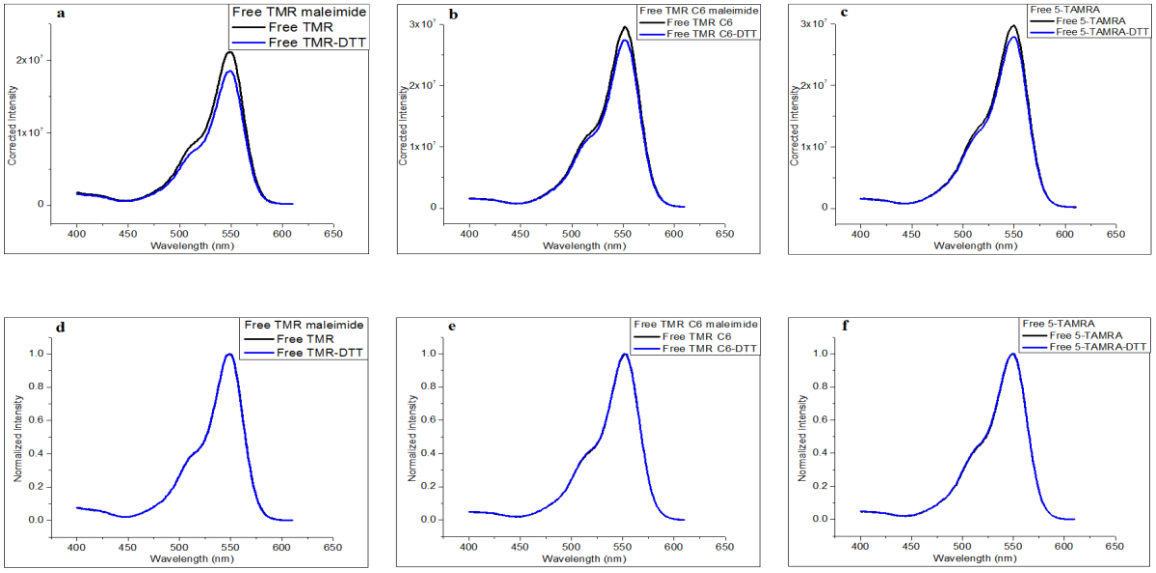

Figure 6.4: Excitation scans of 1 µM TMR maleimide (a and d), TMR C6 maleimide (b and e), and 5-TAMRA (c and f). (λ_{Ex} scanned from 400 nm to 610 nm, λ_{Em} collected at 625 nm). Panels (a-c) and (d-f) show the effects of 5 mM DTT on the intensities and shape of the excitation scans.

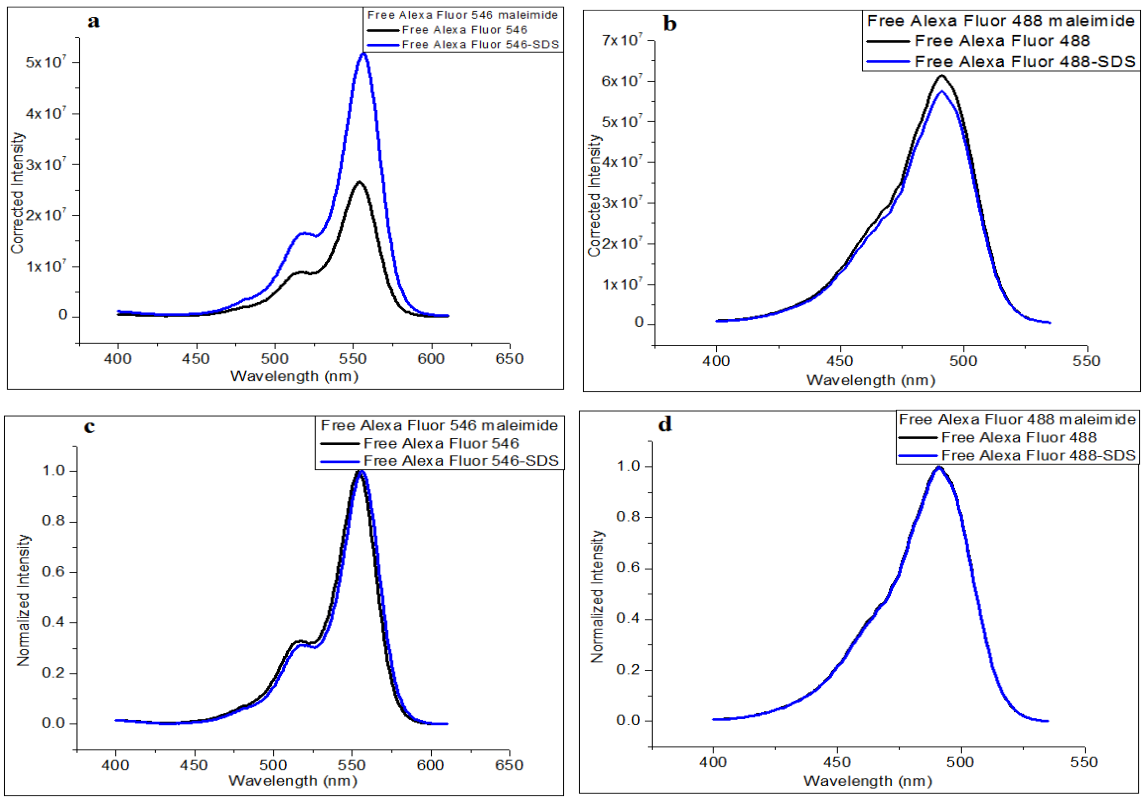

Figure 6.5: Excitation scans of free Alexa Fluor 546 maleimide (a and c: λ_{Ex} scanned from 400 nm to 610 nm, λ_{Em} collected at 625 nm) and free Alexa Fluor 488 maleimide (b and d: λ_{Ex} scanned from 400 nm to 535 nm, λ_{Em} collected at 570 nm) in water. All free dye concentrations were 1 µM. Panels (a-b) and panels (c-d) show the effects of 1% SDS on the intensities and shapes of the excitation spectra respectively.

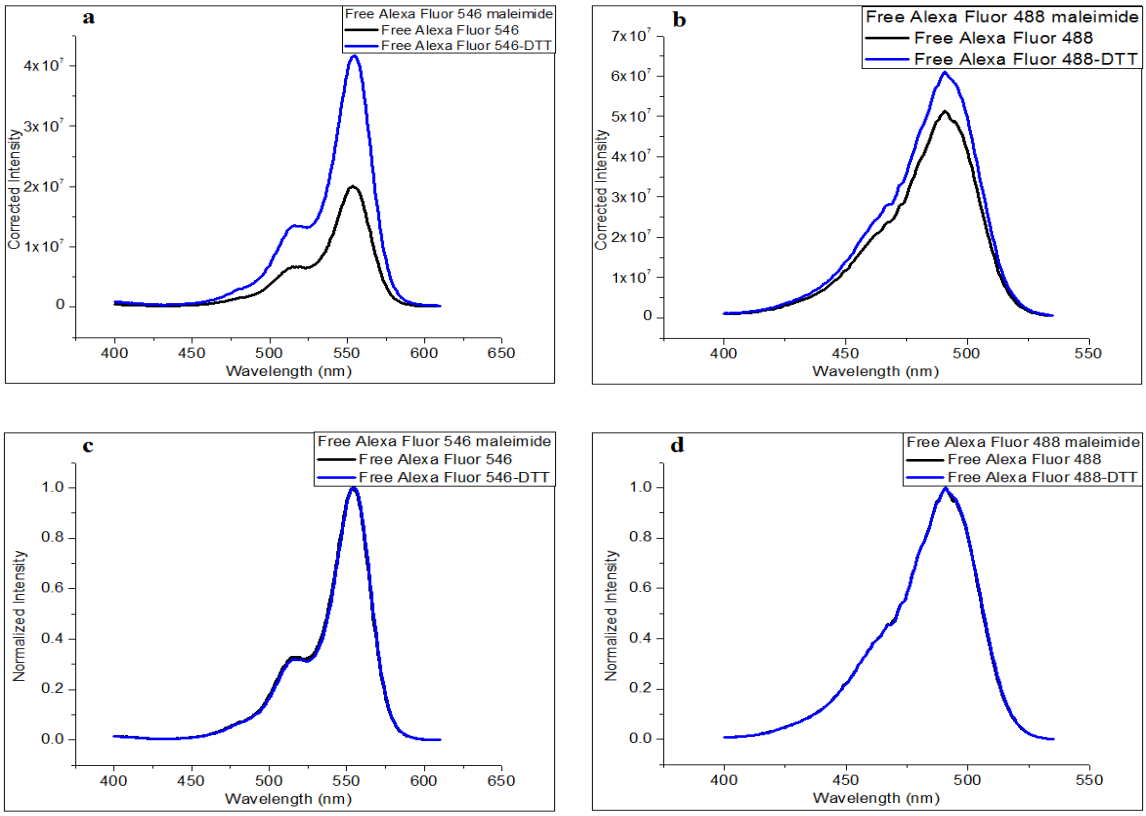

Figure 6.6: Excitation scans of free Alexa Fluor 546 maleimide (a and c: λ_{Ex} scanned from 400 nm to 610 nm, λ_{Em} collected at 625 nm) and free Alexa Fluor 488 maleimide (b and d: λ_{Ex} scanned from 400 nm to 535 nm, λ_{Em} collected at 550 nm) in water. All free dye concentrations were 1 µM. Panels (a-b) and panels (c-d) show the effects of 5 mM DTT on the intensities and shapes of the excitation spectra respectively.

6.2 Structures of Free Rhodamine Dyes

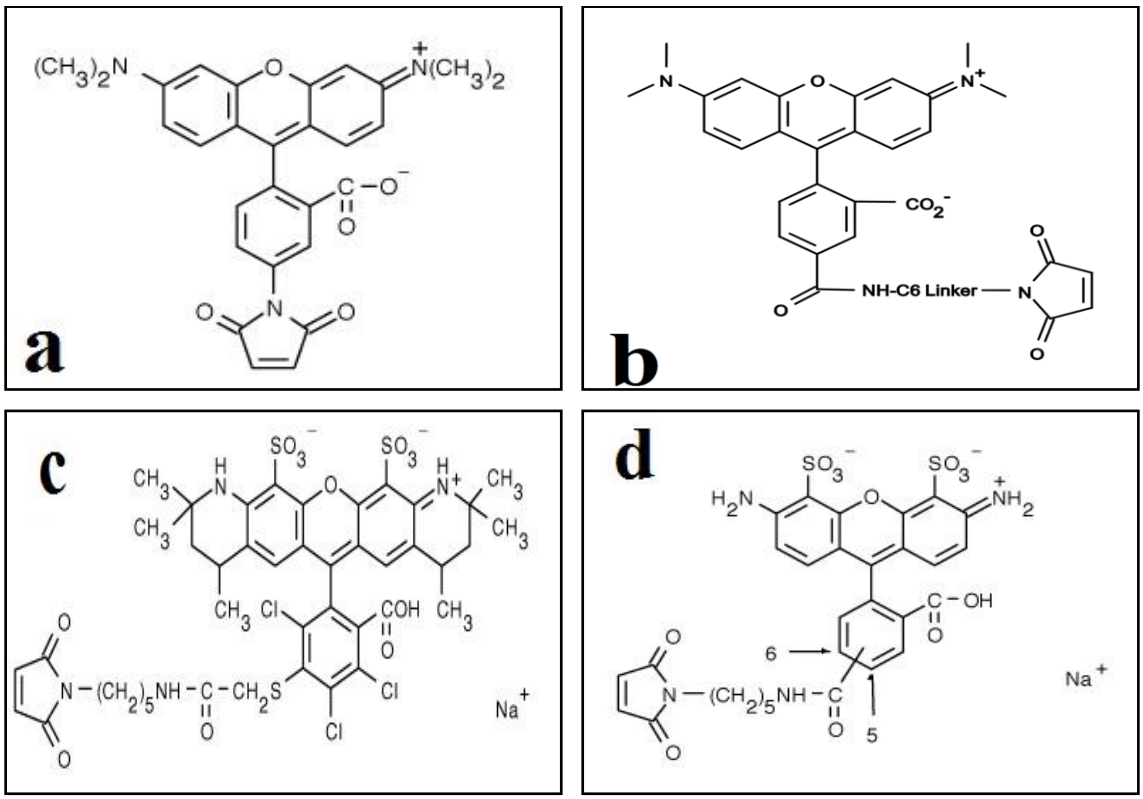

Figure 6.7: Structures of Rhodamines. Tetramethylrhodamine-5-Maleimide[129] (a), 5-TAMRA C6 Maleimide[130] (b), Alexa Fluor 546 C_5 Maleimide[131] (c), and Alexa Fluor 488 C_5 Maleimide[132] (d).

6.3 Ensemble Emission Scans of Dye-Labeled β Clamps

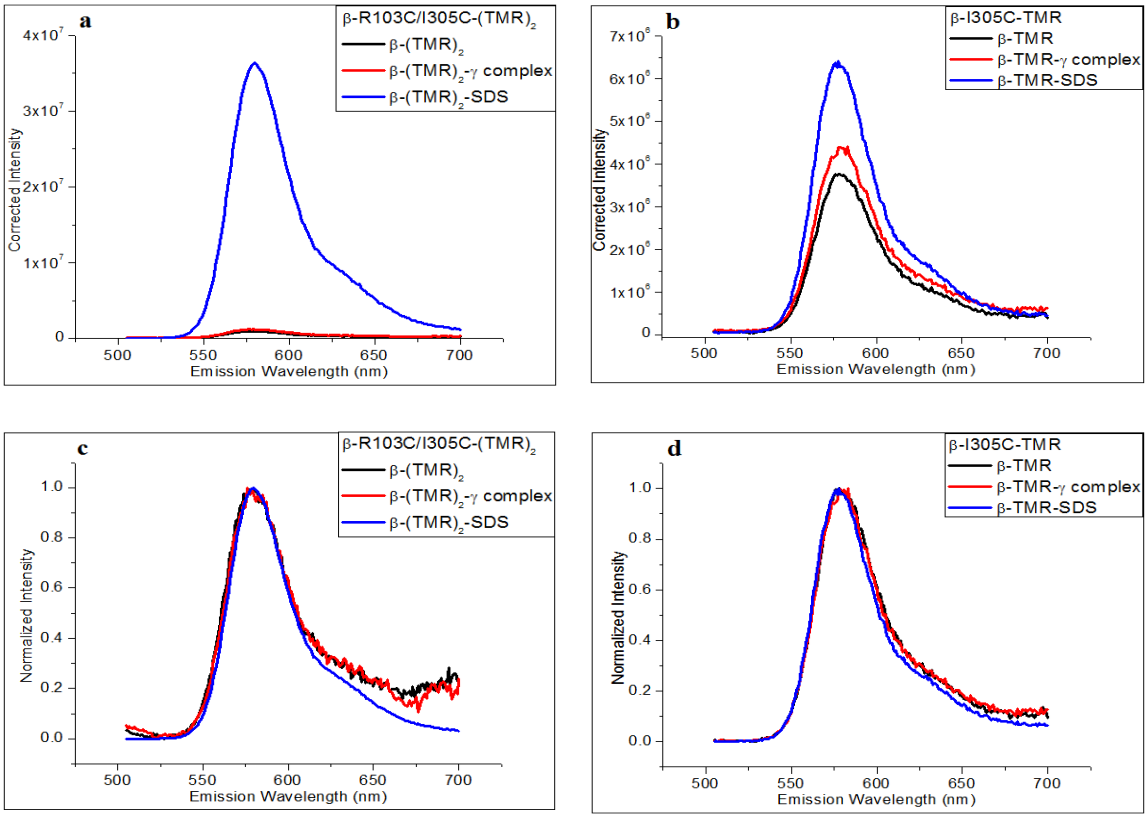

Figure 6.8: Emission scans of β-R103C/I305C-$(TMR)_2$ (a and c) and β-I305C-TMR (b and d). All dye-labeled β were 0.5 μM. The excitation was fixed at 490 nm, and the emission was scanned from 505 nm to 700 nm. Panels (a-b) and panels (c-d) show the effects of 2 μM γ complex and 1% SDS detergent on the intensities and shapes of the emission spectra.

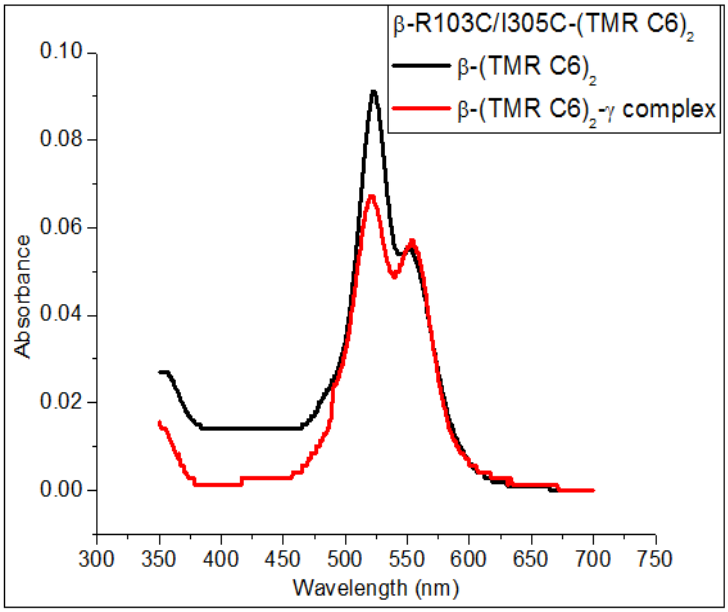

Figure 6.9: Absorbance scans of 0.5 μM β-R103C/I305C-(TMR C6)$_2$ before and after the addition of 2 μM γ complex.

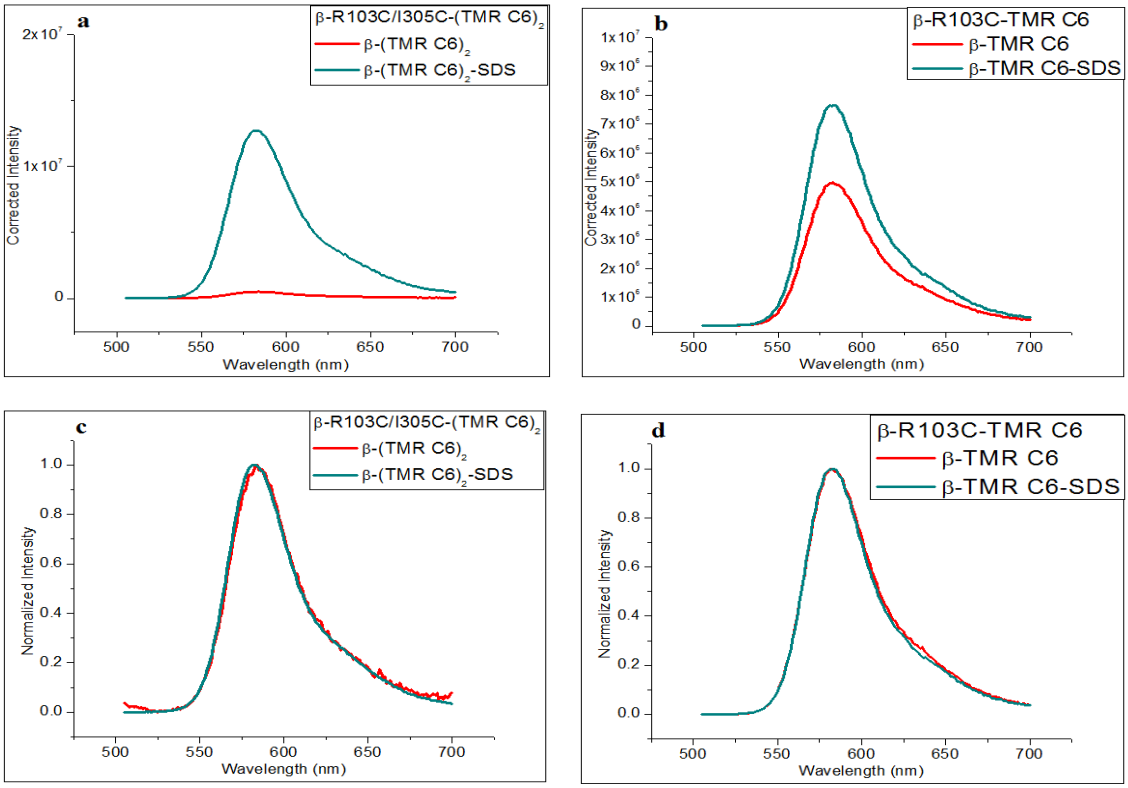

Figure 6.10: Emission scans of β-R103C/I305C-(TMR C6)$_2$ (a and c) and β-R103C-TMR C6 (b and d). All dye-labeled β were 0.5 μM. The excitation was fixed at 490 nm, and the emission was scanned from 505 nm to 700 nm. Panels (a-b) and panels (c-d) show the effects of 1% SDS on the intensities and shapes of the emission spectra.

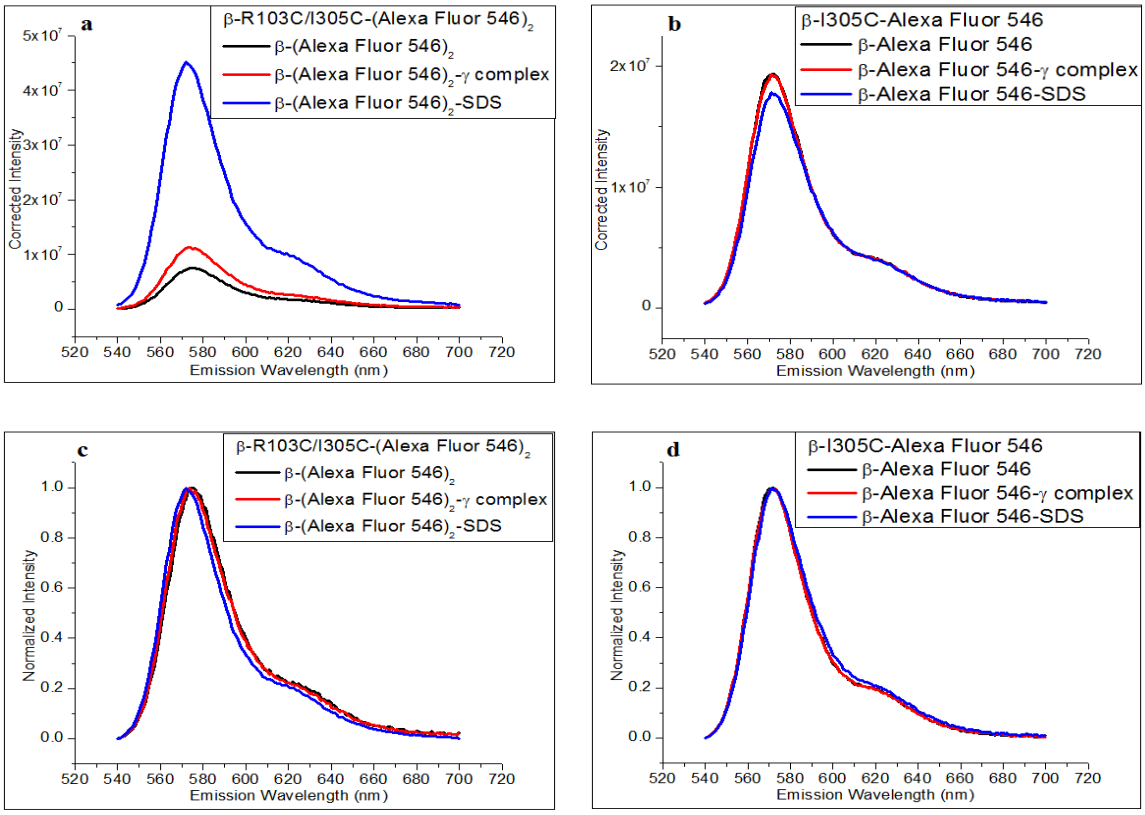

Figure 6.11: Emission scans of β-R103C/I305C-(Alexa Fluor 546)$_2$ (a and c) and β-I305C-Alexa Fluor 546 (b and d). All dye-labeled β concentrations were 0.5 µM. The excitation was fixed at 535 nm, and the emission was scanned from 540 nm to 700 nm. Panels (a) and (b) and panels (c) and (d) show the effects of 2 µM γ complex and 1% SDS detergent on the intensities and shapes of the emission spectra respectively.

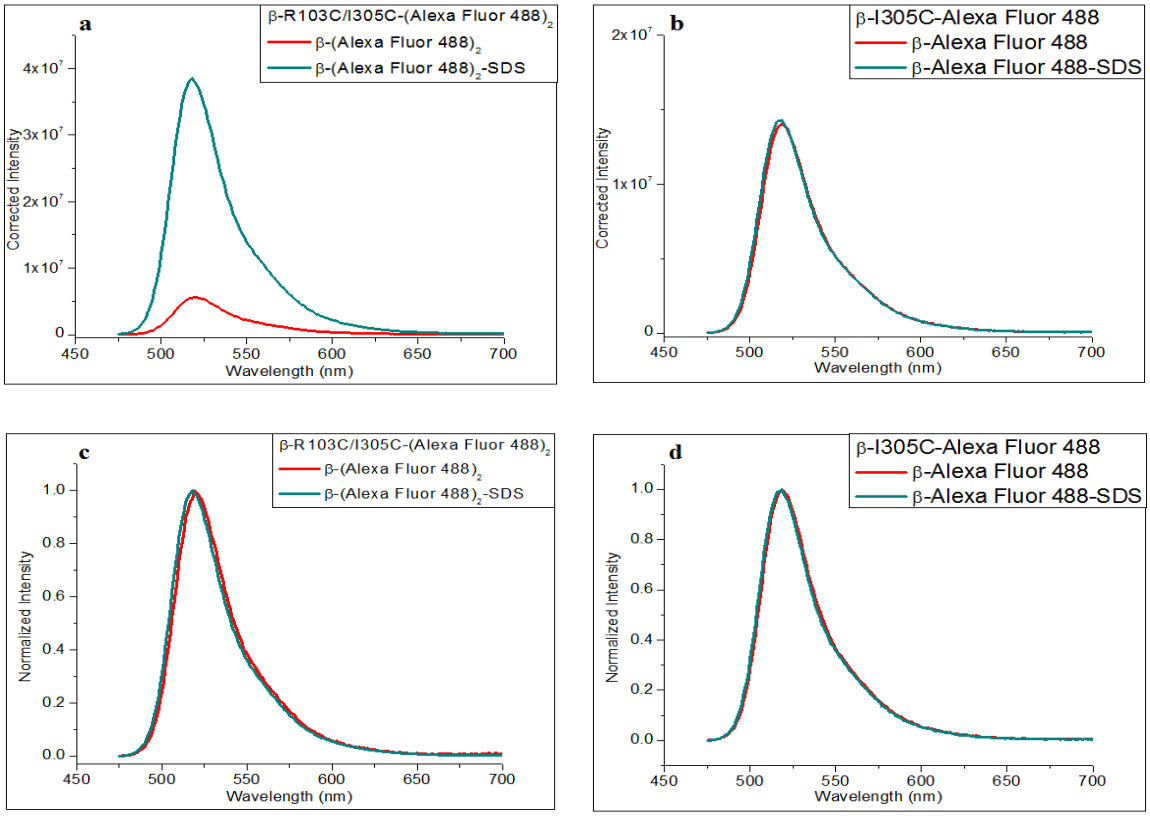

Figure 6.12: Emission scans of β-R103C/I305C-(Alexa Fluor 488)$_2$ (a and c) and β-I305C-Alexa Fluor 488 (b and d). All dye-labeled β were 0.5 μM. The excitation was fixed at 465 nm, and the emission was scanned from 475 nm to 700 nm. Panels (a-b) and (c-d) show the effects of 1% SDS on the intensity and shape of the emission spectra.

6.4 Ensemble Absorbance and Fluorescence Scans with Proteinase K

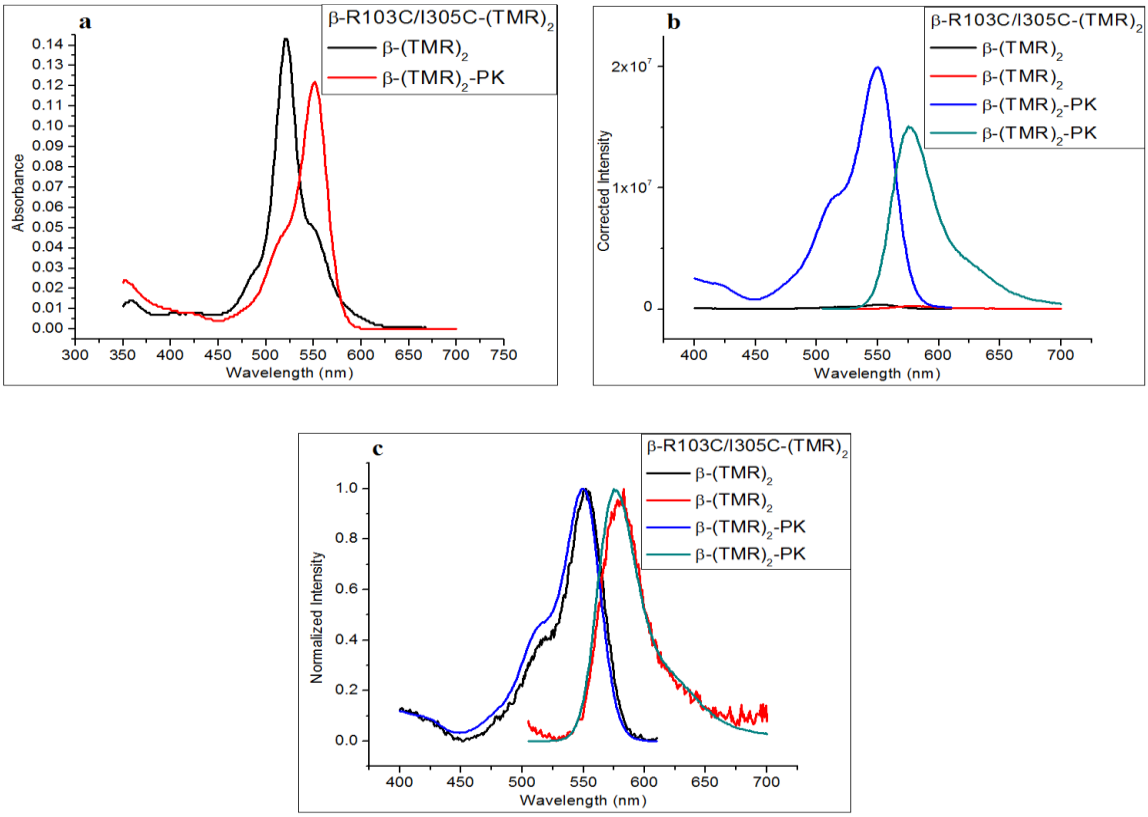

Figure 6.13: Absorbance, excitation, and emission scans of β-R103C/I305C-$(TMR)_2$. All dye-labeled β were 0.5 μM. For the excitation scans, the excitation was scanned from 400 nm to 610 nm, and the emission was collected at 625 nm. For the emission scans, the excitation was fixed at 490 nm, and the emission was scanned from 505 nm to 700 nm. Panel (a) shows the effects of Proteinase K on the absorbance spectrum while panels (b and c) show the effects of Proteinase K on the intensities and shapes of the excitation and emission spectra.

6.5 TCSPC Fitting Parameters of Dye-Labeled β Clamps

Sample	λ_{Ex}(nm)	λ_{Em}(nm)	τ_1 (ns)	τ_2 (ns)	τ_3 (ns)
β-$(TMR)_2$	540	575	2.9 (42%)	1.2 (28%)	0.1 (30%)
β-$(TMR)_2$-γ complex	540	575	2.5 (85%)	0.6 (15%)	
β-$(TMR)_2$-SDS	540	575	3.4 (87%)	0.3 (13%)	
β-TMR	540	575	2.7 (81%)	0.6 (19%)	
β-TMR-γ complex	540	575	2.6 (82%)	0.7 (18%)	
β-TMR-SDS	540	575	3.4 (89%)	0.3 (11%)	
β-$(TMR)_2$	540	575	3.2 (40%)	1.3 (32%)	0.1 (29%)
β-$(TMR)_2$-subunit exchange	540	575	2.7 (81%)	0.9 (19%)	
β-TMR	540	575	2.8 (81%)	0.8 (19%)	
β-TMR-subunit exchange	540	575	2.7 (78%)	0.8 (22%)	
Free TMR maleimide	540	575	2.3 (100%)		
Free TMR maleimide-SDS	540	575	3.3 (83%)	0.9 (17%)	
β-$(TMR)_2$	540	575	2.7 (43%)	0.9 (23%)	0.1 (34%)
β-$(TMR)_2$-PK	540	575	2.6 (93%)	0.2 (7%)	

Table 6.1: Fitting parameters for the TCSPC decays of β-$(TMR)_2$, β-TMR, and free TMR maleimide. Dye-labeled β were 0.5 μM. Subunit exchange: 10 μM unlabeled wt-β was mixed with 0.5 μM dye-labeled β and stored for two days at RT. 2 μM γ complex, 1% SDS, and Proteinase K were also added to the β. Free dye were 1 μM in water. The decays were fitted with exponential terms, as needed to obtain random residuals.

Sample	λ_{Ex} (nm)	λ_{Em} (nm)	τ_1 (ns)	τ_2 (ns)	τ_3 (ns)
β-(TMR C6)$_2$	540	575	2.7 (24%)	0.8 (23%)	0.1 (53%)
β-(TMR C6)$_2$-γ complex	540	575	2.5 (74%)	0.4 (26%)	
β-(TMR C6)$_2$-SDS	540	575	3.4 (80%)	0.3 (20%)	
β-(TMR C6)$_2$	540	575	2.5 (20%)	0.7 (24%)	0.1 (56%)
β-(TMR C6)$_2$-subunit exchange	540	575	3.0 (45%)	1.0 (18%)	0.1 (37%)
β-(TMR C6)$_2$-SDS	540	575	3.4 (81%)	0.4 (19%)	
β-TMR C6	540	575	3.0 (82%)	0.6 (18%)	
β-TMR C6-subunit exchange	540	575	3.1 (84%)	0.7 (16%)	
β-TMR C6-SDS	540	575	3.4 (82%)	0.3 (18%)	
Free TMR C6 maleimide	540	575	2.4 (100%)		
Free TMR C6 maleimide-SDS	540	575	3.4 (83%)	0.2 (17%)	

Table 6.2: Fitting parameters for the TCSPC decays of β-R103C/I305C-(TMR C6)$_2$, β-R103C-TMR C6, and 1 μM free TMR C6 maleimide in water. All dye-labeled β were 0.5 μM. For subunit exchange, 10 μM unlabeled wild-type β was mixed with 0.5 μM dye-labeled β. The samples were stored for two days at room temperature in the dark. 2 μM γ complex and 1% SDS were also added to the dye-labeled β. The TCSPC decays were fitted with one, two, or three exponentials as needed to obtain random residuals.

Sample	λ_{Ex} (nm)	λ_{Em} (nm)	τ_1 (ns)	τ_2 (ns)	τ_3 (ns)
β-$(AF546)_2$	540	575	3.1 (16%)	0.8 (34%)	0.1 (50%)
β-$(AF546)_2$-λ complex	540	575	3.4 (34%)	1.0 (28%)	0.1 (38%)
β-$(AF546)_2$-SDS	540	575	3.8 (93%)	0.6 (7%)	
β-$(AF546)_2$-subunit exchange	540	575	3.7 (36%)	0.9 (25%)	0.1 (39%)
β-AF546	540	575	3.8 (90%)	1.3 (10%)	
β-AF546-γ complex	540	575	3.8 (89%)	1.3 (11%)	
β-AF546-SDS	540	575	3.7 (93%)	0.7 (7%)	
β-AF546-subunit exchange	540	575	3.8 (90%)	1.4 (10%)	
Free AF546 maleimide-water	540	575	3.4 (21%)	1.6 (41%)	0.2 (38%)
Free AF546 maleimide-SDS	540	575	3.7 (82%)	1.1 (18%)	
Free AF546 maleimide-D_2O	540	575	3.5 (32%)	1.5 (32%)	0.2 (36%)
Free AF546 maleimide-ethanol	540	575	3.6 (87%)	0.8 (13%)	

Table 6.3: Fitting parameters for the TCSPC decays of β-R103C/I305C-(Alexa Fluor 546)$_2$, β-I305C-Alexa Fluor 546, and free Alexa Fluor 546 maleimide. All dye-labeled β concentrations were 0.5 μM. For subunit exchange, a twenty-fold excess of unlabeled wild-type β (10 μM) was mixed with 0.5 μM dye-labeled β. The subunit-exchanged samples were stored for two days at room temperature in the dark. 2 μM γ complex and 1% SDS were also added to the dye-labeled β. The TCSPC decays were fitted with one, two or three exponential terms, as needed to obtain random residuals.

Sample	λ_{Ex} (nm)	λ_{Em} (nm)	τ_1 (ns)	τ_2 (ns)	τ_3 (ns)
Free TMR maleimide	540	590	2.3 (91%)	1.0 (9%)	
Free TMR maleimide-DTT	540	590	2.3 (100%)		
Free TMR C6 maleimide	540	590	2.4 (100%)		
Free TMR C6 maleimide-DTT	540	590	2.4 (100%)		
Free AF546 maleimide	540	570	3.1 (32%)	1.3 (33%)	0.2 (35%)
Free AF546 maleimide-DTT	540	570	3.8 (100%)		
Free AF488 maleimide	500	540	4.0 (81%)	1.7 (19%)	
Free AF488 maleimide-DTT	500	540	4.0 (100%)		

Table 6.4: Fitting parameters for the TCSPC decays of 1 µM free TMR maleimide, TMR C6 maleimide, Alexa Fluor546 maleimide, and Alexa Fluor 488 maleimide in water before and after the addition of excess 5 mM DTT. The TCSPC decays were fitted with one, two or three exponential terms, as needed to obtain random residuals.

Sample	λ_{Ex} (nm)	λ_{Em} (nm)	τ_1 (ns)	τ_2 (ns)	τ_3 (ns)
β-$(AF488)_2$	500	540	3.2 (23%)	0.8 (12%)	0.1 (65%)
β-$(AF488)_2$-γ complex	500	540	3.7 (63%)	1.5 (8%)	0.1 (29%)
β-$(AF488)_2$-SDS	500	540	3.9 (95%)	1.0 (5%)	
β-AF488	500	540	3.9 (89%)	1.1 (11%)	
β-AF488-γ complex	500	540	3.8 (89%)	1.4 (11%)	
β-AF488-SDS	500	540	3.9 (90%)	1.6 (10%)	
β-$(AF488)_2$	500	540	3.3 (21%)	1.1 (13%)	0.1 (67%)
β-$(AF488)_2$-subunit exchange	500	540	4.0 (48%)	1.7 (11%)	0.1 (41%)
β-$(AF488)_2$-SDS	500	540	4.0 (90%)	2.0 (10%)	
β-AF488	500	540	3.9 (76%)	1.9 (24%)	
β-AF488-subunit exchange	500	540	3.9 (75%)	1.9 (25%)	
β-AF488-SDS	500	540	3.8 (75%)	2.0 (25%)	
Free AF488 maleimide	500	540	4.0 (76%)	1.6 (24%)	
Free AF488 maleimide-SDS	500	540	3.9 (78%)	1.6 (22%)	

Table 6.5: Fitting parameters for the TCSPC decays of β-R103C/I305C-(Alexa Fluor 488)$_2$, β-I305C-Alexa Fluor 488, and free Alexa Fluor 488 maleimide. All dye-labeled β were 0.5 μM. For subunit exchange, 10 μM unlabeled wild-type β was mixed with dye-labeled β. 2 μM γ complex and 1% SDS were added to the dye-labeled β. The TCSPC decays were fitted with one, two, or three exponentials as needed to obtain random residuals.

CONCLUSIONS

This thesis focused on the efforts to understand the photophysics of BODIPY dyes and rhodamine dyes when they are in close proximity to each other. The ability to use these dyes in biological applications relies on an understanding of the fundamental photophysics of these dyes. Chapter 3 detailed a spectroscopic investigation of the photophysics of BODIPY dyes noncovalently encapsulated in different micellar environments. Amphiphilic polymers with a hydrophobic character and a low Critical Micelle Concentration (CMC) adequately shielded the BODIPY dyes from the aqueous medium even under moderate dye-loading conditions. Moderate dye loading conditions did not result in ground-state dimerization, and only fluorescence lifetimes and brightnesses were affected. Amphiphilic polymers with a hydrophilic character and a high CMC were unable to shield the BODIPY dyes from the aqueous medium with concomitant ground-state dimerization and quenching of the fluorescence intensity, lifetime, and brightnesses even under low dye loading conditions. Chapter 5 detailed a spectroscopic investigation of interchromophoric interactions at the doubly-labeled interfaces of *E. coli* DNA Processivity β clamps for four rhodamine dyes: TMR, TMR C6, Alexa Fluor 546, and Alexa Fluor 488. It was found that both TMR and TMR C6 readily formed H-dimers (static quenching) at the doubly-labeled interfaces, but the longer linker TMR C6 displayed a larger degree of dynamic quenching manifesting as instantaneous depolarizations in the anisotropy decays and fluorescence lifetime shortenings indicating homo-FRET. Alexa Fluor 546 might have displayed a small degree of static quenching in the absorbance and excitation scans suggesting dimers intermediate between H-dimers and J-dimers, but Alexa Fluor 488 displayed no signs of

ground-state dimerization in the absorbance scans. Both Alexa Fluor 546 and Alexa Fluor 488 displayed larger degrees of dynamic quenching manifesting as instantaneous depolarizations in the anisotropy decays and fluorescence lifetime shortenings indicating homo-FRET. It should be noted that the three dyes with longer linkers (TMR C6, Alexa Fluor 546, and Alexa Fluor 488) displayed a larger degree of dynamic quenching suggesting that linker length might be one of many important variables that determine the interchromophoric interactions.

REFERENCES

1. Rice, S.A. and G.A. Kenney-Wallace, *Time-resolved fluorescence depolarization studies of rotational relaxation in viscous media.* Chemical Physics, 1980. **47**(2): p. 161-170.

2. Fleming, G.R., J.M. Morris, and G.W. Robinson, *Direct observation of rotational diffusion by picosecond spectroscopy.* Chemical Physics, 1976. **17**(1): p. 91-100.

3. Magde, D., E. Elson, and W.W. Webb, *Thermodynamic fluctuations in a reacting system measurement by fluorescence correlation spectroscopy.* Physical Review Letters, 1972. **29**(11): p. 705-708.

4. Burstyn, H.C. and J.V. Sengers, *Time dependence of critical concentration fluctuations in a binary liquid.* Physical Review A, 1983. **27**(2): p. 1071-1085.

5. Zhu, et al., *Scaling of transient hydrodynamic interactions in concentrated suspensions.* Physical review letters, 1992. **68**(16): p. 2559.

6. Jorg, E., et al., *Art and Artefacts of Fluorescence Correlation Spectroscopy.* Current Pharmaceutical Biotechnology, 2004. **5**(2): p. 155-161.

7. Gregor, I., D. Patra, and J. Enderlein, *Optical saturation in fluorescence correlation spectroscopy under continuous-wave and pulsed excitation.* Chemphyschem : a European journal of chemical physics and physical chemistry, 2005. **6**(1): p. 164.

8. Sauer, M., J. Hofkens, and J.Ã. Enderlein, *Handbook of Fluorescence Spectroscopy and Imaging: From Ensemble to Single Molecules*. 2010: Wiley.

9. Arbeloa, I.L. and P.R. Ojeda, *Molecular forms of rhodamine B.* Chemical Physics Letters, 1981. **79**(2): p. 347-350.

10. Arbeloa, I.L. and K.K. Rohatgi-Mukherjee, *Solvent effect on photophysics of the molecular forms of rhodamine B. Solvation models and spectroscopic parameters.* Chemical Physics Letters, 1986. **128**(5): p. 474-479.

11. López Arbeloa, F., I.U. Aguirresacona, and I.L. Arbeloa, *Influence of the molecular structure and the nature of the solvent on the absorption and fluorescence characteristics of rhodamines.* Chemical Physics, 1989. **130**(1): p. 371-378.

12. López Arbeloa, F., et al., *Photophysics of rhodamines. Molecular structure and solvent effects.* Journal of Physical Chemistry, 1991. **95**(6): p. 2203-2208.

13. Sauer, M., et al., *New fluorescent labels for time-resolved detection of biomolecules.* Journal of Fluorescence, 1993. **3**(3): p. 131-139.

14. Panchuk-Voloshina, N., et al., *Alexa Dyes, a Series of New Fluorescent Dyes that Yield Exceptionally Bright, Photostable Conjugates.* Journal of Histochemistry & Cytochemistry, 1999. **47**(9): p. 1179-1188.

15. Rohatgi, K.K. and G.S. Singhal, *THE INFLUENCE OF UREA ON THE FLUORESCENCE OF AQUEOUS DYE SOLUTIONS.* The Journal of Physical Chemistry, 1963. **67**(12): p. 2844-2846.

16. Rohatgi, K.K. and G.S. Singhal, *Nature of bonding in dye aggregates.* Journal of Physical Chemistry, 1966. **70**(6): p. 1695-1701.

17. Selwyn, J.E. and J.I. Steinfeld, *Aggregation equilibria of xanthene dyes.* Journal of Physical Chemistry, 1972. **76**(5): p. 762-774.

18. López Arbeloa, I. and P. Ruiz Ojeda, *Dimeric states of rhodamine B.* Chemical Physics Letters, 1982. **87**(6): p. 556-560.

19. Arbeloa, F.L., et al., *Aggregate formation of rhodamine 6G in aqueous solution.* Journal of the Chemical Society, Faraday Transactions 2: Molecular and Chemical Physics, 1982. **78**(7): p. 989-994.

20. Valdesaguilera, O. and D.C. Neckers, *AGGREGATION PHENOMENA IN XANTHENE DYES*, in *Accounts Chem. Res.* 1989. p. 171-177.

21. Arbeloa, F.L., et al., *Self-association of the molecular forms of Rhodamine 19. Solvent effect.* Spectrochimica Acta Part A: Molecular Spectroscopy, 1989. **45**(12): p. 1201-1206.

22. Davydov, A.S., *THE THEORY OF MOLECULAR EXCITONS.* Soviet Physics Uspekhi, 1964. **7**(2): p. 145.

23. Kasha, M., *ENERGY TRANSFER MECHANISMS AND THE MOLECULAR EXCITON MODEL FOR MOLECULAR AGGREGATES.* Radiation research, 1963. **20**: p. 55-70.

24. Kasha, M., H.R. Rawls, and M. Ashraf El-Bayoumi, *The exciton model in molecular spectroscopy*, in *Pure and Applied Chemistry*. 1965. p. 371.

25. López Arbeloa, F., P. Ruiz Ojeda, and I. López Arbeloa, *The fluorescence quenching mechanisms of Rhodamine 6G in concentrated ethanolic solution.* Journal of Photochemistry & Photobiology, A: Chemistry, 1988. **45**(3): p. 313-323.

26. Arbeloa, F., P. Ojeda, and I. Arbeloa, *FLUORESCENCE SELF-QUENCHING OF THE MOLECULAR-FORMS OF RHODAMINE-B IN AQUEOUS AND ETHANOLIC SOLUTIONS.* J. Lumines., 1989. **44**(1-2): p. 105-112.

27. Kemnitz, K. and K. Yoshihara, *Entropy-driven dimerization of xanthene dyes in nonpolar solution and temperature-dependent fluorescence decay of dimers.* Journal of Physical Chemistry, 1991. **95**(16): p. 6095-6104.

28. Hernando Campos, J., et al., *Excitonic Behavior of Rhodamine Dimers: A Single-Molecule Study.* Journal of physical chemistry A, 2003. **107**(1): p. 43-52.

29. Packard, B.Z., et al., *Profluorescent protease substrates: intramolecular dimers described by the exciton model.* Proceedings of the National Academy of Sciences of the United States of America, 1996. **93**(21): p. 11640.

30. Blackman, M.J., et al., *Structural and biochemical characterization of a fluorogenic rhodamine-labeled malarial protease substrate.* Biochemistry, 2002. **41**(40): p. 12244.

31. Gakamsky, D.M., et al., *Photophysical Analysis of Class I Major Histocompatibility Complex Protein Assembly Using a Xanthene-Derivatized β 2-Microglobulin.* Biophysical Journal, 1999. **76**(3): p. 1552-1560.

32. Ogawa, M., et al., *H-type dimer formation of fluorophores: A mechanism for activatable, in vivo optical molecular imaging.* ACS Chemical Biology, 2009. **4**(7): p. 535-546.

33. Binder, J.K., et al., *Intrinsic stability and oligomerization dynamics of DNA processivity clamps.* Nucleic acids research, 2014. **42**(10): p. 6476.

34. Purohit, A., et al., *Electrostatic Interactions at the Dimer Interface Stabilize the E. coli β Sliding Clamp.* Biophysical Journal, 2017. **113**(4): p. 794-804.

35. Pavlopoulos, T., et al., *LASER ACTION FROM 2,6,8-POSITION TRISUBSTITUTED 1,3,5,7-TETRAMETHYLPYRROMETHENE-BF2 COMPLEXES .1.* Appl. Optics, 1990. **29**(27): p. 3885-3886.

36. Karolin, J., et al., *Fluorescence and Absorption Spectroscopic Properties of Dipyrrometheneboron Difluoride (BODIPY) Derivatives in Liquids, Lipid Membranes, and Proteins.* Journal of the American Chemical Society, 1994. **116**(17): p. 7801-7806.

37. López Arbeloa, F., T. López Arbeloa, and I. López Arbeloa, *Electronic spectroscopy of pyrromethene 546.* Journal of Photochemistry and Photobiology A: Chemistry, 1999. **121**(3): p. 177-182.

38. Arbeloa, T.L., et al., *Correlations between photophysics and lasing properties of dipyrromethene–BF 2 dyes in solution.* Chemical Physics Letters, 1999. **299**(3): p. 315-321.

39. Feng, L., et al., *Eight-position substitution effects on laser action of the 1,3,5,7-tetramethyl-2,6-diethyl pyrromethene-BF_2 complexes.* Journal of the Optical Society of America B, 2001. **18**(12): p. 1841-1845.

40. Rohr, H., et al., *Proton- and redox-controlled switching of photo- and electrochemiluminescence in thiophenyl-substituted boron-dipyrromethene dyes*, in *Chem.-Eur. J.* 2006. p. 689-700.

41. Mula, S., et al., *Design and development of a new pyrromethene dye with improved photostability and lasing efficiency: theoretical rationalization of photophysical and photochemical properties.* Journal of Organic Chemistry, 2008. **73**(6): p. 2146-2154.

42. Chaudhuri, T., et al., *Photophysical properties of the 8-phenyl analogue of PM567: A theoretical rationalization.* Spectrochimica Acta Part A: Molecular and Biomolecular Spectroscopy, 2010. **75**(2): p. 739-744.

43. Hecht, M., W. Kraus, and K. Rurack, *A highly fluorescent pH sensing membrane for the alkaline pH range incorporating a BODIPY dye.* Analyst, 2012. **138**(1): p. 325-332.

44. Jiao, L., et al., *Regioselective stepwise bromination of boron dipyrromethene (BODIPY) dyes.* The Journal of organic chemistry, 2011. **76**(24): p. 9988.

45. Bahaidarah, E., et al., *Fluorescent molecular rotors based on the BODIPY motif: effect of remote substituents.* Photochem. Photobiol. Sci., 2014. **13**(10): p. 1397-1401.

46. Mikhalyov, I., et al., *Electronic ground and excited state properties of dipyrrometheneboron difluoride (BODIPY): Dimers with application to biosciences.* Phys. Chem. Chem. Phys., 2002. **4**(22): p. 5663-5670.

47. Marushchak, D., et al., *Pyrromethene dyes (BODIPY) can form ground state homo and hetero dimers: Photophysics and spectral properties.* Spectrochimica Acta Part A: Molecular and Biomolecular Spectroscopy, 2006. **65**(1): p. 113-122.

48. Bell, N.C., et al., *Dye Encapsulation in Polynorbornene Micelles.* Langmuir : the ACS journal of surfaces and colloids, 2015. **31**(35): p. 9707.

49. Okhapkin, I.M., E.E. Makhaeva, and A.R. Khokhlov, *Water Solutions of Amphiphilic Polymers: Nanostructure Formation and Possibilities for Catalysis*, in *Conformation-Dependent Design of Sequences in Copolymers I*, A.R. Khokhlov, Editor. 2006, Springer Berlin Heidelberg: Berlin, Heidelberg. p. 177-210.

50. Kale, T.S., et al., *Supramolecular assemblies of amphiphilic homopolymers.* Langmuir : the ACS journal of surfaces and colloids, 2009. **25**(17): p. 9660.

51. Moughton, A.O., M.A. Hillmyer, and T.P. Lodge, *Multicompartment block polymer micelles.* Macromolecules, 2012. **45**(1): p. 2-19.

52. Owen, S.C., D.P.Y. Chan, and M.S. Shoichet, *Polymeric micelle stability.* Nano Today, 2012. **7**(1): p. 53-65.

53. Wang, Y. and S.M. Grayson, *Approaches for the preparation of non-linear amphiphilic polymers and their applications to drug delivery.* Advanced Drug Delivery Reviews, 2012. **64**(9): p. 852-865.

54. Nicolas, J., et al., *Design, functionalization strategies and biomedical applications of targeted biodegradable/biocompatible polymer-based nanocarriers for drug delivery.* Chem. Soc. Rev., 2013. **42**(3): p. 1147-1235.

55. Zhuang, J., et al., *Multi-stimuli responsive macromolecules and their assemblies.* Chem. Soc. Rev., 2013. **42**(17): p. 7421-7435.

56. Makino, A., *Morphology control of molecular assemblies prepared from bio-based amphiphilic polymers with a helical hydrophobic unit and application as nanocarriers for contrast agents and/or drug delivery.* Polymer Journal, 2014. **46**: p. 783.

57. Swaminathan, S., et al., *Photoresponsive polymer nanocarriers with multifunctional cargo.* Chem. Soc. Rev., 2014. **43**(12): p. 4167-4178.

58. Hu, Y., et al., *WATER-SOLUBLE COPOLYMERS .62. NONRADIATIVE ENERGY-TRANSFER STUDIES OF PH-RESPONSIVE AND SALT-RESPONSIVE ASSOCIATIONS IN HYDROPHOBICALLY-MODIFIED, HYDROLYZED MALEIC ANHYDRIDE-ETHYL VINYL ETHER COPOLYMERS.* Macromolecules, 1995. **28**(21): p. 7100-7106.

59. Yoo, S.I., et al., *Controlled Light Emission by Nanoencapsulation of Fluorophores in Thin Films of Diblock Copolymer Micelles.* Advanced Materials, 2007. **19**(12): p. 1594-1596.

60. Yoo, S.I., et al., *Enhancement and Concurrence of Emissions from Multiple Fluorophores in a Single Emitting Layer of Micellar Nanostructures.* Advanced Functional Materials, 2008. **18**(19): p. 2984-2989.

61. Chen, H., et al., *Fast release of lipophilic agents from circulating PEG-PDLLA micelles revealed by in vivo forster resonance energy transfer imaging.* Langmuir : the ACS journal of surfaces and colloids, 2008. **24**(10): p. 5213.

62. Njikang, G.N., M. Gauthier, and J. Li, *Sustained release properties of arborescent polystyrene-graft-poly(2-vinylpyridine) copolymers.* Polymer, 2008. **49**(25): p. 5474-5481.

63. Hongtao, C., et al., *Release of hydrophobic molecules from polymer micelles into cell membranes revealed by Förster resonance energy transfer imaging.* Proceedings of the National Academy of Sciences, 2008. **105**(18): p. 6596.

64. Wu, W.C., et al., *Enhancement of Aggregation-Induced Emission in Dye-Encapsulating Polymeric Micelles for Bioimaging.* Advanced Functional Materials, 2010. **20**(9): p. 1413-1423.

65. Jiwpanich, S., et al., *Noncovalent encapsulation stabilities in supramolecular nanoassemblies.* Journal of the American Chemical Society, 2010. **132**(31): p. 10683.

66. Ryu, J.-H., et al., *Self-cross-linked polymer nanogels: a versatile nanoscopic drug delivery platform.* Journal of the American Chemical Society, 2010. **132**(48): p. 17227.

67. Chen, K.-J., et al., *Intracellularly monitoring/imaging the release of doxorubicin from pH-responsive nanoparticles using Förster resonance energy transfer.* Biomaterials, 2011. **32**(10): p. 2586-2592.

68. Wang, R., et al., *Enhanced white-light emission from multiple fluorophores encapsulated in a single layer of diblock copolymer micelles.* Chem. Commun., 2011. **47**(10): p. 2787-2789.

69. Lu, J., S.C. Owen, and M.S. Shoichet, *Stability of Self-Assembled Polymeric Micelles in Serum.* Macromolecules, 2011. **44**(15): p. 6002-6008.

70. Hu, P. and N. Tirelli, *Inter-micellar dynamics in block copolymer micelles: FRET experiments of macroamphiphile and payload exchange.* Reactive and Functional Polymers, 2011. **71**(3): p. 303-314.

71. McDonald, T.O., et al., *Multicomponent Organic Nanoparticles for Fluorescence Studies in Biological Systems.* Advanced Functional Materials, 2012. **22**(12): p. 2469-2478.

72. Li, Y., et al., *Probing of the Assembly Structure and Dynamics within Nanoparticles during Interaction with Blood Proteins.* ACS Nano, 2012. **6**(11): p. 9485-9495-9485-9495.

73. Li, Y., et al., *Well-Defined, Reversible Boronate Crosslinked Nanocarriers for Targeted Drug Delivery in Response to Acidic pH Values and cis-Diols.* Angewandte Chemie International Edition, 2012. **51**(12): p. 2864-2869.

74. Bickerton, S., S. Jiwpanich, and S. Thayumanavan, *Interconnected roles of scaffold hydrophobicity, drug loading, and encapsulation stability in polymeric nanocarriers.* Molecular pharmaceutics, 2012. **9**(12): p. 3569.

75. Wagh, A., S. Qian, and B. Law, *Development of Biocompatible Polymeric Nanoparticles for in Vivo NIR and FRET Imaging.* Bioconjugate Chemistry, 2012. **23**(5): p. 981.

76. Javali, N.M., et al., *Fatty acid-RGD peptide amphiphile micelles as potential paclitaxel delivery carriers to $\alpha(v)\beta_3$ integrin overexpressing tumors.* Pharmaceutical research, 2012. **29**(12): p. 3347.

77. Klymchenko, A.S., et al., *Highly lipophilic fluorescent dyes in nano-emulsions: towards bright non-leaking nano-droplets.* RSC Adv., 2012. **2**(31): p. 11876-11886.

78. Lee, S.-Y., et al., *FRET imaging reveals different cellular entry routes of self-assembled and disulfide bonded polymeric micelles.* Molecular pharmaceutics, 2013. **10**(9): p. 3497.

79. Yildiz, I., et al., *Supramolecular strategies to construct biocompatible and photoswitchable fluorescent assemblies.(Report).* Journal of the American Chemical Society, 2011. **133**(4): p. 871-879.

80. Cusido, J., et al., *Fast Fluorescence Switching within Hydrophilic Supramolecular Assemblies.* Chemistry – A European Journal, 2012. **18**(33): p. 10399-10407.

81. Deniz, E., et al., *Photoactivatable Fluorophores for Super-Resolution Imaging Based on Oxazine Auxochromes.* The Journal of Physical Chemistry C, 2012. **116**(10): p. 6058-6068.

82. Swaminathan, S., et al., *Fluorescence photoactivation by intermolecular proton transfer.(Report).* Journal of Physical Chemistry A, 2012. **116**(40): p. 9928-9933.

83. Petriella, M., et al., *Superresolution Imaging with Switchable Fluorophores Based on Oxazine Auxochromes.* Photochemistry and Photobiology, 2013. **89**(6): p. 1391-1398.

84. Swaminathan, S., et al., *Intracellular guest exchange between dynamic supramolecular hosts.(Report).* Journal of the American Chemical Society, 2014. **136**(22): p. 7907-7913.

85. Zhang, Y., et al., *Photoactivatable BODIPYs designed to monitor the dynamics of supramolecular nanocarriers.* Journal of the American Chemical Society, 2015. **137**(14): p. 4709.

86. Swaminathan, S., et al., *Supramolecular nanoreactors for intracellular singlet-oxygen sensitization.* Nanoscale, 2015. **7**(33): p. 14071-14079.

87. Thapaliya, E.R., et al., *Energy-Transfer Schemes To Probe Fluorescent Nanocarriers and Their Emissive Cargo.* Langmuir : the ACS journal of surfaces and colloids, 2015. **31**(35): p. 9557.

88. Ragab, S.S., et al., *Synthesis in living cells with the assistance of supramolecular nanocarriers.* RSC Adv., 2016. **6**(39): p. 32441-32445.

89. Zhang, Y., et al., *Supramolecular delivery of fluorescent probes in developing embryos.* RSC Adv., 2016. **6**(76): p. 72756-72760.

90. *PDI and I_S quantify the widths of the distributions of the molecular weight of the individual macromolecules and the hydrodynamic diameter of the corresponding nanoparticles respectively. The former parameter is the ratio between the weight-average molecular weight and M_n determined by GPC (ref. 91). The latter parameter is the square root of the ratio between the standard deviation and D_H (ref. 92).*

91. Stepto, R.F.T., *Dispersity in polymer science: (IUPAC Recommendations 2009).(INTERNATIONAL UNION OF PURE AND APPLIED CHEMISTRY: POLYMER DIVISION SUBCOMMITTEE ON POLYMER TERMINOLOGY)(Report).* Pure and Applied Chemistry, 2009. **81**(2): p. 351.

92. Koppel, D.E., *Analysis of Macromolecular Polydispersity in Intensity Correlation Spectroscopy: The Method of Cumulants.* The Journal of Chemical Physics, 1972. **57**(11): p. 4814-4820.

93. *The values of N_G are the ratios between the molar concentrations of the molecular guests, measured by absorption spectroscopy, and those of the supramolecular hosts, determined from the mass of corresponding polymer. As a result, these estimates assume that the molecular guests are evenly distributed across the entire population of supramolecular hosts. Alternatively, groups of guests can aggregate, when exposed to the aqueous solution, and the resulting aggregates can be encapsulated within a fraction of the nanocarriers, while the rest of the supramolecular containers remains empty. FCS and lifetime measurements are indicative of significant interchromophoric interactions and, therefore, are consistent with the latter interpretation.*

94. *Compound 8 was prepared in one step from known precursors (Figure 4.4). Its absorption and emission spectra (Figure 4.5) show the characteristic bands of the*

BODIPY chromophore with negligible solvent dependence. ϕ is 0.50 in THF and 0.58 in PBS (Table 3.2).

95. *A similar analysis (Figure 4.8) indicates K_{SV} to be 20 M^{-1} (Table 3.2) for 8 in the absence of macromolecules.*

96. Thompson, N.L., *Fluorescence Correlation Spectroscopy*, in *Topics in Fluorescence Spectroscopy: Techniques*, J.R. Lakowicz, Editor. 1999, Springer US: Boston, MA. p. 337-378.

97. Müller, J.D., Y. Chen, and E. Gratton, *Fluorescence correlation spectroscopy.* Methods in enzymology, 2003. **361**: p. 69.

98. Pieiro, L., et al., *Dye exchange in micellar solutions. Quantitative analysis of bulk and single molecule fluorescence titrations.* Soft Matter, 2013. **9**(45): p. 10779-10790.

99. Yu, G., et al., *Highly sensitive fluorescence probes for nitric oxide based on boron dipyrromethane chromophore-rational design of potentially useful bioimaging fluorescence probe.* Journal of the American Chemical Society, 2004. **126**(10): p. 3357.

100. Tomasulo, M., et al., *Photoswitchable Fluorescent Assemblies Based on Hydrophilic BODIPY−Spiropyran Conjugates †.* The Journal of Physical Chemistry C, 2008. **112**(21): p. 8038-8045.

101. Sandler, S.R., et al., *Polymer Synthesis and Characterization: A Laboratory Manual*. 1998: Elsevier Science.

102. Lakowicz, J.R., *Principles of Fluorescence Spectroscopy*. 3rd ed.. ed, ed. J.R. Lakowicz. 2006: Boston, MA : Springer US.

103. Chakraborty, M., et al., *Protein Oligomerization Monitored by Fluorescence Fluctuation Spectroscopy: Self-Assembly of Rubisco Activase.* Biophysical Journal, 2012. **103**(5): p. 949-958.

104. Ciuba, M.A. and M. Levitus, *Manganese-Induced Triplet Blinking and Photobleaching of Single Molecule Cyanine Dyes.* ChemPhysChem, 2013. **14**(15): p. 3495-3502.

105. Gendron, P.O., F. Avaltroni, and K. Wilkinson, *Diffusion Coefficients of Several Rhodamine Derivatives as Determined by Pulsed Field Gradient–Nuclear Magnetic Resonance and Fluorescence Correlation Spectroscopy.* Journal of Fluorescence, 2008. **18**(6): p. 1093-1101.

106. Müller, C.B., et al., *Precise measurement of diffusion by multi-color dual-focus fluorescence correlation spectroscopy.* EPL (Europhysics Letters), 2008. **83**(4): p. 46001.

107. Hedglin, M., R. Kumar, and S.J. Benkovic, *Replication clamps and clamp loaders.* Cold Spring Harbor Perspectives in Biology, 2013. **5**(4): p. 1-19.

108. Kong, X.-P., et al., *Three-dimensional structure of the β subunit of E. coli DNA polymerase III holoenzyme: A sliding DNA clamp.* Cell, 1992. **69**(3): p. 425-437.

109. Oakley, A.J., et al., *Flexibility revealed by the 1.85 Å crystal structure of the β sliding-clamp subunit of Escherichia coli DNA polymerase III.* Acta Crystallographica Section D, 2003. **59**(7): p. 1192-1199.

110. Turner, J., et al., *The internal workings of a DNA polymerase clamp-loading machine.* EMBO Journal, 1999. **18**(3): p. 771-783.

111. Johanson, K.O., T.E. Haynes, and C.S. McHenry, *Chemical characterization and purification of the β subunit of the DNA polymerase III holoenzyme from an overproducing strain.* Journal of Biological Chemistry, 1986. **261**(25): p. 11460-11465.

112. Anderson, S.G., et al., *Temporal correlation of DNA binding, ATP hydrolysis, and clamp release in the clamp loading reaction catalyzed by the Escherichia coli γ complex.* Biochemistry, 2009. **48**(36): p. 8516-8527.

113. Paschall, C.O., et al., *The Escherichia coli clamp loader can actively pry open the β-sliding clamp.* The Journal of biological chemistry, 2011. **286**(49): p. 42704.

114. Maki, S. and A. Kornberg, *DNA polymerase III holoenzyme of Escherichia coli. I. Purification and distinctive functions of subunits τ and γ, the dnaZX gene products.* Journal of Biological Chemistry, 1988. **263**(14): p. 6547-6554.

115. Tang, S., et al., *Structural Implications on the Properties of Self-Assembling Supramolecular Hosts for Fluorescent Guests.* Langmuir : the ACS journal of surfaces and colloids, 2016. **32**(34): p. 8676.

116. Conroy, E., et al., *Self-Quenching, Dimerization, and Homo-FRET in Hetero-FRET Assemblies with Quantum Dot Donors and Multiple Dye Acceptors.* J. Phys. Chem. C, 2016. **120**(31): p. 17817-17828.

117. *Alexa Fluor 610-X NHS Ester (Succinimidyl Ester) - Thermo Fisher Scientific*. 2018; Available from: https://www.thermofisher.com/order/catalog/product/A30050.

118. Agnew, B., K. Gee, and T. NYBERG, *Labeling and detection of post translationally modified proteins*. 2007, Google Patents.

119. Papenhuijzen, J. and A.J.W.O. Visser, *Simulation of convoluted and exact emission anisotropy decay profiles.* Biophysical Chemistry, 1983. **17**(1): p. 57-65.

120. Visser, N.V., et al., *Tryptophan-Tryptophan Energy Migration as a Tool to Follow Apoflavodoxin Folding.* Biophysical Journal, 2008. **95**(5): p. 2462-2469.

121. Nunthaboot, N., et al., *Molecular dynamics simulation of energy migration between tryptophan residues in apoflavodoxin.* RSC Adv., 2014. **4**(59): p. 31443-31451.

122. Koushik, S.V. and S.S. Vogel, *Energy migration alters the fluorescence lifetime of Cerulean: implications for fluorescence lifetime imaging Forster resonance energy transfer measurements.* Journal of biomedical optics, 2008. **13**(3): p. 031204-031204.

123. Matsumoto, T., et al., *A thiol-reactive fluorescence probe based on donor-excited photoinduced electron transfer: key role of ortho substitution.* Organic letters, 2007. **9**(17): p. 3375.

124. Melo, A.M., et al., *Exploring homo-FRET to quantify the oligomer stoichiometry of membrane-bound proteins involved in a cooperative partition equilibrium.* Physical Chemistry Chemical Physics, 2014. **16**(34): p. 18105-18117.

125. Yan, Y. and G. Marriott, *Analysis of protein interactions using fluorescence technologies.* Current Opinion in Chemical Biology, 2003. **7**(5): p. 635-640.

126. Ghukasyan, V., et al. *Fluorescence lifetime dynamics of enhanced green fluorescent protein in protein aggregates with expanded polyglutamine*. 2010. SPIE.

127. Rafal, L., et al., *Single Molecule Studies of Multiple-Fluorophore Labeled Antibodies. Effect of Homo-FRET on the Number of Photons Available Before Photobleaching.* Current Pharmaceutical Biotechnology, 2008. **9**(5): p. 411-420.

128. Nicoli, F., et al., *Directional Photonic Wire Mediated by Homo-Förster Resonance Energy Transfer on a DNA Origami Platform.* ACS Nano, 2017. **11**(11): p. 11264-11272.

129. *Tetramethylrhodamine-5-Maleimide, single isomer - Thermo Fisher Scientific*. 2018; Available from: https://www.thermofisher.com/order/catalog/product/T6027.

130. *5-TAMRA-C6-Maleimide-AAT Bio*. 2018; Available from: https://www.aatbio.com/products/5-tamra-c6-maleimide?unit=424.

131. *Alexa Fluor 546 C5 Maleimide - Thermo Fisher Scientific*. 2018; Available from: https://www.thermofisher.com/order/catalog/product/A10258.

132. *Alexa Fluor 488 C5 Maleimide - Thermo Fisher Scientific*. 2018; Available from: https://www.thermofisher.com/order/catalog/product/A10254.

APPENDIX A

"REPRINTED (ADAPTED) WITH PERMISSION FROM STRUCTURAL IMPLICATIONS ON THE PROPERTIES OF SELF-ASSEMBLING SUPRAMOLECULAR HOSTS FOR FLUORESCENT GUESTS.

SICHENG TANG, BRYAN DONAPHON, MARCIA LEVITUS, AND FRANÇISCO M. RAYMO.

LANGMUIR **2016** *32* (34), 8676-8687.

DOI: 10.1021/ACS.LANGMUIR.6B01549.

Copyright Clearance Center RightsLink®

Home | Create Account | Help

ACS Publications
Most Trusted. Most Cited. Most Read.

Title: Structural Implications on the Properties of Self-Assembling Supramolecular Hosts for Fluorescent Guests

Author: Sicheng Tang, Bryan Donaphon, Marcia Levitus, et al

Publication: Langmuir

Publisher: American Chemical Society

Date: Aug 1, 2016

Copyright © 2016, American Chemical Society

LOGIN

If you're a copyright.com user, you can login to RightsLink using your copyright.com credentials. Already a RightsLink user or want to learn more?

Quick Price Estimate

Permission for this particular request is granted for print and electronic formats, and translations, at no charge. Figures and tables may be modified. Appropriate credit should be given. Please print this page for your records and provide a copy to your publisher. Requests for up to 4 figures require only this record. Five or more figures will generate a printout of additional terms and conditions. Appropriate credit should read: "Reprinted with permission from {COMPLETE REFERENCE CITATION}. Copyright {YEAR} American Chemical Society." Insert appropriate information in place of the capitalized words.

I would like to...	reuse in a Thesis/Dissertation
Requestor Type	Author (original work)
Portion	Full article
Format	Print and Electronic
Will you be translating?	No
Select your currency	USD - $
Quick Price	Click Quick Price

QUICK PRICE | CONTINUE

This service provides permission for reuse only. If you do not have a copy of the article you are using, you may copy and paste the content and reuse according to the terms of your agreement. Please be advised that obtaining the content you license is a separate transaction not involving Rightslink.

To request permission for a type of use not listed, please contact the publisher directly.